H2020 - Research and Innovation Action

APPLICATE

Advanced Prediction in Polar regions and beyond: Modelling, observing system design and LInkages associated with a Changing Arctic climaTE

Grant Agreement No: 727862

Deliverable No. 2.5

Final report on model developments and their evaluation in coupled mode

Submission of Deliverable

Work Package	**WP2 Enhanced weather and climate models**		
Deliverable No	2.5		
Deliverable title	Final report on model developments and their evaluation in coupled mode		
Version	**1.0**		
Status	**Final**		
Dissemination level	**PU - Public**		
Lead Beneficiary	UCLouvain		
Contributors	× **1 – AWI**	☐ **2 – BSC**	× **3 – ECMWF**
	☐ **4 – UiB**	× **5 – UNI Research**	☐ **6 – MET Norway**
	× **7 – Met Office**	× **8 – UCLouvain (UCL)**	☐ **9 – UREAD**
	× **10 – SU**	× **11 – CNRS-GAME**	× **12 - CERFACS**
	☐ **13 – AP**	☐ **14 – UiT**	☐ **15 - IORAS**
	☐ **16 - MGO**		
Due Date	**30-11-2020**		
Delivery Date	**11-01-2021**		
Coordinating author	Leandro Ponsoni (leandro.ponsoni@uclouvain.be)		
Contributing authors	Mukesh Gupta (UCLouvain), Jean Sterlin (UCLouvain), François Massonnet (UCLouvain), Thierry Fichefet (UCLouvain), Claudia Hinrichs (AWI), Tido Semmler (AWI), Gabriele Arduini (ECMWF), Jeff Ridley (Met Office), Aleksi Nummelin (UNI Research), Rym Msadek (CERFACS), Laurent Terray (CERFACS), David Salas y Melia (CNRS-GAME), Gunilla Svensson (SU), Ed Blockley (Met Office)		

This project has received funding from the European Union's Horizon 2020 Research & Innovation programme under grant agreement No. 727862.

Contents

Executive summary

In such a remote and harsh environment as the Arctic, the monitoring of essential climate variables is expensive and, therefore, sporadic. In turn, satellites provide observations constrained to the surface. Also, because of technical restrictions, satellites cannot sample, at least not year-round, a set of essential variables, such as the sea ice thickness. To overcome this difficulty, numerical models are key tools for studying and predicting the Arctic weather and climate. Numerical models aim at reproducing the interactions between different climate components such as the land, atmosphere, ocean, and sea ice. Such interactions are complex and described with non-linear functions. This is one reason numerical models are in constant improvement.

The primary goals of Work Package 2 are to promote improvements in numerical models and establish the impact of these improvements on model results, both for the study of the Arctic climate and numerical weather prediction. This deliverable presents a set of model enhancements that are implemented and tested in fully coupled models (AWI-CM1, HadGEM3-GC3.1, EC-Earth3 PRIMAVERA, and ECMWF IFS CY45R1) and forced-mode (NEMO3.6-LIM3 and GELATO).

All model developments aim to improve the representation of physical processes that take place in the sea ice or snow. These consist of a better representation of the turbulent exchanges of heat and momentum between the atmosphere and sea ice (form drag), a description of the melt ponds that appear on the sea ice surface during the melt season (melt ponds), a parameterization which takes into account the effect of the sea ice attached to the shore and ocean floor (landfast ice), a scheme which accounts for the size of the floes that form the sea ice cover (floe size distribution), and an improved representation of the snow both over land and sea ice (multilayer snow scheme).

We assess the benefit of the model developments based on the following five aspects: (i) changes in various components of the Arctic surface energy budget, (ii) changes in the transfer of momentum from the atmosphere to the ocean, (iii) the overall realism of the simulated climate system, (iv) effects on the Arctic Ocean circulation, and (v) changes in the Arctic climate sensitivity.

Common results emerged from the form drag experiments: increased sea ice drift speed in the marginal ice zone, a general decrease in ice thickness, and a marginal decrease of ice concentration at the ice edge in summer. The form drag parameterization improved the large-scale atmospheric and ocean-driven ocean circulation. The melt pond parameterization shows a clear impact on the albedo and sea ice variability and reinforces that a reduced sea ice regime in the Arctic impacts the large-scale, density-driven ocean circulation.

The multilayer snow scheme makes the models more sensitive to the surface thermodynamic forcing than the control run with a single layer of snow and shows a more realistic albedo. In numerical weather prediction, the multilayer scheme leads to an improved prediction of the 2-m temperature diurnal cycle over land. Over sea ice, the new scheme reduces large positive biases of outgoing longwave radiation. Fast ice developments lead to more realistic sea ice conditions supported by evidence from observational data. Parameterization of floe size distribution reveals sea ice growth caused by large ice floes in the marginal ice zone during summer.

1 Introduction

1.1 Background and objectives: APPLICATE, WP2 and D2.5

One of the key aims of APPLICATE is to develop an enhanced predictive capacity for weather and climate in the Arctic and beyond. Within APPLICATE, Work Package 2 (WP2) is devoted to enhancing weather and climate models. One of the major goals of WP2 is to perform model developments to improve the simulated state and dynamics of the atmosphere-sea ice-ocean system in the Arctic, focusing on the processes representation and on the coupling methodology in different global models such as AWI-CM, CNRS-CM, EC-Earth, HadGEM3, and IFS CY45R1.

The main core of Deliverable 2.5 (D2.5) is dedicated to assessing the model enhancements through coordinated experiments performed in Task 2.3.1, which are subsequently evaluated in Task 2.3.2. The experiments from Task 2.3.1 consisted of equilibrium and transient climate runs (piControl and 1pctCO2 CMIP6-like experiments) and ensembles of sensitivity runs with constant forcing. Task 2.3.2 aims at evaluating the benefit of the model developments in terms of the following five aspects:

(i) changes in various components of the Arctic surface energy budget (radiative, turbulent);
(ii) changes in the transfer of momentum from the atmosphere to the ocean;
(iii) the overall realism of the simulated climate system;
(iv) effects on the Arctic Ocean circulation;
(v) changes in the Arctic climate sensitivity.

In summary, the overall goal of this document is to collect and organize the intended contribution to D2.5 from the WP2 partners. In practical terms, D2.5 is mainly based on the results produced in Tasks 2.3.1 and 2.3.2. However, other tasks also contribute to D2.5, such as Task 2.1.2 (Improve description of snow on land and sea ice).

1.2 Deviations from the original proposal

D2.5 (and associated tasks) experienced deviations from its original proposal in terms of postponing the delivery beyond the deadline and also regarding its contents.

Initially scheduled for June 2020, D2.5 is being delivered in January 2021. The main reason for this delay is associated with the challenges and interruptions of the workflow imposed on all WP2 groups by the restrictions resulting from the COVID-19 pandemic. This delay was previously communicated and discussed between our APPLICATE Project Manager and the Project Officer.

Originally, Task 2.3.1 was designed to perform a suite of CMIP6-like experiments. These experiments consisted of a 200-year long control simulation under pre-industrial forcing, a historical run, and a 1pctCO2 simulation. However, previous climate projection analyses and sensitivity tests performed both in WP2 and WP5 revealed that the CMIP6-like experiments were not the best way to evaluate the impact of the individual model developments. We decided that a better use

of resources - both computing and staff - would be to tailor the analysis for each development to better show the impacts. This approach was consulted with and approved by the Project Officer in the context of WP5 (also to be reported in the upcoming Deliverable 5.4). Note that this change of approach does not impact the main overall goal of D2.5: to report and provide an evaluation of a set of model enhancements.

Even though D2.5 is dedicated to present the assessment of the model developments in coupled mode, we take advantage of this report to also present the developments which were so far implemented and tested in forced mode. These are on the way to be integrated into fully coupled models.

1.3 Organization of this report

The remainder of this report is structured as follows. Section 2 presents a brief description of the sea ice model enhancements carried out in WP2. Sections 2.1–2.5 focus on each category of model enhancements. Within each category the methodological aspects and performed experiments are described for the development in each model. In total, this report refers to ten sea ice and snow model enhancements: namely three Form Drag (Secs. 2.1.2, 2.1.1, and 2.1.3), two Melt Ponds (Secs. 2.2.1 and 2.2.2), three Multilayer Snow Schemes (Secs. 2.3.1, 2.3.2, and 2.3.3), one Landfast Ice (Sec. 2.4.1), and one Floe Size Distribution (Sec. 2.5.1) parameterizations.

In addition to the model enhancements, Sec. 2.6 describes the model outputs and approach used for evaluating the impact of increased model resolution on the physical processes driving Arctic surface warming amplification in 1pctCO2-increase simulations.

The results from the experiments with the newly implemented parameterizations in coupled mode are presented in Sec. 3. Results and accompanying discussion are sorted as follows: form drag (Secs. 3.1.2, 3.1.1, and 3.1.3), melt pond (Sec. 3.2.1), multilayer snow scheme for weather forecasts (Sec. 3.3.1), landfast ice (Sec. 3.4.1), and floe size distribution (Sec. 3.5.1). The impact of the increased model resolution on the CMIP6-1pctCO2 experiments is discussed in Sec. 3.6.

Sec. 4 presents additional results from experiments performed in forced mode for the following model developments: form drag (Sec. 4.1.1; in complement to the experiments in coupled mode described in Sec. 3.1.3), melt pond (Sec. 4.2.1), and multilayer snow schemes for climate projections (Secs. 4.3.1 and 4.3.2).

Section 5 presents the main conclusions and outlook of this report. There, the key conclusions are presented in perspective with the five aspects (i–v) defined earlier in Section 1.1. Note that not all the aspects are considered for each development but only the most relevant ones. Lastly, the References and List of acronyms are presented.

2 Model enhancements and experiments

As highlighted above, D2.5 is focused upon ten model enhancements implemented into APPLICATE modelling systems by five different modelling centres: AWI (1-development), CNRM (2-), ECMWF (1-), Met Office (1-), and UCLouvain (5-). Table 1 provides a summary of the experiments conducted to assess each model development in terms of the used numerical model, whether the experiment was performed in coupled (or forced) mode, the time span of the runs, and the number of ensemble members. The table also informs which of the five aspects (i–v, Sec. 1.1) are relevant to each model enhancements. These model enhancements and experiments have been conducted under different climate conditions and forcing to assess their performance and, at places, a diagnostic developed in WP1 (D1.3) is used.

2.1 Form drag

In climate models, turbulent exchanges of heat and momentum between the atmospheric boundary layer and sea ice are parameterized with bulk formulae. The drag coefficients used in these schemes for momentum and heat exchange over sea ice are often just constant values and do not account for the sub-grid heterogeneity of the sea ice - such as the impact of form drag over floe edges, leads, and melt ponds. Meanwhile observations show that drag is not linearly related to sea ice concentration (SIC; e.g., Andreas et al. (2010)).

Several parameterizations have been proposed to improve the representation of sea ice form drag for the calculation of surface exchanges of momentum and heat: Steiner et al. (1999), Lüpkes et al. (2012, 2013), Tsamados et al. (2014, 2015), Elvidge et al. (2016), Renfrew et al. (2019). Here, the Lüpkes or Tsamados parameterizations are implemented into three global climate models (AWI-CM1, EC-Earth PRIMAVERA, and HadGEM3-GC3.1). In the Lüpkes scheme, the drag coefficients for heat and momentum are enhanced to include a parameterization of form drag from ice edges derived from the SIC. The Tsamados parameterization further extends the Lüpkes parameterization of atmosphere-sea ice form drag by using information about the subgrid distribution of ice thickness, melt ponds, and pressure ridges (sails) provided by the sea ice model component. The Tsamados method also provides an analogous parameterization of ice-ocean drag using the subgrid distribution of ridges (keels) information available in the sea ice model. The Tsamados approach is to decompose the neutral drag coefficients into the sum of skin drag and form drag components associated with sea ice ridges, floe edges, and melt ponds edges.

A more detailed description of the parameterization schemes and the sensitivity experiments carried out to test their overall effect are given below.

Table 1: Selected specifications of the model enhancements (first column) and respective experiments performed to assess the enhancements.

Enhancement	Scheme	Experiment(s)	Time span	Ensemble Members	Model (coupled or forced)	Results' Section	Covered aspects (i–v)	Institute
Form Drag	Tsamados et al. (2014)	CMIP6-like piControl	500 years	1	HadGEM3-GC31-LL (coupled)	3.1.1	i, ii, iii, iv, v	Met Office (runs and enhancement)
		CMIP6-like +1%CO2	150 years	4				NORCE and UCLouvain (analyses)
	Luepkes et al. (2012) Luepkes et al. (2013) Luepkes and Gryanik (2015)	Constant 1950-forcing	20 years	10	AWI-CM1 (coupled)	3.1.2	ii	AWI
	Tsamados et al. (2014)	Constant 2000-forcing	10 years	1	EC-Earth-PRIMAVERA (coupled)	3.1.3	ii, iii	UCLouvain
	Tsamados et al. (2014)	Constant 2000-forcing	58 years	1	NEMO/LIM3 (forced)	4.1.1	ii, iii	UCLouvain
Melt Pond	Flocco and Feltham (2007) Flocco et al. (2010, 2012)	Constant 2000-forcing	165 years	1	EC-Earth-PRIMAVERA (coupled)	3.2.1	i, iv	UCLouvain
	Holland et al. (2012)	Atmospheric JRA55 forcing	61 years	1	NEMO/GELATO (forced)	4.2.1	iii	CNRM
Multilayer Snow Scheme	Arduini et al. (2019)	Coupled 10-day forecasts initialised with operational ECMWF analysis	Winter 2014/2015 and 2016/2017	1	IFS CY45R1 (coupled land-ocean-atmosphere)	3.3.1	i, iii	ECMWF
	Lecomte et al. (2013)	Atmospheric DFS5.2 forcing	58 years	1	NEMO/LIM3 (forced)	4.3.1	i	UCLouvain
	Boone (2002) Køltzow (2007) Lebrun (2019)	Atmospheric JRA55 forcing	61 years	1	NEMO/GELATO (forced)	4.3.2	iii	CNRM
Landfast Ice	Lemieux et al. (2015, 2016)	Constant 2000-forcing	10 years	1	EC-Earth-PRIMAVERA (coupled)	3.4.1	iii	UCLouvain
Floe Size Distribution	Luepkes et al. (2012)	Constant 2000-forcing	10 years	1	EC-Earth-PRIMAVERA (coupled)	3.5.1	i	UCLouvain
Ocean Resolution	NA	+1%CO2	140-years	1	CNRM-CM6-1, HadGEM3-GC31, MPI-ESM1-2, and GISS-E2-G	3.6.1	v	CERFACS (analyses)

2.1.1 Implementation of form drag parameterization within HadGEM3-GC3.1

The Met Office's CMIP6 climate model HadGEM3-GC3.1 (Williams et al., 2017) has been modified to use an extended version of the Tsamados et al. (2014) form drag scheme. Although the Tsamados scheme was already available in the CICE5 model that forms the sea ice component of HadGEM3, several modifications to the model code had to be made. The complications arise because surface exchanges over sea ice in HadGEM3 are calculated as part of the JULES surface exchange scheme rather than in the sea ice model component (see Ridley et al. (2018)). Doing the coupling in this way allows the model to perform a consistent calculation of surface exchange/near-surface boundary layer across the globe and reduces the errors in ice-atmosphere flux calculations (West et al., 2016).

To fully implement the Tsamados form drag scheme into HadGEM3 therefore, the coupling interfaces were modified to pass the roughness lengths calculated in CICE through to the JULES surface exchange scheme where the wind stress is calculated (within the boundary-layer routines). The scheme was further extended to include changes to the thermal roughness length, based on the work of Renfrew et al. (2019), that have been shown to improve the scalar transfer of latent and sensible heat and boundary-layer formulation in the (uncoupled) MetUM atmosphere model. These improvements to the scalar transfer were implemented into the MetUM outside of the APPLICATE project but are applied here in coupled mode for the first time.

Several 50-year climate model simulations were performed using the modified HadGEM3 model with the form drag scheme enabled to tune the new scheme. This was done using both the medium- and low-resolution CMIP6 configurations of HadGEM3 described in Roberts et al. (2019): namely HadGEM3-GC3.1-MM (N216-ORCA025 resolution) and HadGEM3-GC3.1-LL (N96-ORCA1 resolution). For each configuration/resolution, between 3 and 5 simulations were performed using different combinations of values for the various parameters within the form drag scheme. The selection of these parameter values was motivated by a review of the relevant literature and by consultation with some of the developers of the original form drag scheme.

Once the tuning was completed a 500-year pre-industrial control simulation was performed using the HadGEM3-GC3.1-LL model along with a 4-member ensemble of +1pctCO2 simulations following the CMIP6 DECK protocols.

2.1.2 Implementation of form drag parameterization within AWI-CM1

The Lüpkes parameterization (Lüpkes and Gryanik, 2015a; Lüpkes et al., 2012, 2013) was implemented into ECHAM, the atmospheric model component of AWI-CM1 (Semmler et al., 2020). In the default version, the effective drag coefficients for heat and momentum exchange over ice are constant everywhere and assumed to be of the same value which is contradictory to measurements. With the new parameterization following Lüpkes and Gryanik (2015b), the skin drag and heat transfer coefficients were amended separately to explicitly include form drag active where SIC is below 1 as can be seen in Fig. 1. The effective drag coefficients and heat transfer coefficients shown are approximately linearly depend on SIC for the neutral stability case over sea ice. In the model

the effective drag coefficients and heat transfer coefficients over ice are then combined with those over water.

To test the long-term impact of the new parameterization in AWI-CM1, control and sensitivity experiments, generated through a small perturbation in the atmosphere, are branched off a long spin-up run. Each experiment is run for 20 years with 10 members each with constant 1950 GHG forcing to evaluate the long-term impact of the new parameterization (see Section 3.1.2).

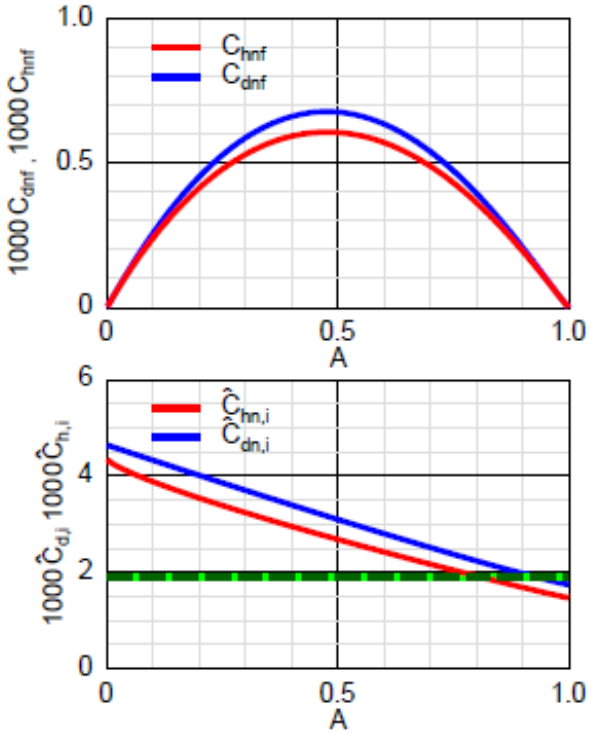

Figure 1: Top: Form drag coefficient (C_{dnf}, blue) and edge-related heat transfer coefficient (C_{hnf}, red) as function of SIC (A). Bottom: Effective drag coefficients ($\hat{C}_{dn,i}$) and heat transfer coefficients ($\hat{C}_{hn,i}$) over sea ice (green: old version of ECHAM6, red: new heat transfer coefficient, blue: new drag coefficient). Figure provided by C. Lüpkes–AWI.

2.1.3 Implementation of form drag parameterization within NEMO3.6-LIM3 and EC-Earth3

The form drag parameterization implementation within NEMO3.6-LIM3 (forced) and EC-Earth3 PRIMAVERA (coupled) follows the work of Tsamados et al. (2014). We introduced new tracers of level ice area and volume in the sea ice model LIM3 to calculate the ice ridge contribution. The tracers keep track of the SIC and volume that do not deform because of mechanical processes, such as ridging and rafting. A difference between the SIC (volume) and the level-ice concentration

(volume) gives the deformed ice concentration (volume). The scheme uses the deformed ice quantities to estimate the height and depth of the top and bottom ice ridges, and the distance between them. We parameterize the length of the floes and the average distance between them as functions of the ice concentration (Lüpkes and Birnbaum, 2005; Lüpkes et al., 2012). Last, form-drag calculations use the melt pond schemes to determine pond sizes as melt ponds edges contribute to the form drag. The topographic melt pond scheme (Flocco and Feltham, 2007; Flocco et al., 2010, 2012) estimates the average melt pond size (see Sec. 2.2.1).

To study the effect of the variable drag coefficients of Tsamados et al. (2014) on the Arctic sea ice, we have performed simulations both in coupled (see Sec. 3.1.3) and forced modes (see Sec. 4.1.1). In forced mode we run NEMO3.6-LIM3 (forced mode) using Drakkar Forcing Set version 5.2 (DFS5.2; Dussin et al. (2016)), from years 1958 to 2016. The control simulation uses the default constant (neutral) drag coefficients of 5×10^{-3} (ocean-ice interface) and 1.4×10^{-3} (ice-atmosphere interface). The form drag simulation uses the drag formulation of Tsamados et al. (2014). In forced mode, we decreased the time steps of the ocean and ice models by a factor of four to ensure its stability in coastal regions in both simulations.

In the current configuration at UCLouvain, NEMO3.6-LIM3 uses a 1° curvilinear tripolar grid of the ORCA family as the horizontal grid. The vertical grid has 75 vertical levels in partial step z-coordinate. We calculate transfer coefficients over the ocean according to Large and Yeager (2004, 2008) using the Monin-Obukhov Similarity Theory. When conducted with a prescribed atmospheric state, NEMO3.6-LIM3 follows the recommendations of the Coordinated Ocean-ice Reference Experiments (CORE) (Griffies et al., 2009). The forcing method uses bulk formulae to derive the wind stress, sensible and latent turbulent heat fluxes from surface variables in atmospheric reanalyses. The method used in coupled mode is the same, except that coupled-mode simulations use a Global Circulation Model (EC-Earth PRIMAVERA).

2.2 Melt ponds

Melt ponds appear during the melt season in the Arctic when the surface meltwater accumulates in the depressions of the ice field. Many global coupled models predict high mean albedo over sea ice because melt ponds do not exist in these models. Melt ponds reduce the mean albedo over sea ice during summer as observed by the satellites in different regions of the Arctic Ocean (Laine, 2004). Therefore, it is important to parameterize melt ponds in the models.

The meltwater originates from the melting of the ice and snow surface layers, and liquid precipitation collected on the ice surface. The albedo of the melt ponds (∼0.24) is considerably lower than those of snow (∼0.80) and ice (∼0.72) (Grenfell and Perovich, 2004; Shine and Henderson-Sellers, 1985). Therefore, melt ponds are an important aspect of the ice-albedo feedback, whereby a reduction in the ice cover results in lower surface albedo, greater absorption of solar radiation, and further ice melt. Additionally, melt ponds act as temporary reservoirs of freshwater. The accumulated freshwater either flushes to the ocean through several processes, re-integrates to the ice cover when melt ponds refreeze or evaporates back to the atmosphere.

2.2.1 Implementation of melt pond parameterization within EC-Earth3

We implemented the topographic scheme of Flocco and Feltham (2007) and Flocco et al. (2010) in the EC-Earth3 PRIMAVERA (r4796, revision 5888) setup (Haarsma et al., 2020; Roberts et al., 2020). This scheme defines an implicit relationship between the melt pond area and depth by using the prognostic sea ice thickness (SIT) distribution to estimate the morphology of the ice surface. The topographic scheme fills the surface categories in ascending order, with the meltwater for ponds to develop, considering the volume of saturated snow.

The version of the topographic scheme at UCLouvain follows the implementation by Lecomte et al. (2015), except for the refreezing mechanism which has its basis on the formulation proposed by Holland et al. (2012). There is an exponential decrease in the volume of meltwater in the ponds with time when the surface air temperature is cold enough to refreeze the melt ponds. The exponential rate depends on the difference between the surface temperature and a refreezing temperature parameter κ in °C. The volume of refrozen water in the melt ponds is redirected to the ocean in the form of a freshwater flux to ensure both mass and heat conservation.

The albedo scheme in the LIM3 sea-ice model uses the melt pond depth to estimate the surface albedo of the ponds. Then, LIM3 assigns weights to the surface albedo as it changes with the surface area for various surfaces (ice, melt pond, ocean, snow). We estimate the flux of meltwater entering the melt ponds as a fraction r of the fluxes of melting snow and ice at the surface. The fraction varies with the ice concentration per category as $r(A_i) = 0.15 + 0.55A_i$. The expression is closely related to the formulation of Holland et al. (2012). However, using the ice concentration per category (A_i) limits erroneous input of meltwater in melt ponds when the ice concentration in categories is too low to sustain meltwater. To conserve meltwater across the model, we changed the calculation method of the input meltwater for melt ponds from a flux-based estimation to a derivation from the changes at the surface in snow and ice thickness. This new approach limits erroneous flux values for the melt pond scheme when activated.

The surface energy budget during summer in the Arctic is very sensitive to the melt pond formation. The energy budget controls the amount of sea ice, i.e., ice volume, concentration, and extent at the end of the season and throughout the year. To study the impact of the melt pond implementation in EC-Earth3 PRIMAVERA, we conduct a sensitivity experiment under constant atmospheric forcing (i.e., 2000). This experiment aim to estimate the impact of introducing melt pond parameterization on the evolution of sea ice on seasonal and decadal time scales.

2.2.2 Implementation of melt pond parameterization within GELATO

A new prognostic melt pond scheme has been developed in the GELATO sea ice model. Melt ponds are defined by two prognostic variables: the water volume and the volume of the ice lid that forms as melt pond refreezing takes place. Both quantities are advected along with the other ice state variables. The fraction of sea ice covered with melt ponds, and their depth is computed from the melt pond volume, assuming a statistical relationship between the fraction and depth of melt ponds (Holland et al., 2012).

In the model, melt ponds are considered as "levitating" reservoirs of water that fill up with the part of the snowpack and ice surface meltwater that is not drained to the ocean. At the end of the summer, as the melt ponds are refreezing, the formed ice contributes to decreasing the volume of melt ponds, until they vanish. The formation of ice lids covering melt ponds is represented following Hunke et al. (2013). For simplicity, in order to ensure water conservation, the amount of water corresponding to the rate of melt pond ice formation is sent to the ocean. However, a limitation of this simplification is a positive bias in freshwater input to the ocean in early summer. The melt pond albedo is here diagnosed from melt pond depth.

To assess the impact of the melt pond parameterization within GELATO, 61-year (1958-2018) simulations are performed with and without the activation of the parameterization. These are atmosphere-forced simulations that follows the CMIP6/OMIP2protocol (JRA-55-based; Tsujino et al. (2018)). The results shown in Sec. 4.2.1 are based on a 30-year period from 1981 to 2010.

2.3 Multilayer snow scheme

The snow physical properties play an important role in heat conduction through the snow-ice system. Snow acts as a thermal insulator, which affects sea ice growth and melt. The relatively low thermal conductivity of snow, compared to the heat conduction in sea ice (approximately 10 times larger), reduces the ice growth at the ice base because of less heat loss to the atmosphere caused by reduced conductive heat flux from the sea ice to the snow-air interface. The process of heat transfer through the snow can be via conduction through interconnected ice crystals, or interstitial air trapped in the snow layer, or through latent heat. The effective thermal conductivity governs the growth and melt of sea ice. Therefore, it is important to consider the number of snow layers used in a model as it influences the effective heat conduction through the ice column. Many large-scale land and sea ice models use a constant thermal conductivity of snow, thus ignoring snow physics.

2.3.1 Implementation of multilayer snow scheme within ECMWF Integrated Forecasting System

A new multilayer snow scheme was developed and tested within the ECMWF Integrated Forecasting System (IFS) to improve the model realism in short- to medium-range weather forecasts. The technical description of the new multilayer snow scheme is reported in APPLICATE Deliverable 2.3 (D2.3) and Arduini et al. (2019). In D2.3, the evaluation was performed in land surface-only simulations, as well as an initial assessment in coupled forecast mode for selected case-studies both over land and sea ice.

In this deliverable, we report on the assessment of the new snow scheme in coupled forecast mode at the global scale, considering several months (e.g., a winter) providing more robust statistics. At first, the multilayer snow scheme is activated only over land and its impact on near-surface weather forecasts is evaluated. Then, it is activated both over land and sea ice to evaluate the impact on the sea ice surface temperature in the Arctic region.

2.3.2 Implementation of multilayer snow scheme within NEMO3.6-LIM3

A new scheme for snow on sea ice following Lecomte et al. (2013) was implemented in the NEMO3.6-LIM3. This new snow component includes the following physical components:

- A multilayer snowpack representation on sea ice.
- Wind-dependent snow density.
- Density-dependent snow thermal conductivity.
- Sea ice albedo based on an effective "patchy" snow cover.
- An improved shortwave radiation transfer in snow, similar to the treatment of the radiation transfer in sea ice and taking the effective snow cover into account as well.

Multilayer snow scheme specifications in forced mode are available in Table 2.

Table 2: Specifications of the control run (CTRL) and multilayer snow experiments.

Development	**CTRL**	**Multilayer snow**
Snow layers	1	3
Parameterization for snow density (nn_sno_dens)	0	2 (wind dependent correction)
Snow thermal conductivity formulation (nn_sno_thcon)	0	3 (wind dependent)
Parameterization for radiative transfer in snow (nn_sno_rad)	0 (no radiative transfer, snow absorbs all shortwave radiation at the surface)	1 (radiative transfer as in sea ice, with specific extinction coefficients)
Computation of surface albedo based on an effective snow coverage on sea ice (nn_sno_alb)	0 (parameterization for patchy snow albedo: no treatment of patchy snow (standard))	1 (snow depth dependent)

The multilayer snowpack representation on sea ice investigated by Lecomte et al. (2013) was the first in a global ocean-sea ice coupled model. However, the results of this exploratory study remained rather qualitative in terms of the sensitivity of the sea ice mean state and seasonal to multi-decadal variability to the snow representation. Here, we implement the snow representation using more robust numerical methods allowing an improved assessment of a new set of physical sensitivity tests, also using evaluation metrics that were not available at the time of the preliminary work by

Lecomte et al. (2013). In this scheme, the state variables of all snow layers undergo advection instead of the total snow mass horizontal transport with sea ice. The wind-induced transformation of snow properties takes place through the snowfall density because of a vertical remapping preserving resolution in the top snow layers in the thermodynamics. This implementation method allows conducting sensitivity experiments on the number of snow layers present (on sea ice) in a climate model. Sea ice albedo relies on the existing patchy snow parameterization of the CICE/CESM model and Hunke et al. (2013) but the model tests it combining with multilayer snowpack and improved shortwave radiation. The improved shortwave radiation extends the current treatment of the shortwave radiation transfer in sea ice in NEMO3.6-LIM3 to snow (use of a surface scattering layer and snow-based extinction coefficients by Pogson et al. (2011)).

The effect of introducing the multilayer snow thermodynamic scheme in the sea ice model LIM3 is assessed in 58-year forced mode NEMO3.6-LIM3 experiments. We discuss the state and variability of the Arctic sea ice volume and surface snow depth with and without the multilayer snow parameterization. The simulations rely on the NEMO3.6-LIM3 setup with a prescribed atmospheric surface state, as described in Section 2.1.3.

2.3.3 Implementation of multilayer snow scheme within GELATO

In the initial version of GELATO 6, used within CNRM-CM6-1 for CMIP6 (Voldoire et al., 2019), the ice and snow parts of every ice thickness category are treated separately, as two media that interact with each other. The only exception to this rule is for solving the vertical heat diffusion, where the ice and snow system is considered as a single slab with variable density, salinity, and heat diffusion coefficients over the vertical, following Hunke and Lipscomb (2010). In this original version, five ice thickness categories are considered. Each of them have nine levels in the ice part of the slab. The snowpack is represented by a single layer.

The sensitivity experiments to the inclusion of various processes in GELATO are based on a model version that differs from the version used for CMIP6. The reason for developing and using an upgraded model as a reference version is that, as pointed out in Voldoire et al. (2019), the modelled snowpack thickness on sea ice within CNRM-CM6.1 is overestimated year round. During the winter, the too thick snowpack causes an overestimate of the insulating effect of snow, reducing bottom sea ice freezing. More over, due to the persistence of a relatively thick snowpack in summer, the surface albedo is overestimated, leading to an underestimate of both absorbed sunlight and surface melting. In order to reduce these biases, several developments were introduced in GELATO:

- the vertical heat diffusion equation in the ice-snow slab is updated to be solved in two steps. First, the heat diffusion is applied to the snowpack (if any), using temperature at the snow-ice as a bottom boundary condition. Then, the vertical heat diffusion equation is solved in the ice, using the conductive heat flux at the bottom of the snowpack as a top boundary condition, and seawater freezing point as a bottom boundary condition. Since the conductivity of sea ice is a function of temperature, and since the snow-ice temperature depends on both temperature in the upper sea ice layer and in the bottom snow layer, this two-step process is repeated

until convergence is reached. The convergence criterion is that the mean temperature change in the whole slab is less than 0.02 °C between two iterations.

- a snow compaction scheme is incorporated based on the scheme used in the ISBA-ES snow model (Boone, 2002).
- a revised light transmission in the ice and snow is added. The surface transmission parameters, the thickness of the surface scattering layers, and the attenuation coefficient in ice and snow were revised, following Lebrun (2019).
- a revised snow surface albedo scheme is implemented. In the reference version, a simple parameterization of the albedo and fraction of melt ponds was introduced in GELATO, following Køltzow (2007), in case the more complex prognostic melt ponds scheme described in Sec. 2.2.2 is not activated.

Once all these developments were implemented in GELATO, the snowpack model was modified to allow for the use of several layers. Each layer of snow has a specific density and temperature. Like the other state variables describing the sea ice slab, these quantities are advected by the incremental remapping scheme described by Hunke and Lipscomb (2010).

2.4 Landfast ice

Fast ice, or landfast ice, is the part of sea ice attached to the shore, to the ocean floor in shallow sea regions, to ice shelves and marine-terminating glaciers, or restricted by grounded icebergs. The place of occurrence of landfast ice influences interactions between the ocean and ice, the freshwater budgets, and the stability of the halocline layer in the Arctic Basin (Itkin et al., 2015). In the Arctic Ocean, landfast ice sustains through two primary mechanisms. First, landfast ice develops over deep-sea regions by its tensile strength. The tensile strength of sea ice represents the maximum pulling forces that the sea ice can sustain before it breaks. Second, landfast ice occurs in shallow seas, where sea ice ridges can reach the seafloor. These ice ridges serve as anchoring points for landfast ice.

2.4.1 Implementation of landfast ice parameterization within EC-Earth3

To simulate the landfast ice in the Arctic, we changed the ice rheology to better resolve the tensile strength of sea ice and implemented the ice-basal parameterization by Lemieux et al. (2015) in NEMO3.6-LIM3. We tested and tuned the developments with a prescribed atmospheric state (forced mode) as a first step and implemented it in EC-Earth3 PRIMAVERA.

LIM3 uses the Elastic-Viscous-Plastic (EVP) formulation with an elliptical yield curve to resolve the ice rheology similar to other sea ice models in Global Circulation Models. This ice rheology has some but limited tensile strength properties. The ellipse ratio of the yield curve already represents some uni-axial tensile strength. However, the ice rheology does not represent isotropic tensile strength, and cannot account for landfast ice over deep-sea regions. We changed the elliptical yield

curve of the ice rheology in LIM3 to account for both the isotropic and uniaxial tensile strength properties of sea ice. The changes in LIM3 comprise a new parameter k_t to set the amount of isotropic tensile strength in sea ice, a modification in the eccentricity of the elliptical yield curve, and an increased number of sub-iterations for the EVP algorithm.

Following the recommendations by Environment and Climate Change Canada (ECCC), we set the isotropic tensile strength parameter k_t to 0.05 in the simulations, that is 1/20th of the compressive ice strength that agrees with Hibler and Schulson (2000). We changed the eccentricity of the ellipse from 2.0 to 1.4. The lower eccentricity value allows greater uniaxial tensile strength. Last, we increased the number of sub-iterations of the EVP algorithm to resolve the ice rheology. The number of sub-iterations is crucial for the EVP algorithm to converge to a solution, and to simulate landfast ice because of tensile strength properties. An increase of the sub-iterations from 120 to 720 provides a stable solution but doubles the HPC costs compared to the standard rheology for EC-Earth3 PRIMAVERA run on 144 CPUs.

In the set-up of EC-Earth3 PRIMAVERA, the minimum ocean depth is set to 20 m to ensure the stability of the ocean model. However, grounded ice ridges occur only in shallow seas with depths shallower than about 30 m. To go around this limitation, we used an external bathymetry file for applying the grounded scheme, while the minimum EC-Earth ocean depth remained unchanged. The external bathymetry file is provided by ETOPO1 - 1 Arc-Minute Global Relief Model (Amante and Eakins, 2009). We interpolated ETOPO1 data onto the EC-Earth ORCA 1° grid and masked data points from depths in which the grounding scheme is not applicable. Hence, the external bathymetry allows the parameterization to solve grounded ice ridges, but preserves the ocean model stability.

The critical thickness parameter k_1 shows if sea ice has grounded. Grounding occurs if the SIT multiplied by k_1 is greater than the ocean depth. k_1 allows accounting for the sub-grid scale variability of the bathymetry. The value of k_1 depends on the horizontal grid resolution and the bathymetric features of the considered regions. The parameter is equal to 8 given by Lemieux et al. (2015), whereas previous developments on grounded ice in LIM3 used estimates of 6.7 or 10 (Thonner, 2016). Considering the different values for k_1 and the new external bathymetry for grounded ice, we developed an approach to estimate the parameter based on the minimization of a cost function.

We performed fast ice sensitivity experiments with isotropic tensile strength ($k_t = 0.05$) and basal stress parameterization, each 10-year run, using EC-Earth3 PRIMAVERA for constant greenhouse forcing of 2000 to assess the impact of fast ice parameterization (Lemieux et al., 2015; Lemieux et al., 2016) on the sea ice volume and ice concentration. We use a set of observations of landfast ice based on the U.S. National Ice Center (NIC) weekly/bi-weekly ice charts, spanning between 2006 to 2017 (provided by ECCC).

Also, we performed an ocean-ice simulation with the tensile strength and ice rheology modifications activated and without the ice-basal parameterization. Using the spun-up model for the years covering the period of the observational product, we built a cost function with k_1 as the

unknown variable (see Figure 2). The cost function returns the root mean square of the differences between the observed landfast ice area of the ECCC dataset and the landfast ice area that the ice-grounded scheme produces with the prognostic variables of the model, and as it changes with k_1. To perform the minimization of the cost function, we used data where the water depth is less than 30 m, excluding fast ice governed by the tensile-strength-only mechanism, and when collocated observational data were available. The minimum of the cost function is found when k_1 is equal to 7.8, in close agreement with Lemieux et al. (2015).

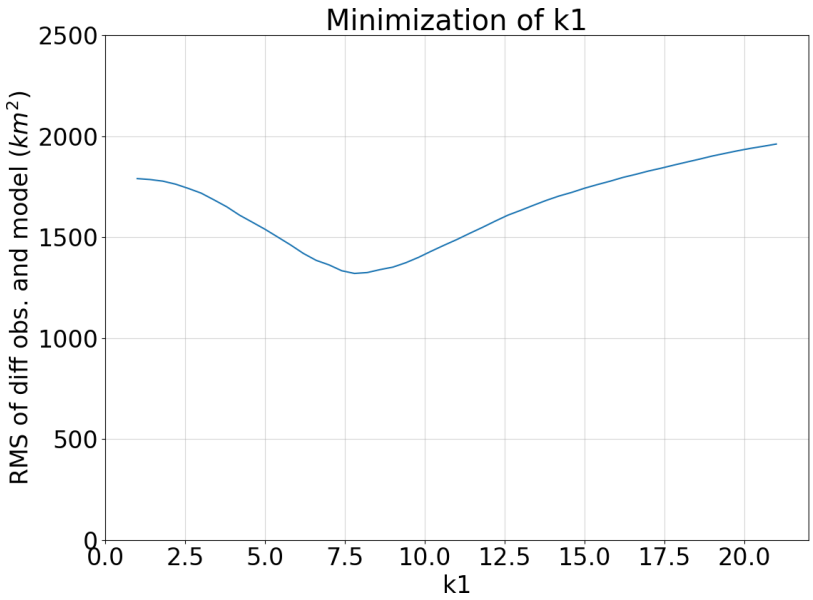

Figure 2: Root mean square (RMS) of the differences between observed landfast ice area based on the U.S. National Ice Center (NIC) weekly/bi-weekly ice charts and estimated landfast ice area by the ice-grounded scheme as a function of the critical ice thickness parameter k_1, using prognostic variables of a simulation with tensile strength and modified ice rheology only. The RMS of the differences is calculated in regions where depth is less than 30 m and in the presence of collocated observations, between 2006 and 2017. The minimum in RMS difference is obtained when k_1 is equal to 7.8.

2.5 Floe size distribution

Although contemporary sea ice models use a fixed floe size, in reality sea ice cover comprises a mosaic of floes with various shapes and dimensions, ranging from a few metres to hundreds of kilometres. The aim of the Floe Size Distribution (FSD) parameterization is to represent the size of the floes within sea ice models and, among other benefits, to provide a proper representation of the lateral ice melt. Overall, the lateral melt is expected to be less important than basal melt, as the bottom of the floes usually have a larger area than the lateral surface. Nevertheless, Horvat et al. (2016) showed that basal melting is intrinsically linked to lateral melting. Density fronts can develop in the sea along the edge of the floes because of atmospheric heat fluxes and local melting.

This, in turn, could trigger baroclinic instabilities and eddy formation accompanied by increased heat transport under the floes (Horvat et al., 2016).

2.5.1 Implementation of floe size distribution parameterization within EC-Earth3

Here, we modified the sea ice thermodynamics in LIM3 within EC-Earth3 PRIMAVERA to study the effect of the FSD on the Arctic sea ice, including the representation of the lateral melting. To do so, the prescribed FSD estimates the mean size of the floes following Lüpkes et al. (2012) as shown in Eq. 1:

$$D = D_{min} \left(\frac{A^*}{A^* - A} \right)^{\beta}. \tag{1}$$

The equation above requires two constant parameters related to the minimum and maximum floe caliper diameters (D_{min}= 8 m and D_{max}= 300 m) and also an exponent β which shapes the relation between SIC (A) and D. A caliper diameter is the distance between the lines when each touches one side of the floe without penetrating the interior (Rothrock and Thorndike, 1984). The parameter A^* avoids a singularity when the SIC tends to 1 (Eq. 2), as follows:

$$A^* = \frac{1}{1 - \left(\frac{D_{min}}{D_{max}} \right)^{\frac{1}{\beta}}}. \tag{2}$$

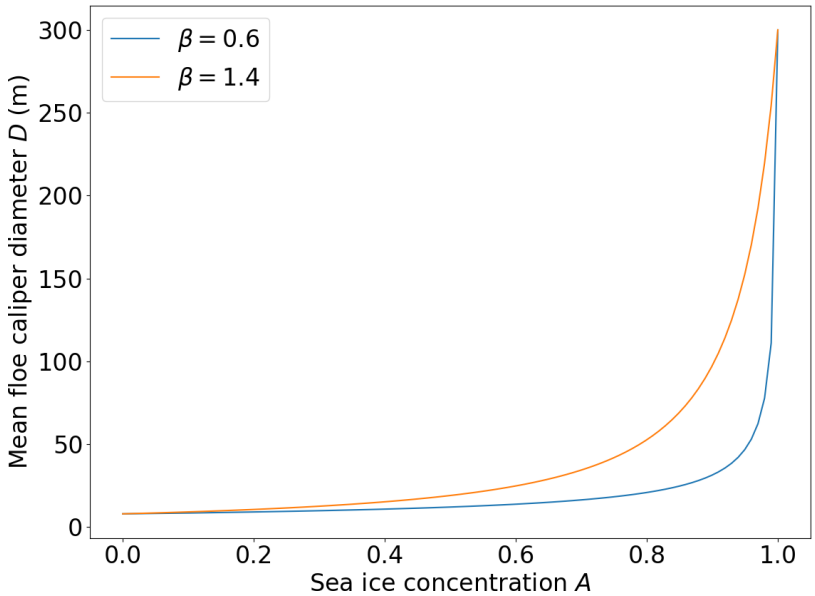

Figure 3: Mean floe caliper diameters estimated from Equation 1 in function of the ice concentration for two different β values.

Figure 3 shows how the mean size of the floes depend on the SIC as prescribed by Eq. 1 for two different values of β (0.6 and 1.4). In practical terms, β depends on the region and the season. For instance, $\beta < 1$ is more representative of the Western part of Fram Strait, whereas $\beta > 1$ is characteristic of the Eastern part of Fram Strait. However, with a prescribed FSD only one value can be used, so we have performed two simulations to test the effects of β on the Arctic sea ice using β=0.6 (FSD1) and β=1.4 (FSD2).

2.6 Increased model resolution

Apart from the model developments discussed in Secs. 2.1–2.5, we also investigated the impact of increased resolution on the physical processes driving Arctic surface warming amplification in 1pctCO2-increase simulations. We consider four models (CNRM-CM6-1, HadGEM3-GC3.1, MPI-ESM1-2, and GISS-E2-G) with two resolutions. The first three models have a low- and high-horizontal resolution version. The last one (GISS model) has a low- and high- vertical resolution. Note that only the first two models are part of APPLICATE, but we included more models to check the robustness of the results.

It is well-known that both observations and historical climate simulations reveal a pronounced seasonality of Arctic surface warming amplification with maximum warming amplification in autumn and winter and minimum in summer. Based on multi-model 1pctCO2-increase climate simulations and following the methodology used in Lu and Cai (2009), we study the relative importance of various feedbacks causing the strong seasonality of Arctic warming amplification. The analysis is performed by calculating partial temperature changes due to each of these processes using a simple linearization of the surface energy budget equation. Contributions to changes in surface temperature are coming from six processes that amplify the change due to the CO_2 concentration increase (see Lu and Cai (2009) for the derivation and details).

3 Coupled mode: results and discussion

3.1 Form drag

3.1.1 Impact of form drag on the sea ice, ocean, and atmosphere within HadGEM3-GC3.1

Impact on the sea ice

The imbalance in the heat fluxes between ocean-sea ice and atmosphere interfaces causes basal accretion of fresh ice in the Arctic. It is crucial to represent heat flow through ocean-sea ice-atmosphere in models. The conduction of heat through sea ice depends on several geophysical parameters–snow and SIT values, the air-ocean temperature contrast, and snow/ice conductivity. It is difficult to test these parameters in models, as there is little observational data. The heat conduction index (HCI, introduced in D1.3 of APPLICATE WP1) metric overcomes this issue by studying how the controlling parameters interact with one another rather than how they perform alone.

The HCI is a new metric that defines how the temperature of the snow-ice interface (T_i represents the temperature of the snow/sea-ice system thermodynamics) depends on the snow or sea ice surface temperature (T_s represents the temperature of the forcing). So, we interpret the HCI as the sensitivity of sea ice thermodynamics (represented by T_i) to the atmospheric thermal forcing (represented by T_s). The value of HCI lies between 0 and 1. A higher value of HCI (HCI > 0.5) shows that the internal temperature of the snow-ice system is more responsive to the atmospheric forcing (implying that heat conduction through ice is more efficient), whereas a lower value of HCI (HCI $<$ 0.5) shows a poor sensitivity to the atmospheric forcing (implying that heat conduction through ice is less efficient). The above definition of HCI reformulates in terms of the state variables (i.e., snow and sea ice thickness) that are available from routine observations. There are a few assumptions for this formulation: (1) the ice-snow system has zero heat capacity, (2) the temperature profile is not nonlinear through the snow-ice system, (3) the basal ice temperature is constant, and (4) the snow and ice conductivity, K_s and K_i, respectively, are constant. The reformulated HCI under the above assumptions is (Eq. 3):

$$HCI = \frac{K_s \times h_i}{(K_s \times h_i + K_i \times h_s)}, \tag{3}$$

where h_s and h_i are the thickness of snow and ice layers, respectively.

The assumptions above prevent the exact measurement of how internal temperature depends on surface temperature. However, the diagnostic (Eq. 3) is useful for evaluating models with the following advantages:

- Snow and ice thickness are standard geophysical parameters and have routine measurements during field campaigns. The heat conductivity is less constrained and, if no estimate is

available from the field, the same reference values can be useful in models and observations.

- The HCI tests a process (heat conduction) rather than a single geophysical parameter (e.g., SIT or snow depth). This means that a model with SIT twice as large as in observations could still simulate the right HCI value, provided the snow depth is also twice as large as in observations (Eq. 3).
- The HCI formulation is simple and applies without running dedicated experiments: it needs no new output variables. In particular, the HCI can apply to existing models as long as they have archived snow and ice thickness data.
- A robust feature of the HCI is its high stability over time, despite strong trends in Arctic snow and ice thickness. It is clear from the HCI definition (Eq. 3) that if snow and ice thickness are each multiplied by the same constant factor; the HCI remains unchanged. The physics behind the process of heat conduction itself does not change in a warmer climate when both the snow and ice cover melt.

The snow and ice conductivity that appear in the HCI definition are by default: 0.31 and 2.04 W m^{-1} K^{-1}, respectively, following Maykut and Untersteiner (1971) and Lecomte et al. (2015). It is still possible to prescribe other values for these parameters if model specific values are known.

To apply the HCI diagnostic on model outputs, we took the last 100-year mean of the 500-year simulation using HadGEM3 for piControl scenario with and without form drag parameterization (Tsamados et al., 2014). Figure 4 shows September and March difference maps (form drag run minus control run (CTRL)) for SIC and SIT. A decline in SIT, because of the form drag parameterization, occurs in March (winter) in most of the Arctic Ocean except in a small region of Chukchi Sea (Fig. 4d). The impact of form drag parameterization on winter SIC is little in the entire Arctic Ocean (Fig. 4c). Similar results are noted in September (Fig. 4a,b), with exception to the fact that the form drag parameterization leads to a reduction of the SIC near the marginal ice zone (MIZ, Fig. 4a).

The change in HCI shows the impact of form drag parameterization on SIC and SIT. We computed HCI before (CTRL) and after activating the form drag parameterization in HadGEM3. Fig. 5 shows the HCI difference maps for all months. A prominent positive difference (form drag minus CTRL) in the Baffin Bay, Kara Sea, and the Laptev Sea during winter months implies melting and depletion of sea ice because of increased heat conduction in these regions of the Arctic Ocean after parameterizing form drag in the model. A typical value of HCI lies between 0 (low conduction) and 1 (high conduction). The negative difference during winter months in the Beaufort Sea implies accretion of sea ice, most likely because of prevalent ice dynamics in the southwestern Beaufort and Chukchi Seas (Hutchings and Rigor, 2012). During late summer, when SIT and ice concentration are less, the ice depletes in the Fram Strait region because of the higher value of HCI after implementation of the form drag scheme as compared to the CTRL.

As discussed, the HCI diagnostic assessed the sea ice depletion after implementing form drag as shown in Fig. 4. The HCI allows us to get insights on the conduction of heat through the ice system

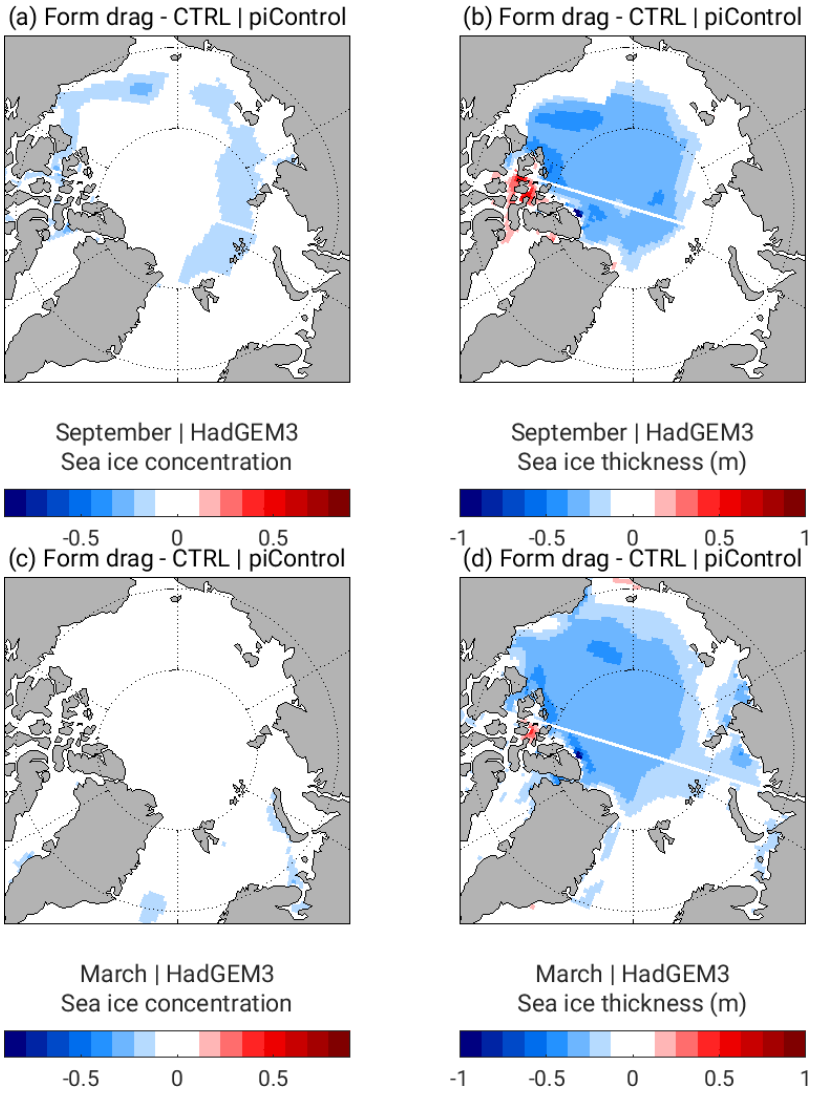

Figure 4: The difference of form drag run and CTRL under piControl scenario for SIC (a,c) and SIT (b,d) for last 100-year mean of 500-year simulation using HadGEM3 for Arctic sea ice in September (a, b) and March (c, d).

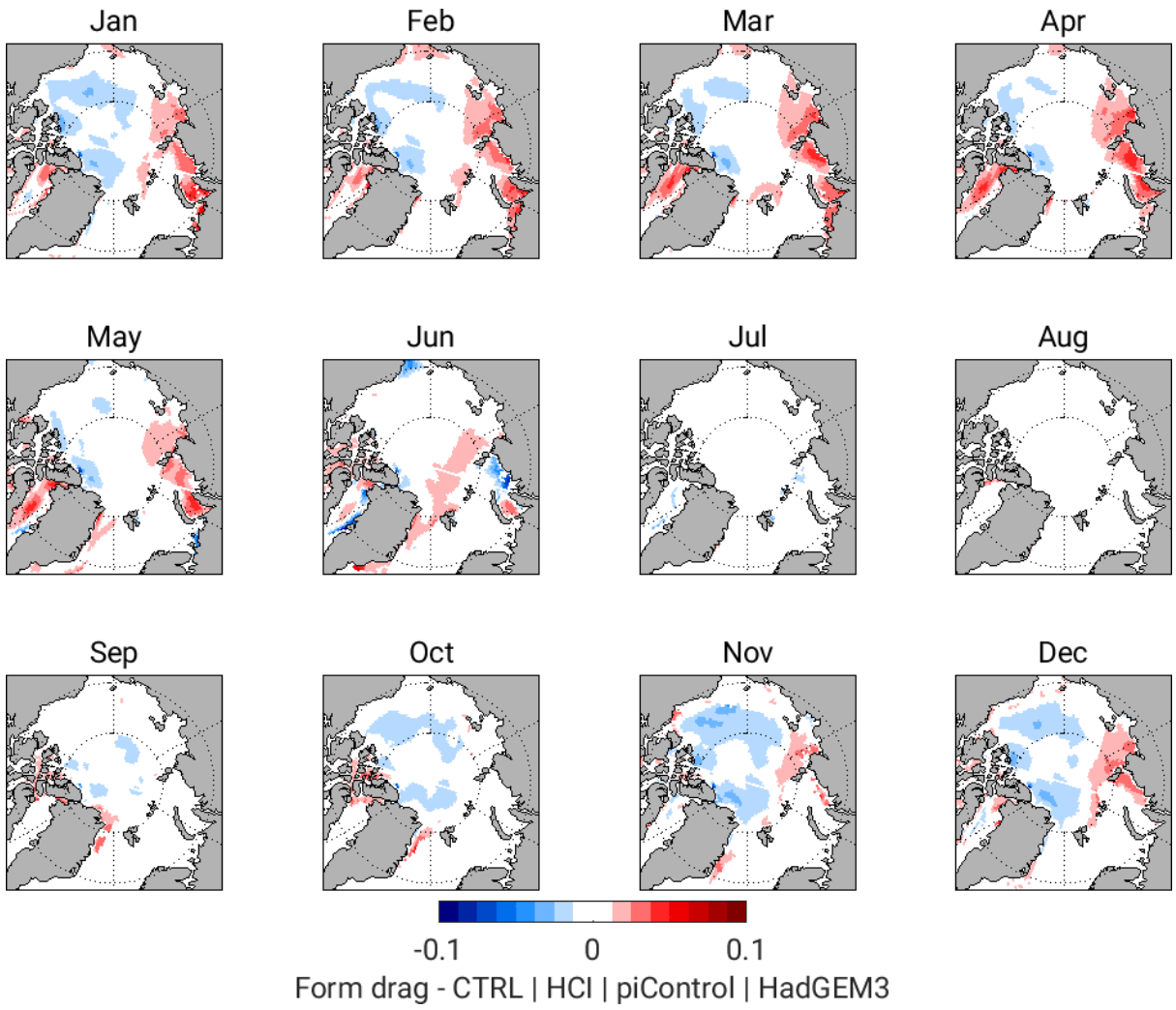

Figure 5: The difference of form drag run and CTRL under piControl scenario for heat conduction index (HCI) for the last 100-year mean of 500-year simulation using HadGEM3 for Arctic sea ice.

(Fig. 5). SIT is less (but higher HCI) in the Baffin Bay region after form drag parameterization. We can explain this inconsistency in part by changes in snow depth. However, the HCI provides additional information and serves as an assessment tool for the model outputs. The HCI computed for the form drag simulation can be compared with the field measurements of snow depths and ice thickness.

Impact on the ocean and atmosphere

Although the form drag affects directly only the heat and momentum exchange through the ice, it is expected to have an impact on the ocean circulation by changing momentum and buoyancy forcing below the sea ice, as well as by impacting the large scale atmospheric circulation. To identify these changes, we have examined the Arctic ocean state in a low CO_2 (100 years of pre-industrial control climate; relatively large, perennial sea ice cover) as well as a high CO_2 climate (last 30 years of the annual 1pctCO2 increase simulation; relatively small, seasonal ice cover).

The results in the low CO_2 control climate show that the impact on the volume budget is small (not shown), but that the modified form drag shifts the inflow and outflow towards warmer temperatures at the Arctic gateways (Fig. 6), and consequently, the Atlantic Water temperatures at depths of 200 m and deeper are 0.4–1 °C warmer in the modified form drag cases (Figs. 7 and 8). This change is driven by large scale changes in the atmospheric circulation: (1) Subpolar gyre adjust to changing wind stress curl zero-line (stronger tilt towards the North-East, i.e., Nordic Seas) leads to warmer inflow to the Nordic Seas (Fig. 7, a clear temperature shift seen as a positive-negative temperature anomaly pair); (2) reduction in the wind speed (not shown) drives a large reduction (up to 50 W m^{-2}, or 40% reduction) in the annual mean turbulent heat flux close to the ice edge (Fig. 12), leading to reduced cooling of the Atlantic Water entering the Arctic at the Fram Strait and Barents Sea Opening (as seen in Figs. 6–8).

The salinity signal is generally small at depth, but the salinity in the surface layer suggests an increase in the Beaufort Gyre freshwater storage, and a reduction in the freshwater storage in the Eurasian Basin. Such a change indicates a shift towards more positive Arctic Oscillation and a consequent change in the freshwater pathways driving larger part of the Eurasian river runoff towards the Beaufort Gyre instead of Fram Strait (Morison et al., 2012). These results are supported by wind stress curl anomalies (Figs. 10 and 11) which show a positive (cyclonic) anomaly over the Eurasian Basin and a negative (anticyclonic) anomaly over the Canada Basin. These anomalies are most pronounced during the winter period (Fig. 11).

Overall, the form drag simulations have reduced ocean temperature and salinity biases in the Arctic in the low CO_2 case, but with an adverse effect of increasing the warm bias in the subpolar gyre. However, the adverse effects could be minimized by additional tuning.

The impact of the form drag is smaller in the high CO_2 climate as the sea ice is lost for much of the year. The atmospheric circulation response, although small, is the opposite to the pre-industrial climate with a northward shift of the zero-wind stress curl line when the form drag is activated,

and a negative Arctic Oscillation like signal in the wind stress curl over the Arctic. Consequently, a larger amount of freshwater is stored in the Canada and Makarov Basins when the form drag is applied.

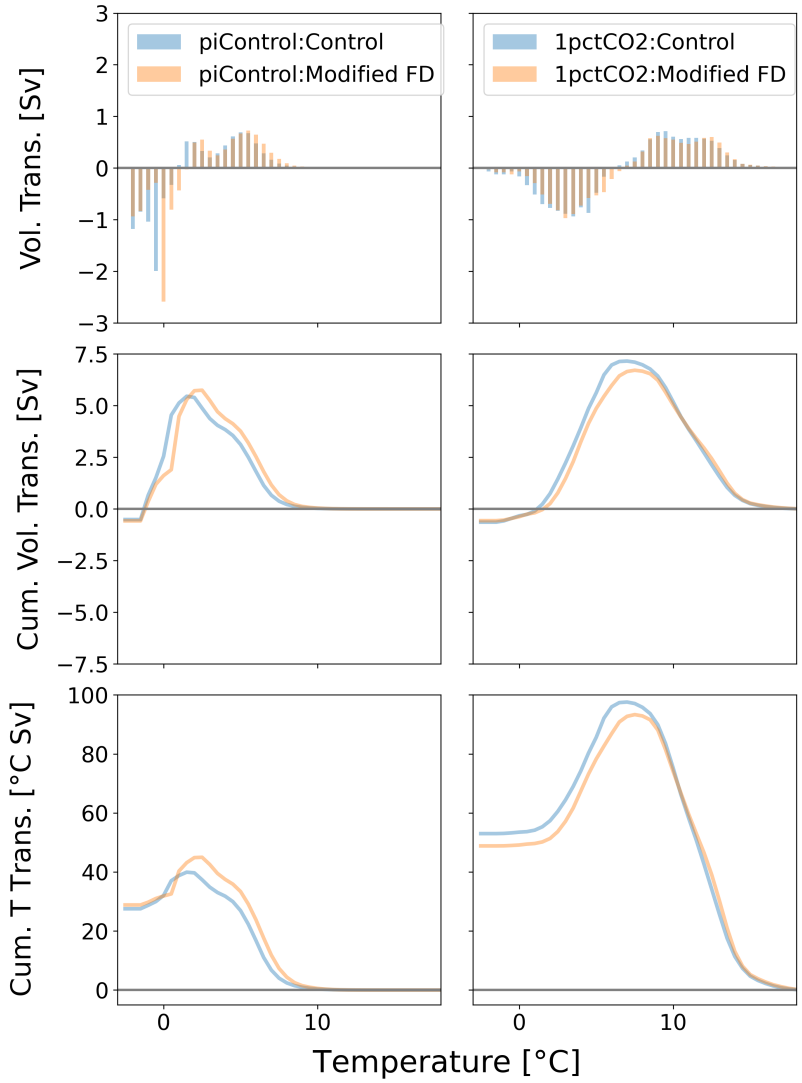

Figure 6: Exchange of volume (positive northward) and heat (relative to 0 °C) at the Arctic gateways (Fram Strait, Barents Sea Opening, Bering Strait, and Davis Strait) in HadGEM3-LL. Panels on the left column show the exchanges during the last 100 years of pre-industrial control climate simulation (piControl) for the CMIP6 (blue) version of the model and for the modified form drag version of the model (orange). The panels on the right are similar, but for the last 30 years of the 1pctCO2 experiments. Note that the 1pctCO2 control represents a mean over four ensemble members.

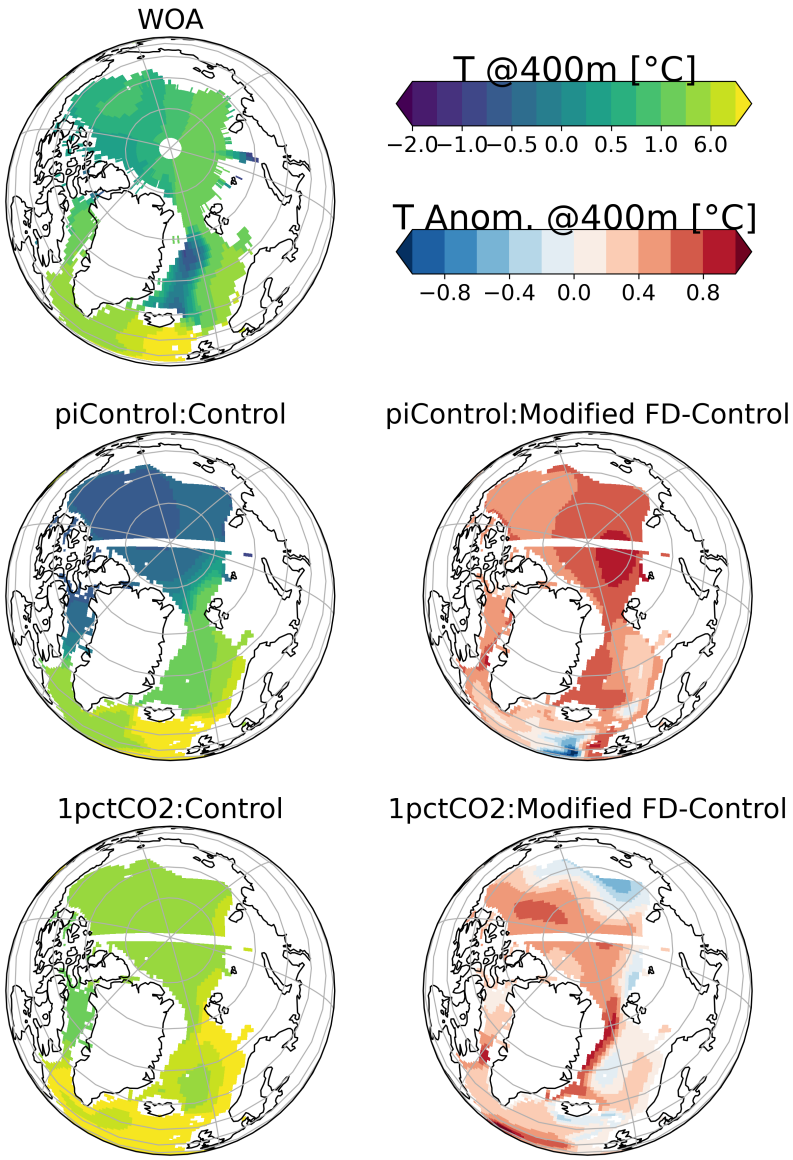

Figure 7: Annual mean temperature at 400 m depth in the Subpolar North Atlantic and the Arctic in observations (WOA) and in HadGEM3-LL. Panels on the right show the comparison between the simulation with the modified form drag and the standard CMIP6 simulation. For piControl we use the time mean is taken over the last 100 years, whereas for the 1pctCO2 the time mean is taken over the last 30 years of the simulation. Note that the 'control' for the 1pctCO2 simulation is a mean over four ensemble members.

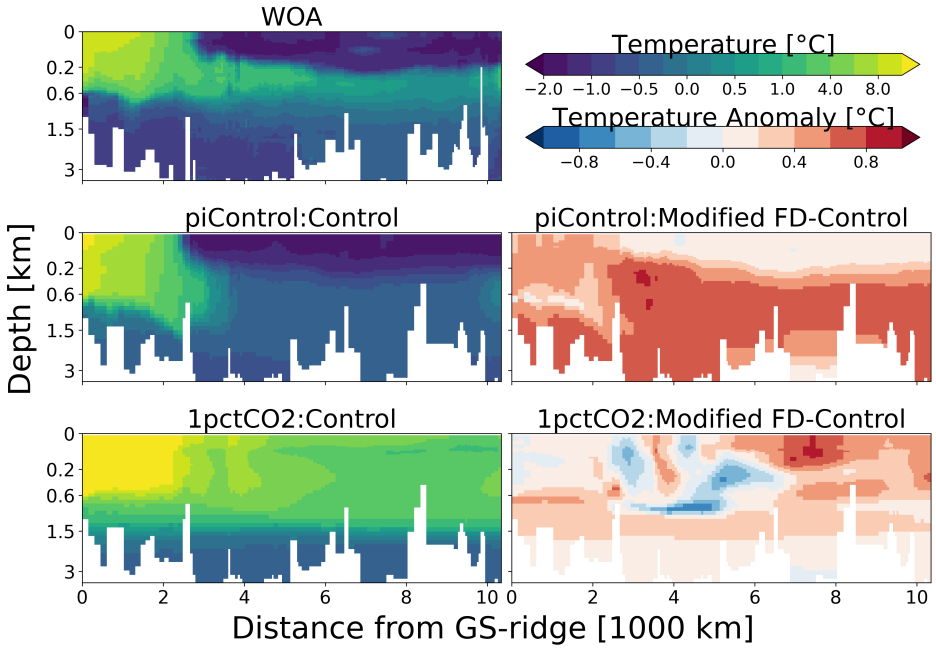

Figure 8: Annual mean temperature section along the Atlantic Water pathway from Greenland-Scotland Ridge (GS) around the Arctic ending in Fram Strait in observations (WOA) and in HadGEM3-LL. Panels on the right show the comparison between the simulation with the modified form drag and the standard CMIP6 simulation. Note that the '1pctCO2: control' is a mean over four ensemble members.

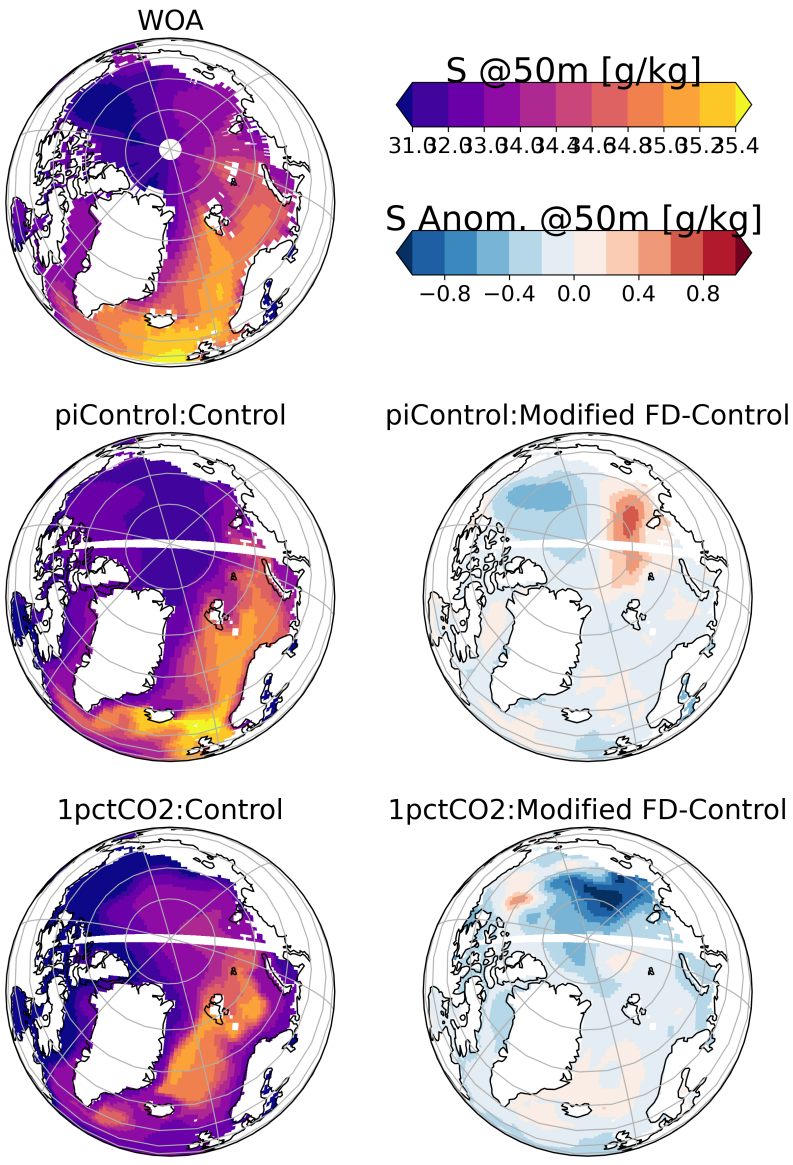

Figure 9: Same as Fig. 7, but for annual mean salinity at 50 m depth.

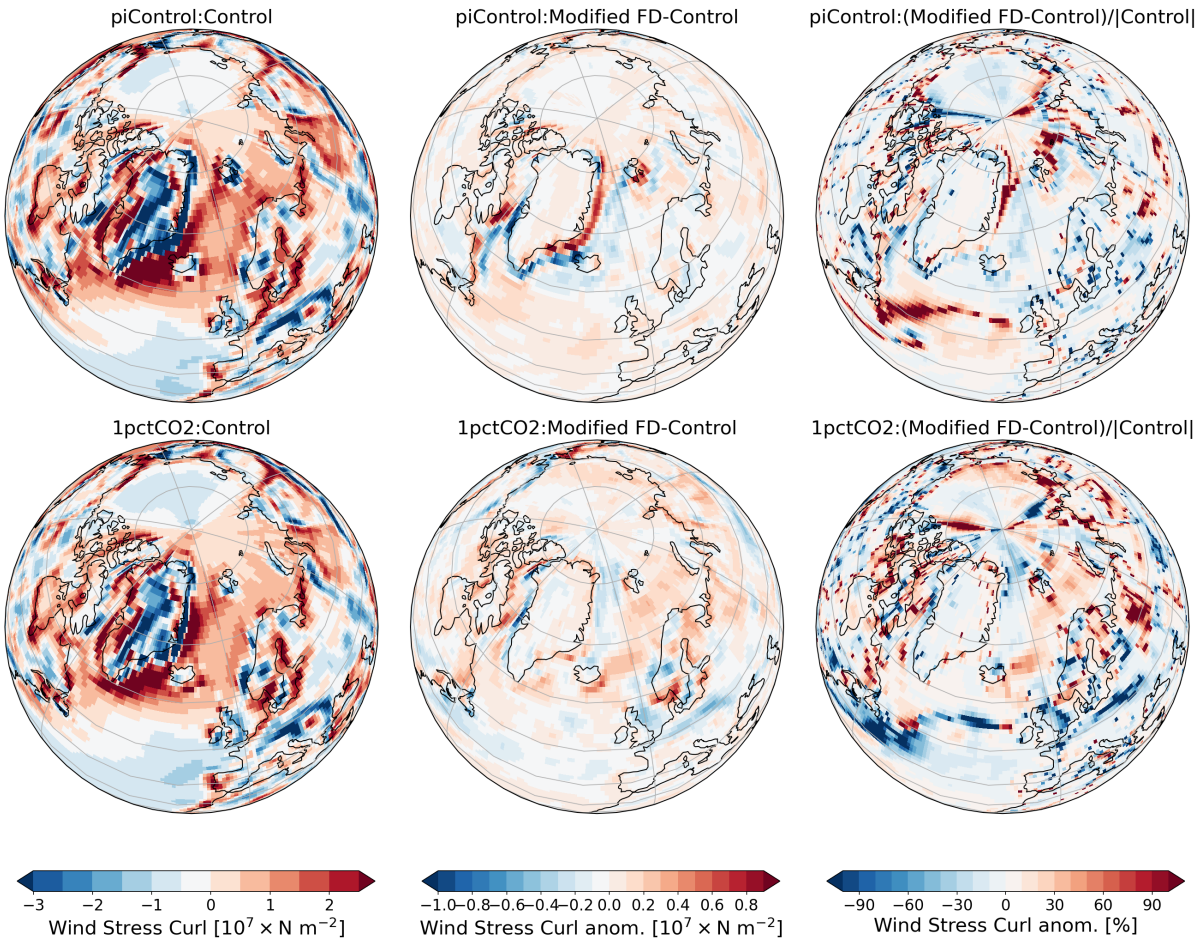

Figure 10: Annual mean Wind Stress Curl in the low CO_2 climate (last 100 years of the piControl; top row) and high CO_2 climate (last 30 years of the 1pctCO2 simulation; bottom row). Note that the '1pctCO2: control' is a mean over four ensemble members.

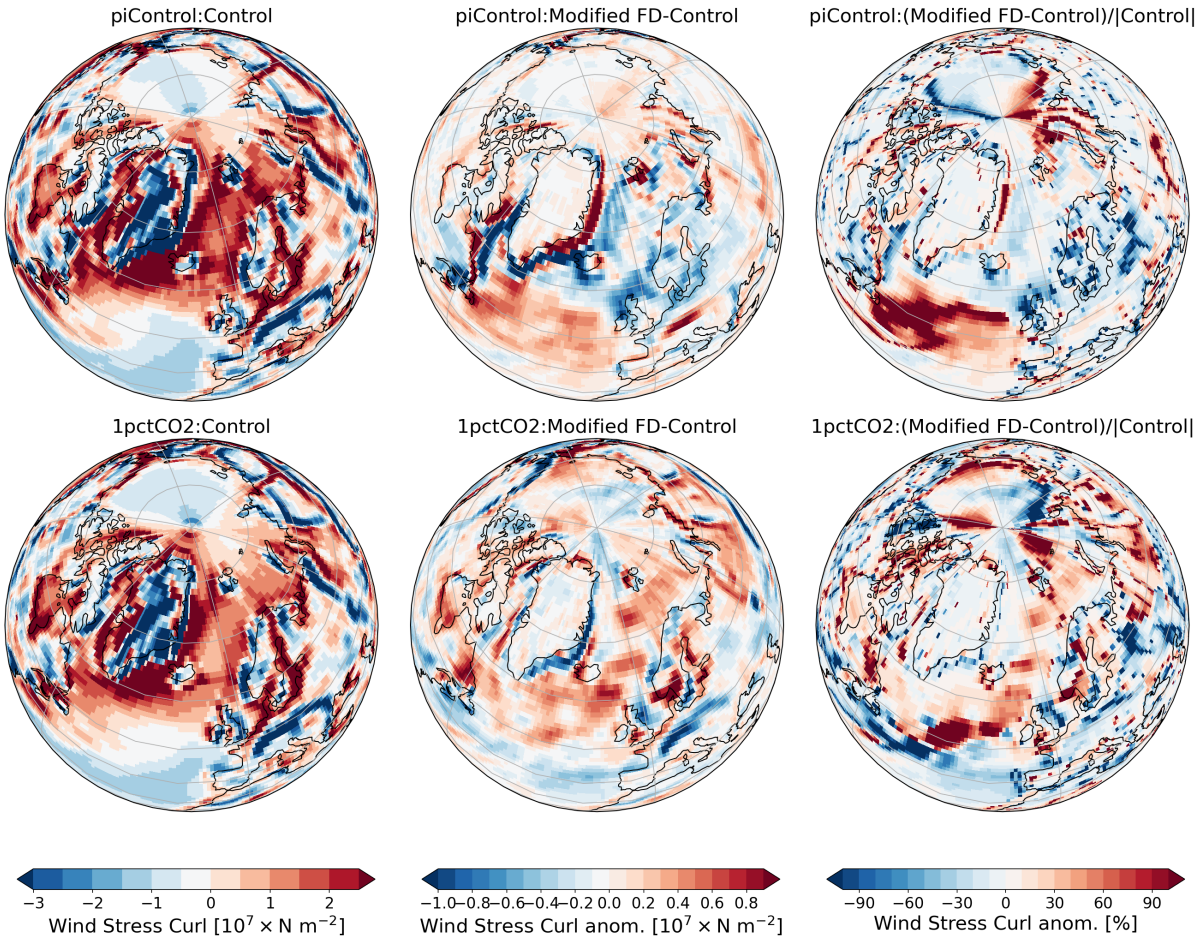

Figure 11: Same as Fig. 10 but the time average is taken only over winter months December, January, and February.

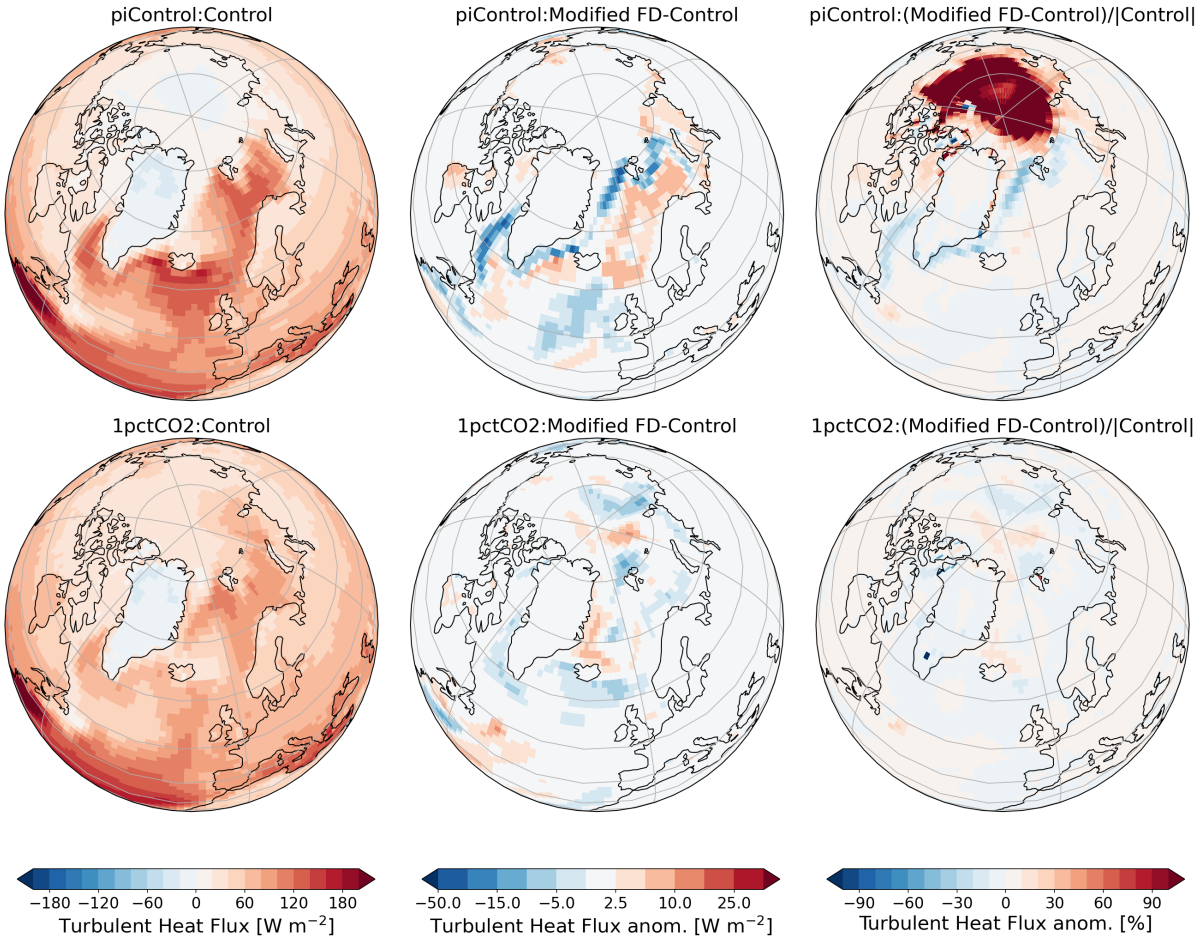

Figure 12: Annual mean turbulent heat flux (sum of latent and turbulent heat fluxes, positive up) in the low CO_2 climate (last 100 years of the piControl; top row) and high CO_2 climate (last 30 years of the 1pctCO2 simulation; bottom row). Note that the '1pctCO2: control' is a mean over four ensemble members.

3.1.2 Impact of form drag on the sea ice and air temperature within AWI-CM1

The impact of the new form drag parameterization in simulations with AWI-CM1 on a few selected climate variables is shown in this section. The internal model variability is quite high so that the aerial extent of statistically significant impact is somewhat limited but nonetheless the impact patterns are coherent and explainable beyond these areas. Shown are the mean differences between the sensitivity runs and controls runs for winter and summer season and the overall mean difference. The marginal ice zone (MIZ) is depicted by showing the isolines of 0.15 and 0.80 SIC.

In AWI-CM1, the effective transfer coefficients over ice in the new parameterization are slightly lower than the default for SIC greater than 0.8 (heat transfer coefficient) to 0.9 (momentum transfer coefficient) and increasingly larger with decreasing SIC (see Fig. 1, bottom). The change in the momentum transfer formulation is reflected in the changes in sea ice drift speed (Fig. 13). In winter, most of the Arctic Basin is covered with sea ice with SIC at or close to 1. Here, the sea ice drift speed is slightly decreased (not significant). The new parameterization only has an effect in the MIZ, where a higher transfer coefficient leads to a significant increase in sea ice drift speed. In summer, the zone with higher ice drift speeds has moved closer to the poles with the MIZ. The overall mean impact (Fig. 13, right) is an increase in sea ice drift speed, significant especially along the ice export routes, East Greenland Current, Labrador Current and coastal currents in the Bering Sea.

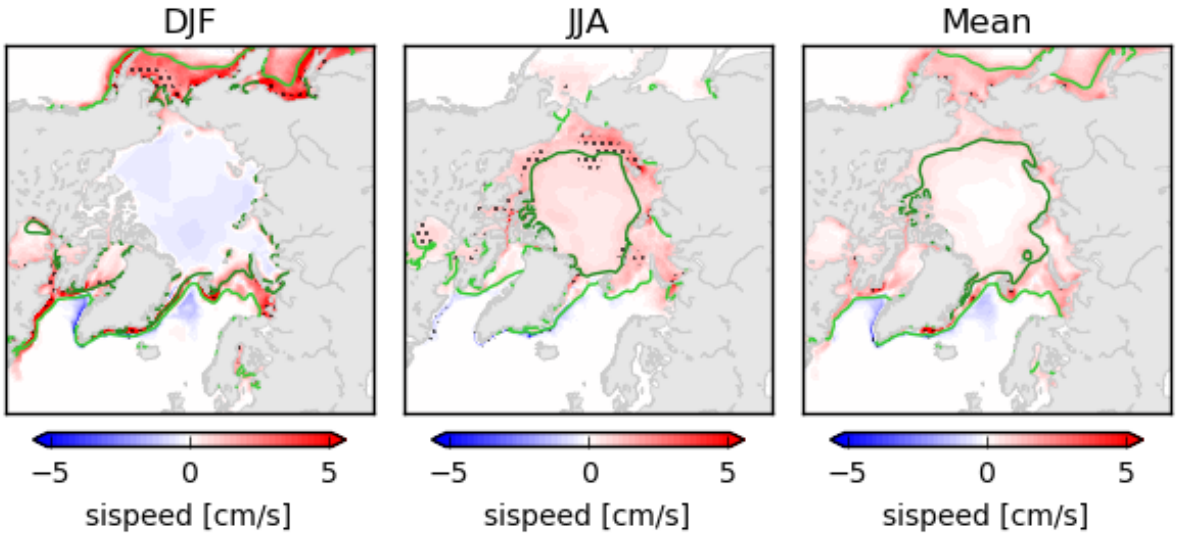

Figure 13: Mean difference (SENS-CTL) in sea ice drift speed [cm s^{-1}] for DJF, JJA, and whole year, black dots show 95% significance. Isolines shown for SIC 15% (lightgreen) and 80% (darkgreen).

A tendency for a decrease in SIC can be observed in the MIZ, but only significantly so around southern Greenland and the Labrador Coast in summer (Fig. 14). This is likely connected to the increased sea ice drift speed and decreased SIT in those areas, which indicate less sea ice volume export at a greater rate so that less sea ice stays present in those areas.

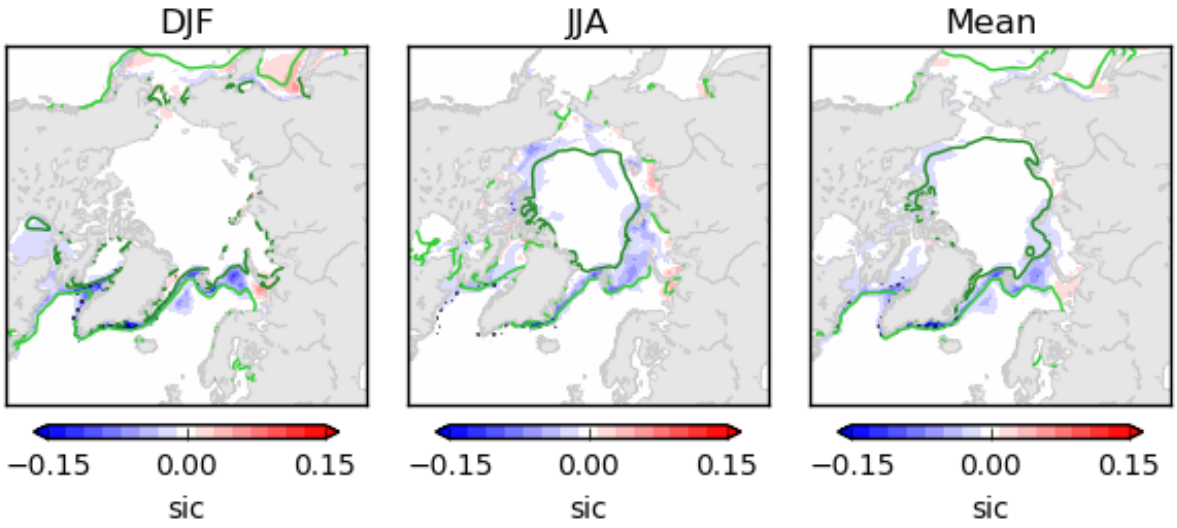

Figure 14: Mean difference (SENS-CTL) in SIC for DJF, JJA, and whole year, black dots show 95% significance. Isolines shown for SIC 15% (lightgreen) and 80% (darkgreen).

Figure 15 shows the difference in 2-m temperature between the sensitivity and control run. The difference in 2-m temperature arises from the inherent change of the heat transfer coefficient with the new parameterization as well as a decrease in sea ice cover. In winter, temperature increase can be observed in and around the Canadian Arctic Archipelago, around Greenland, Svalbard and in the western Barents Sea (statistically significant around southern Greenland). In summer, the temperature increase is concentrated around southern Greenland. The annual mean difference is dominated by the winter difference. SIT is decreased around the perimeter of the Arctic Ocean and around Greenland, there significantly (Fig. 16). The largest SIT decrease occurs north of Greenland and the Canadian Arctic Archipelago.

3.1.3 Impact of form drag on the sea ice within EC-Earth3

Figure 17 shows the differences between form drag parameterization (DRG) and control run (CTRL) in sea ice volume (per unit grid cell area), sea ice velocity, and SIC during March as simulated by EC-Earth3 PRIMAVERA. The maps show the last 5-year mean of the 10-year simulation. A noticeable feature is a reduction in sea ice velocity throughout the Arctic during winter after implementing the Tsamados' form drag parameterization. SIC reduces in the MIZ of the Norwegian Sea during winter. The sea ice volume (per unit grid area) experiences a positive impact in the Southern Beaufort, East Siberian, Laptev, and Kara Seas in winter. A negative impact is discernible in the Fram Strait, Barents, and Norwegian Seas. The ice volume (and ice concentration) decreases because of form drag implementation in the MIZ in winter.

The sea ice velocities decrease at the end of summer (September, Fig. 18) implying that form drag parameterization causes reduced ice mobility in all seasons throughout the Arctic. SIC reduces

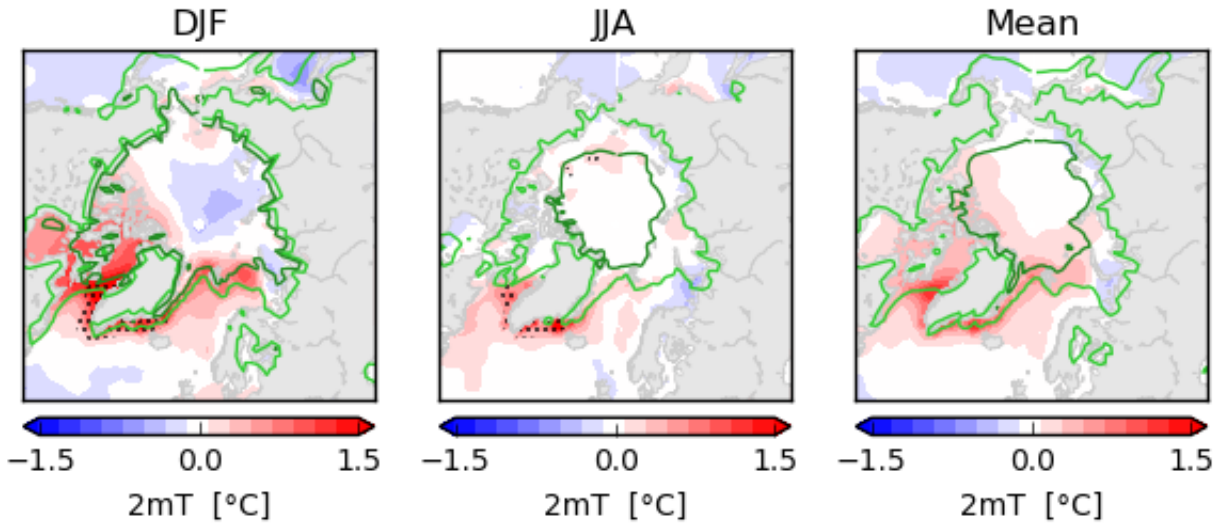

Figure 15: Mean difference (SENS-CTL) in 2-m temperature [°C] for DJF, JJA, and whole year, dots show 95% significance. Isolines shown for SIC 15% (lightgreen) and 80% (darkgreen).

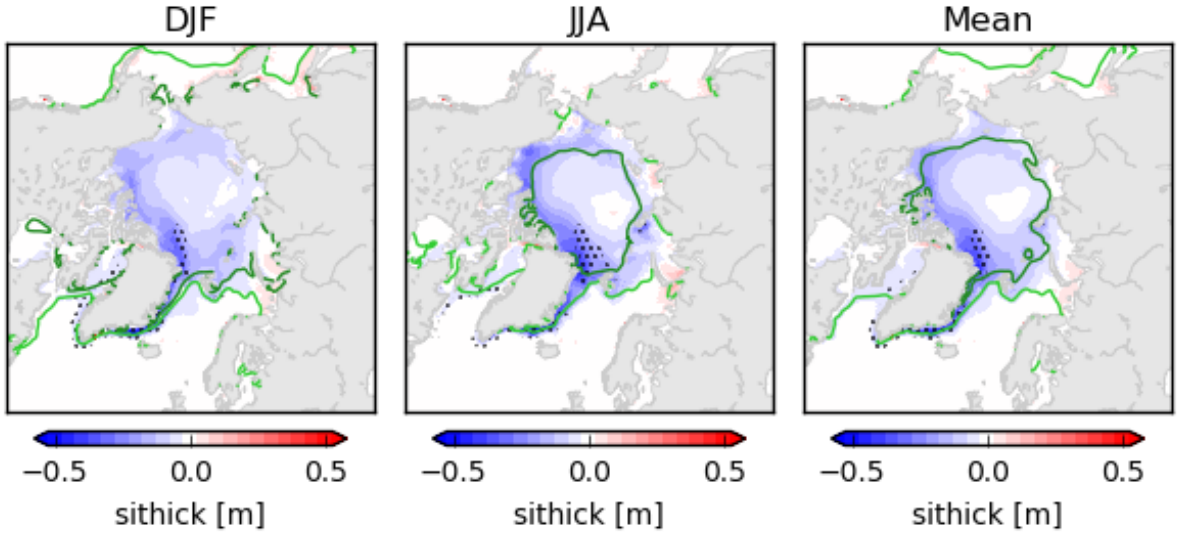

Figure 16: Mean difference (SENS-CTL) in SIT [m] for DJF, JJA, and whole year, dots show 95% significance. Isolines shown for SIC 15% (lightgreen) and 80% (darkgreen).

in the MIZ of the Norwegian Sea during the summer, too. It implies that SIC decreases in both seasons in the MIZ of the Norwegian Sea. However, an increase in September in SIC is discernible in the East Siberian and Southern Beaufort Seas (Fig. 18). Sea ice volume (per unit grid area) increased in the Southern Beaufort and East Siberian Seas, whereas it depleted in the MIZs of the Greenland Sea and the northern Barents Sea. As these coupled simulations are rather short (10

years), there may be unforeseen variability influencing the results. The total ice extent and total ice volume remain the same with some variability in all seasons before and after the form drag implementation. Additional results are presented in Sec. 4.1.1 for experiments in forced mode.

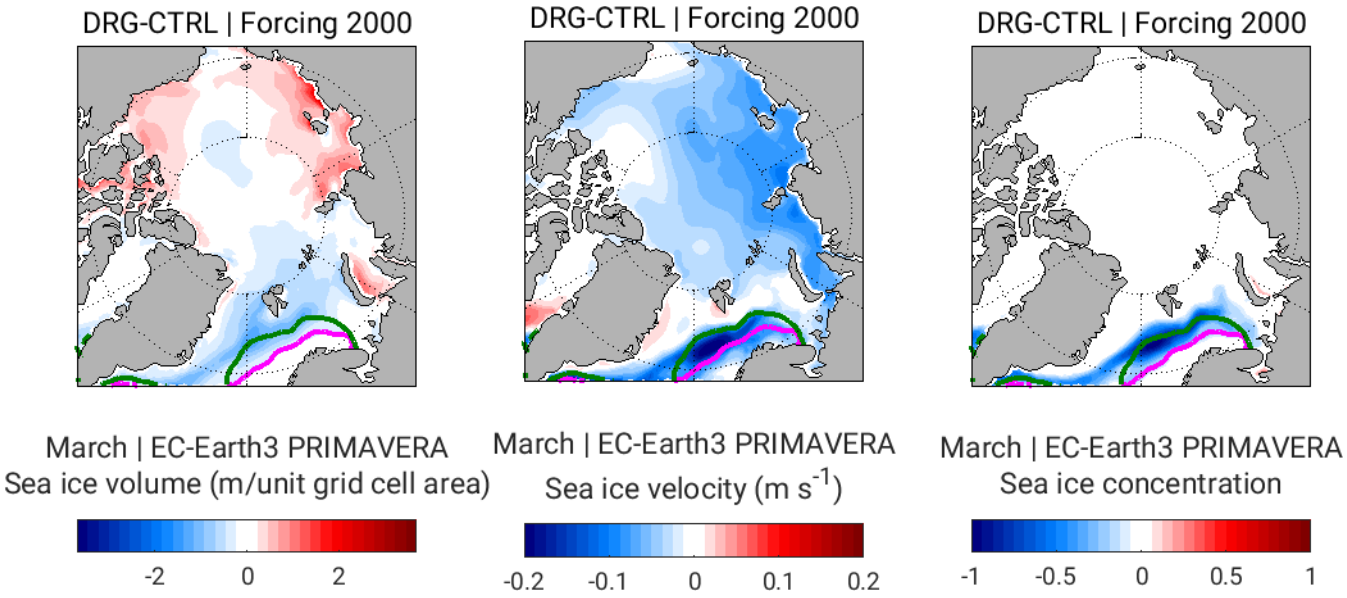

Figure 17: Difference maps of form drag parameterization (DRG) and control run (CTRL) simulated by EC-Earth3 PRIMAVERA. The maps show the last 5-year mean of 10-year run for sea ice volume (per unit grid cell area, m), sea ice velocity, and SIC during March. Magenta (green) solid line is 15% SIC for CTRL (DRG).

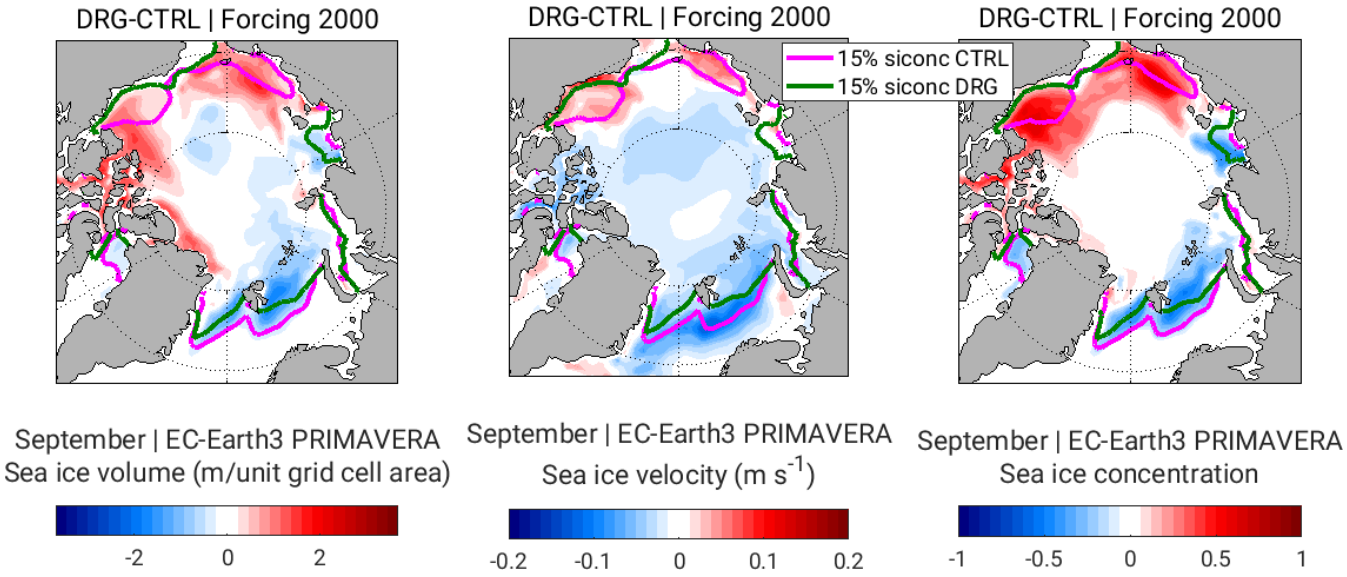

Figure 18: Same as Fig. 17 but for September.

3.2 Melt ponds

3.2.1 Impact of melt ponds on the sea ice and ocean within EC-Earth3

Under modern forcing, an expected impact of melt ponds is to reduce the mean albedo over sea ice. Since the maximum occurrence of melt ponds is in July, we used this month to inspect the impact of the parameterization on the albedo field. Fig. 19 shows that the reduction in mean albedo is discernible mainly near the Central Arctic.

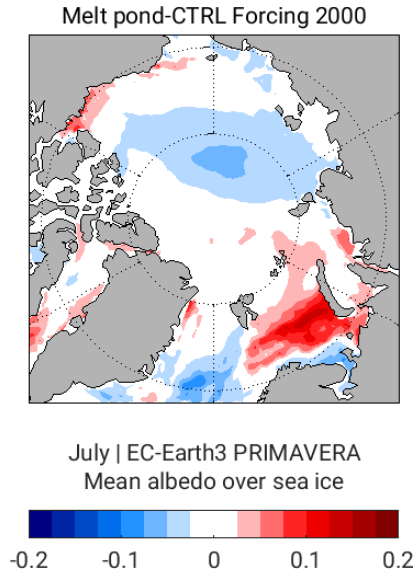

Figure 19: Difference map (Melt pond minus CTRL) of the mean albedo over sea ice for the last 20-year mean of 165-year simulation of EC-Earth3 PRIMAVERA in July for constant greenhouse gas forcing of 2000.

On the other hand, to assess the impact of melt ponds on the winter SIT (and sea ice volume) by having the ponds the previous summer, we choose the month of March. The energy differences because of ice conditions in winter and the end of summer are such that the refreezing of ponds adversely impacts the lateral and vertical sea ice growth. Fig. 20 shows that the melt pond parameterization leads to thinner ice in collocated regions in which the albedo also decreases by applying the parameterization (see Fig. 19). At this stage, we do not have a clear understanding of the increase in the albedo and sea ice thickness in some regions (e.g., Canadian Arctic Archipelago) because of the melt ponds parameterization. This might be an effect of internal variability or due to the time span of the experiments. Further analysis and additional experiments are being conducted to elucidate this issue.

The density scatter plot of mean (July) albedo over sea ice against the mean (March) sea ice volume (per unit grid cell area, Fig. 21) reveals that the regions having reduced albedo over sea ice correspond to thinner sea ice after the melt pond parameterization is activated (note the scarcity of points on the lower-right region in Fig. 21).

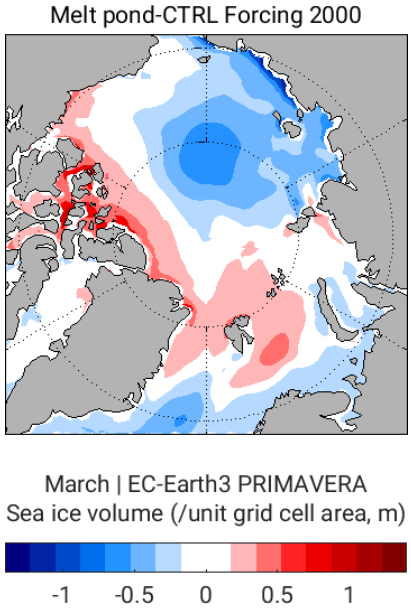

Figure 20: Difference map (Melt pond minus CTRL) of winter sea ice volume per unit grid cell area (m) for last 20-year mean of 165-year simulation of EC-Earth3 PRIMAVERA in March for constant greenhouse gas forcing of 2000.

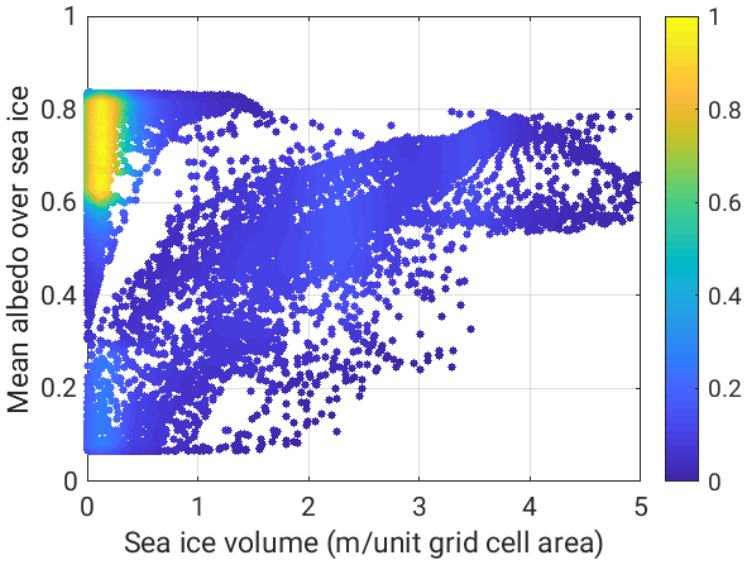

Figure 21: Density scatter plot of mean (July) albedo over sea ice against the mean (March) sea ice volume (per unit grid cell area) for the last 20-year mean of 165-year simulation for constant greenhouse forcing of 2000 after melt pond parameterization in EC-Earth3 PRIMAVERA. Note that zero SIT values (ice-free regions) are removed, although this is not visible in the figure due to the used x-axis scale and density of points.

As shown in Fig. 22, the July SIC (when melt pond occurrence is maximum) also presents a good correspondence with the albedo (Fig. 19) and SIT (Fig. 20) fields. In terms of pan-Arctic sea ice volume and extent, it is difficult to decipher the impact of melt pond parameterization for the entire 165-year time span (Fig. 23). For the first 70 years of the simulation, as the coupled model stabilizes, the melt pond growth remains slow for June, July, and August (Fig. 24). The melt pond area fraction grows almost four times in July compared to June under the constant forcing of 2000.

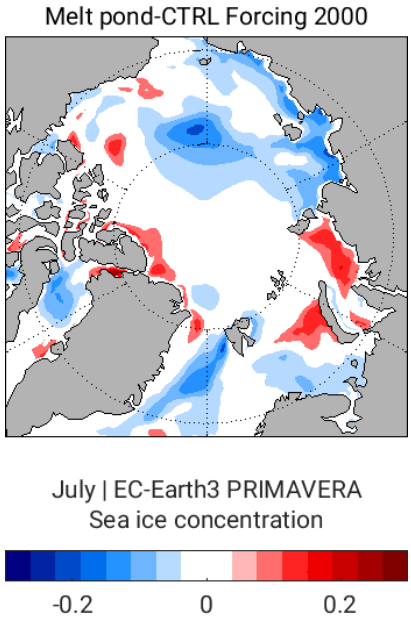

Figure 22: Difference map (Melt pond minus CTRL) of SIC for last 20-year mean of 165-year simulation of EC-Earth3 PRIMAVERA in July for constant greenhouse gas forcing of 2000.

The Atlantic meridional ocean circulation (AMOC) is a major source for decadal and multi-decadal variability in the global and Arctic climate system (Mahajan et al., 2011). An increased net upward flux increases surface air temperature and limits sea ice formation and growth. The low value of maximum AMOC has a direct association with the high sea ice volume/extent and vice versa (Fig. 25a and b). The last 20 years of simulation of melt pond parameterization under constant forcing of 2000 corresponds to a high value of AMOC, which causes less sea ice extent and volume for that forcing as seen in Fig. 23.

The SIT and ice extent time evolution correlate with the maximum AMOC as shown in the 165-year time series (Fig. 25c). Pearson's correlation (r) coefficient between 5-year moving means of SIT (sea ice extent) time series of 165 years and corresponding maximum AMOC at 26°N is $r = -0.45$ ($r = -0.43$), which implies that AMOC and SIT/extent have an inverse correlation.

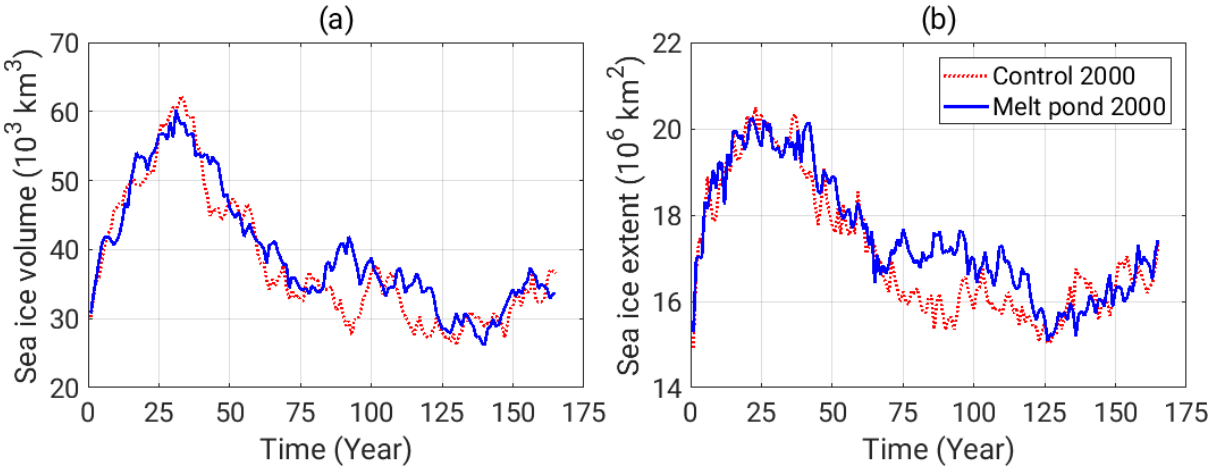

Figure 23: EC-Earth3 PRIMAVERA simulated 165-year time series of March total sea ice volume (a) and total sea ice extent (b) for CTRL and melt pond parameterization for constant greenhouse gas forcing of 2000.

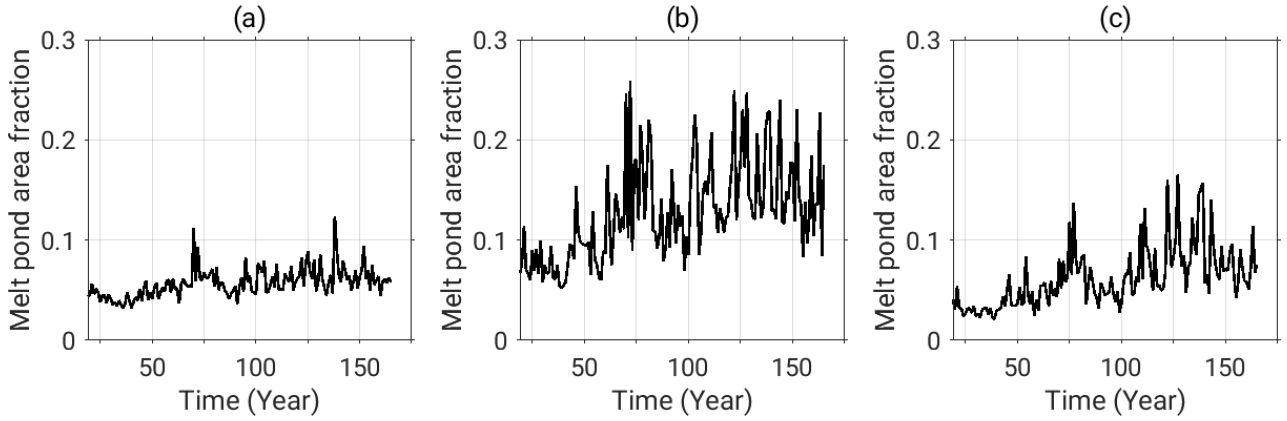

Figure 24: Melt pond area fraction for June (a), July (b), and August (c) as simulated by EC-Earth3 PRIMAVERA under constant greenhouse gas forcing of 2000 for 165 years.

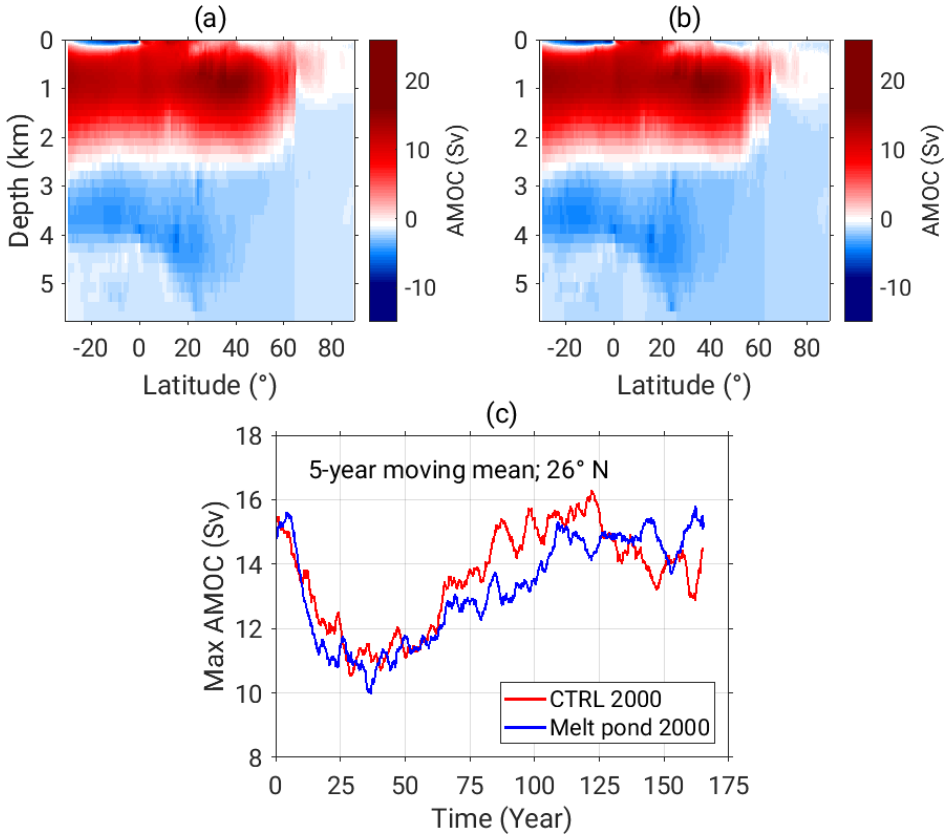

Figure 25: Meridional stream function for Atlantic (AMOC) for CTRL and melt pond parameterization. Last 20-year mean of 165-year run (a) CTRL 2000, and (b) Melt ponds 2000. (c) Time series of the maximum AMOC at 26°N for both simulations.

3.3 Multilayer snow scheme

3.3.1 Impact of the ECMWF snow scheme in coupled global weather forecasts

Snow on land

The setup of the numerical experiments is the same of that described in detail in Arduini et al. (2019) and in D2.3. In short, global coupled land-atmosphere forecasts with the ECMWF's IFS (CY45R1) are performed with the single-layer (FC-SL) and multilayer (FC-ML) snow schemes using a horizontal resolution of 30 km and 137 vertical levels, with the lowest model level being located at about 10 m above the ground. Ten-day forecasts are initialized each day between December 2016 and March 2017, at 00 UTC from the ECMWF operational analysis.

The case-study analysed in D2.3 at Sodankyla indicated that the current IFS underestimates the amplitude of the diurnal cycle of the 2-m temperature (T2m), compared to observations. The use of the multilayer snow scheme increases the amplitude of the diurnal cycle of T2m, reducing the diurnal cycle amplitude bias. This is due in particular to the improvement in the representation

of the minimum temperatures. In the following, we show that this result is also confirmed at the hemispheric scale and considering a longer time period. For this purpose, we use the T2m observations of the surface synoptic weather station network (SYNOP) to validate the results.

As shown in Fig. 26, the forecasted daily minimum (Tmin) and maximum temperature (Tmax) are generally lower and higher, respectively, for forecasts using the multilayer snow scheme than the ones using the single-layer snow scheme. This implies a larger amplitude of the diurnal cycle over snow-covered surfaces, corroborating the results for a single site, presented in D2.3, at the global scale. Looking separately at Tmin and Tmax, a widespread positive bias for Tmin is seen in the FC-SL experiments in most of the NH apart from central Europe, over which a small negative bias of about -0.5 °C is present (see Fig. 26a). In the FC-ML, a lower Tmin is obtained during wintertime over the NH (seeFig. 26b), leading to a reduction of the positive bias by more than 1 °C over east Eurasia, Scandinavia, and North America (see Fig. 26c).

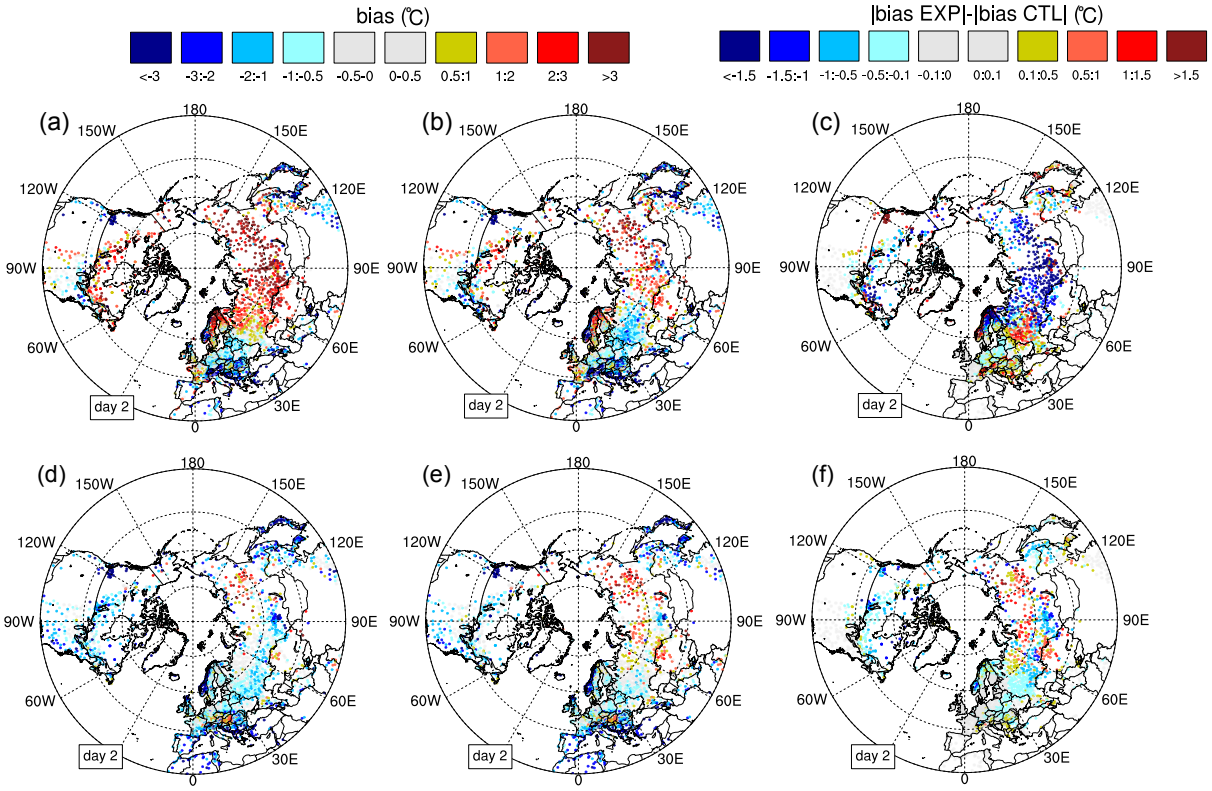

Figure 26: Top row: bias of the daily minimum 2-m temperature of the coupled forecasts performed for DJF 2016/2017 using the (a) single-layer (FC-SL) and (b) the multilayer snow scheme (FC-ML), at a lead time of two days; (c) difference of the absolute value of the bias between FC-ML and FC-SL for DJF 2016/2017, at a lead time of two days; blue colours imply a reduction of the bias in FC-ML compared to FC-SL, red colours an increase of the bias. Bottom row: same as the top row, but for the daily maximum 2-m temperature at a lead time of two days.

The Tmax bias is weaker in magnitude than the bias in Tmin, and it shows more spatial

variability (see bottom row of Fig. 26). A cold daytime bias in the FC-SL (as for instance in Europe and North America) is consistent with an underestimation of the amplitude of the diurnal cycle with respect to observations. For these regions, Tmax is higher in FC-ML, which means that the bias with respect to observations is reduced compared to the FC-SL experiment. However, for regions in which a positive (warm) bias in Tmax is present in FC-SL (e.g., in the eastern part of Eurasia), the bias is enhanced in FC-ML due to the increased amplitude in the diurnal cycle. These findings also hold for longer lead times (Day 5, not shown). The increase of the bias in these regions can be attributed not only to the overestimation of the diurnal cycle but also to errors in the representation of the temporal evolution of the daily mean temperature. This is illustrated in Fig. 27, which shows the time series for February 2017 of the T2m and total cloud cover averaged over stations between 120°E – 180°E and 50°N – 75°N. The diurnal cycle amplitude for T2m in the FC-ML experiment is closer to the observed one than that for FC-SL. However, the mean diurnal temperature is overestimated in both experiments, therefore leading to larger errors in Tmax in FC-ML. This can be partially explained by the overestimation of cloud cover over the region that keeps the model temperature too warm (see bottom of Fig. 27). However, other sources of error, for instance, related to cloud phase, surface albedo, sensible heat flux or turbulent mixing in stable conditions, can also contribute to these errors (as was also discussed in Day et al. (2020)).

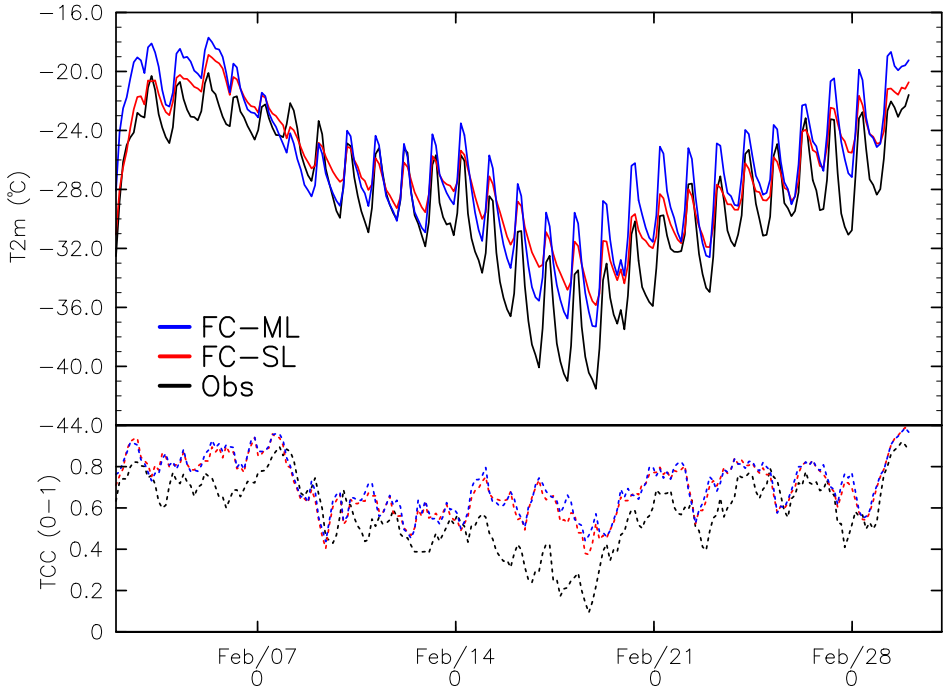

Figure 27: Concatenated day 2 (t+24 to t+47) forecasts of 2-m temperature (°C, top panel) and total cloud cover (0-1, bottom panel) averaged over stations between 120°E-180°E and 50°N-75°N for February 2017 from the coupled forecast experiments using the single-layer (FC-SL, red line) and the multilayer (FC-ML, blue line) snow scheme, compared to observations (Obs, black line).

When considering the entire Arctic region however, the mean error of 2-m temperature is reduced

at all lead times in FC-ML (see Fig. 28). The relative improvement of FC-ML compared to FC-SL increases at longer lead times; for instance, at day 4 in the forecast the bias is reduced from a value of 0.6 K to 0.3 K when using the multilayer snow scheme.

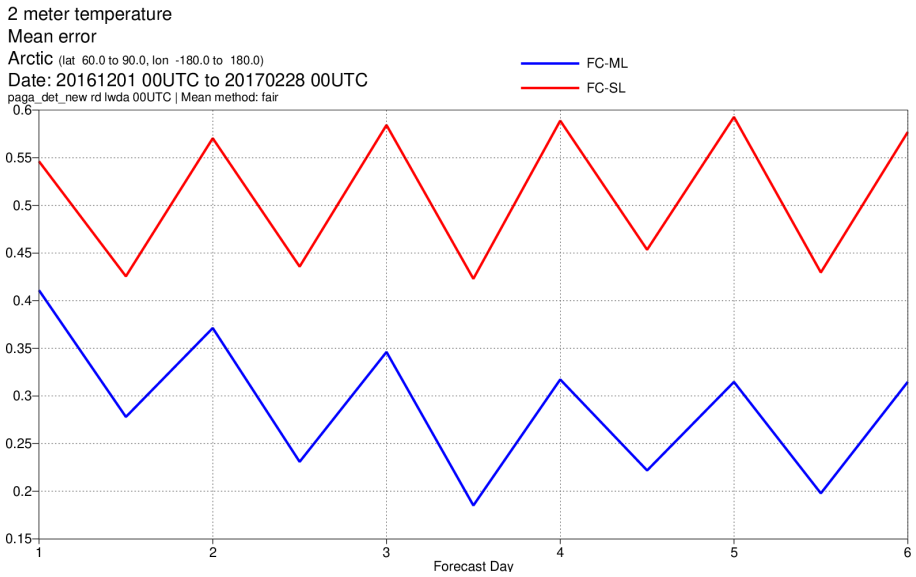

Figure 28: Mean error (bias, °C) of 2-m temperature as a function of lead time (days) for the Arctic region (northward 60°N) for the coupled forecast using the single-layer (FC-SL, red) and the multilayer (FC-ML, blue) snow scheme.

The impact of the new multilayer snow scheme on upper-air scores, e.g., the root-mean-square-error (RMSE) of geopotential height at 500 hPa in the North Hemisphere, was found nearly neutral on the time scales considered (see Fig. 29).

Snow on sea ice

The analysis of the case study discussed in D2.3 highlighted the importance of the snow insulation for the representation of the skin temperature variability during wintertime over the Arctic sea ice. However, the results also highlighted the role of the compensation between cloud errors and errors in the surface-atmosphere coupling, due to the strong influence of the cloud radiative properties on the surface temperature variability in the Arctic winter.

To evaluate the impact on the wider Arctic region and on a longer time period, coupled ocean-land-atmosphere forecasts using IFS CY45R1 are performed with the multilayer snow scheme (ML) activated both over land and sea ice for the period 1st December 2014 to 28th February 2015. Forecasts are initialised every day at 00 UTC from ERA5 reanalyses and run for 5 days. An experiment with no snow over sea ice is used as a reference (CTL). The horizontal resolution used is about 30 km with 137 vertical levels, with the lowest model level being located at about 10 m above the ground. In the current formulation, the use of ML over sea ice surfaces does not allow the advection of the snowpack properties with the ice floes. Therefore, the snow depth from LIM2

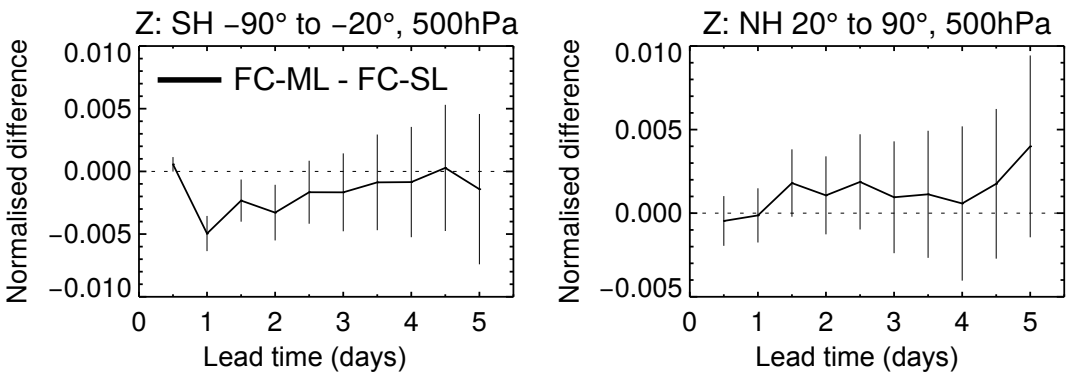

Figure 29: Normalized difference in regional root-mean-square-error (RMSE) for DJF 2016/2017 for geopotential height at 500 hPa between forecasts with the multilayer snow scheme and single-layer snow scheme, compared to the operational analysis. Negative differences mean that using a multilayer snow scheme reduces the RMSE. Vertical bars display the 95% confidence intervals.

is used as an input every coupling time-step in the surface energy budget computation which is done in the atmospheric/land component of IFS. The ML scheme included in the land scheme of IFS (HTESSEL) is thus used in the surface energy budget computation to update the snow temperature, which is then used in the coupling with the atmosphere. Additional details on the implementation of the multilayer snow scheme over sea ice is reported in D2.3.

The surface temperature over sea ice is evaluated using satellite ice surface temperature observations from the Copernicus Marine Environmental Monitoring Service (CMEMS, available at https://resources.marine.copernicus.eu/?option=com_csw&view=details&product_id=SEAICE_ARC_SEAICE_L4_NRT_OBSERVATIONS_011_008). A pre-processing of the observations was required to remove cloud-covered pixels. Indeed, for these points a spatial interpolation using the neighbouring pixels was used in the original dataset, to fill spatial gaps. Also, it should be noted that the satellite observations provide information on the daily mean surface temperature, because the dataset is formed by a composite of many passages of the satellite within a day over the same area. Because satellite observations were only available from 1st January 2015, the comparison of the model's data with this dataset covers only the time period between 1st January 2015 to 28th February 2015.

The simulated daily mean skin temperature of CTL is affected by a positive bias of several degrees over the Arctic region, compared to the satellite observations (Fig. 30). Such errors are consistent with what reported in previous studies when ERA5 data were considered (see for instance Batrak and Müller (2019)). The magnitude of the bias is larger in the Central Arctic and near Greenland, whereas it is lower on the Siberian and Alaskan side. The bias is largely reduced in the ML experiment, with areas of near-zero bias in the Siberian and Alaskan regions (Fig. 30). When

averaged over grid cells with a sea ice cover fraction larger than 0.9, the bias of the daily mean skin temperature at day 2 of the forecast is 7.8 K for CTL, whereas it is reduced to 3.2 K for ML. At day 5, the daily mean bias is 7.3 K for CTL and 3.1 K for ML.

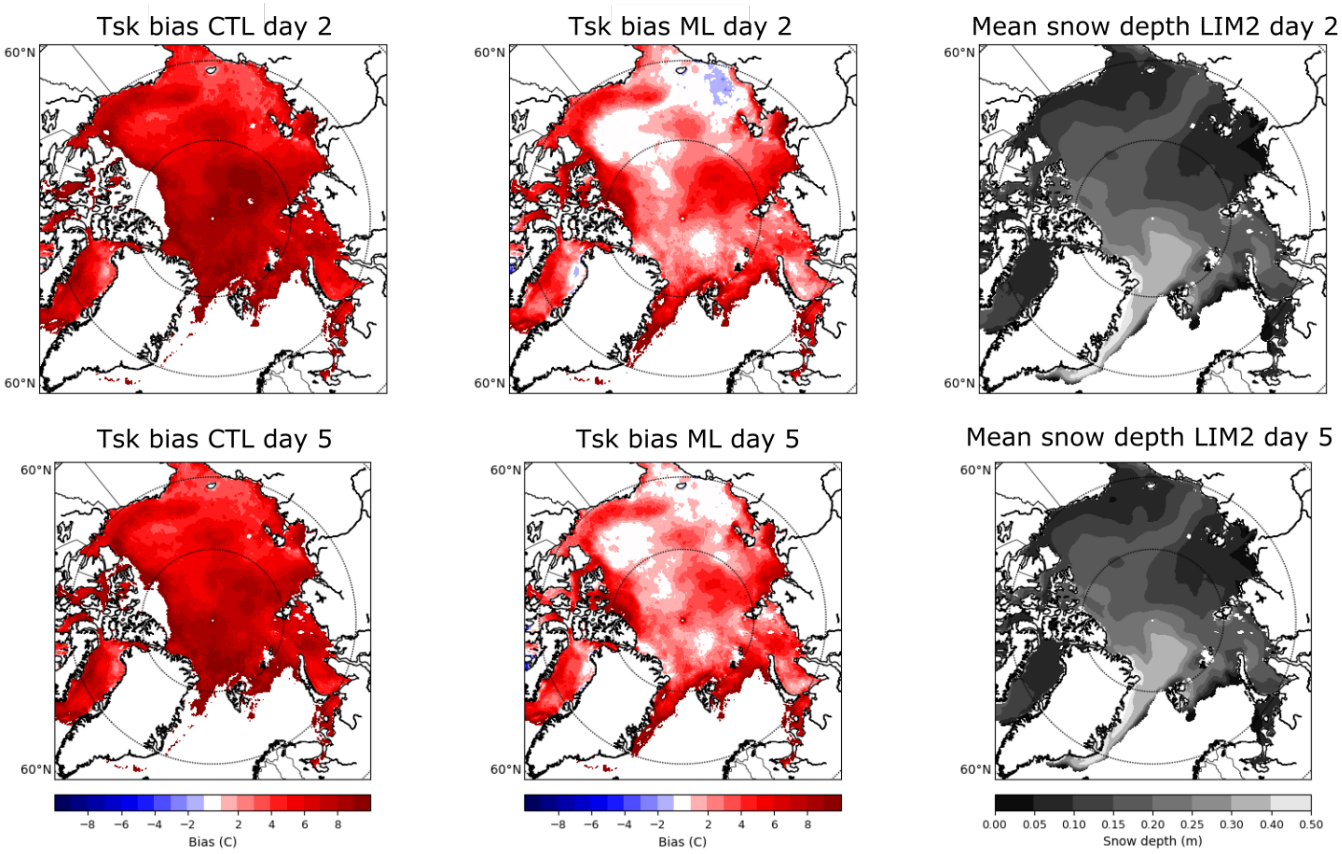

Figure 30: Bias of simulated daily average skin temperature (Tsk) with respect to the CMEMS satellite surface temperature observations of the coupled forecast with no snow over sea ice (CTL, left) and with the multilayer snow scheme (ML, centre) at a lead time of 2 days (top row) and 5 days (bottom row) from 1 January 2015 to 28 February 2015. Right column: mean snow depth over sea ice between 1 January 2015 and 28 February 2015 in the sea ice model LIM2 at a lead time of 2 days (top row) and 5 days (bottom row).

The spatial pattern of the biases is consistent to some extent with the larger snow accumulation in the Central Arctic and near Greenland, compared to the Siberian side, as simulated in LIM2 (see Fig. 30, right column). However, the spatial variability of snow depth alone does not fully explain the spatial variability of the bias. It should be noted that the snow depth accumulating in LIM2 can have biases due to errors in the precipitation amount in the atmospheric model, as well as in the LIM2 snow parameterizations. Another factor which can influence the surface temperature variability is the ice thickness, which is fixed to 1.5 m in the current IFS. However, in reality the winter sea ice varies in space and time, being thicker in the Central Arctic and near Greenland

than in the Siberian and Alaskan side (Ricker et al., 2014). This can lead to a larger heat flux from the warm ocean underneath towards to surface in the regions with shallower sea ice, and a stronger thermal decoupling between the atmosphere and ocean in region with thicker ice. An improved coupling between the atmospheric and sea ice models is required to take into account such effects on the sea ice surface temperature, which was explored as part of WP2 Task 2.2.2 and reported in D2.2.

The previous analysis indicates that the insulation effect of snow over sea ice largely affects the surface temperature representation over the Arctic region. Therefore, one might expect an impact also in the upper-air fields. To evaluate the relative effect of the snow on sea ice only, an additional experiment with the multilayer snow scheme activated only over land surfaces is performed (ML-Land). Figure 31 shows biases of geopotential height at 850 hPa for CTL, ML (in which the ML scheme is used both over land and over sea ice) and ML-Land, with respect to the ECMWF operational analysis, at a lead time of 48 hours. Representing snow over sea ice leads to a general reduction of the geopotential height in the Central Arctic region, compared to CTL and ML-Land, due to the increased cooling in the lower part of the atmospheric boundary layer. Both CTL and ML-Land have a positive bias in this region, therefore indicating a positive impact of ML on the geopotential height. However, the evaluation against the ECMWF operational analysis should be taken with caution over the Central Arctic region, because of the caveats with assimilating observations in polar regions (Lawrence et al., 2019). Future work is needed to evaluate the impact of the representation of snow over sea ice on the upper-air fields using observations, as the ones collected from recent Arctic field campaigns like MOSAiC.

In conclusion, the evaluation in coupled forecast mode of the multilayer snow scheme over the north Hemisphere confirms the positive impact on the 2-m temperature diurnal cycle, as previously reported in a case-study analysed in D2.3. A detailed discussion on the evaluation of the coupled forecasts with the new multilayer snow scheme is reported in Arduini et al. (2019) and Day et al. (2020).

The use of a multilayer snow scheme reduces the positive bias of the daily minimum 2-m temperature by more than 1 °C over most of the high-latitude regions at different lead times, compared to in situ observations (see Fig. 26). Considering the Arctic region (northward 60°N), the 2-m temperature bias is reduced at all lead times (see Fig. 28).

The increased amplitude of the diurnal cycle can have a detrimental impact on the maximum 2-m temperature, in particular over regions characterized by a preexisting positive bias of the daily mean temperature (see Fig. 26 and Fig. 27). Indeed, using multiple vertical layers for the description of the snowpack only directly impacts the heat transfer within the snowpack and thus the diurnal cycle amplitude. The net radiative forcing at the surface is mainly controlled by other processes such as cloud cover/microphysics or albedo, affecting incoming radiation and its partitioning (see for instance Day et al. (2020)). Hence, despite improvements in the responsiveness of snow-covered surfaces with respect to the atmospheric forcing and the ability to represent different time scales, there are also other substantial errors in polar regions that need to be addressed, such as cloud

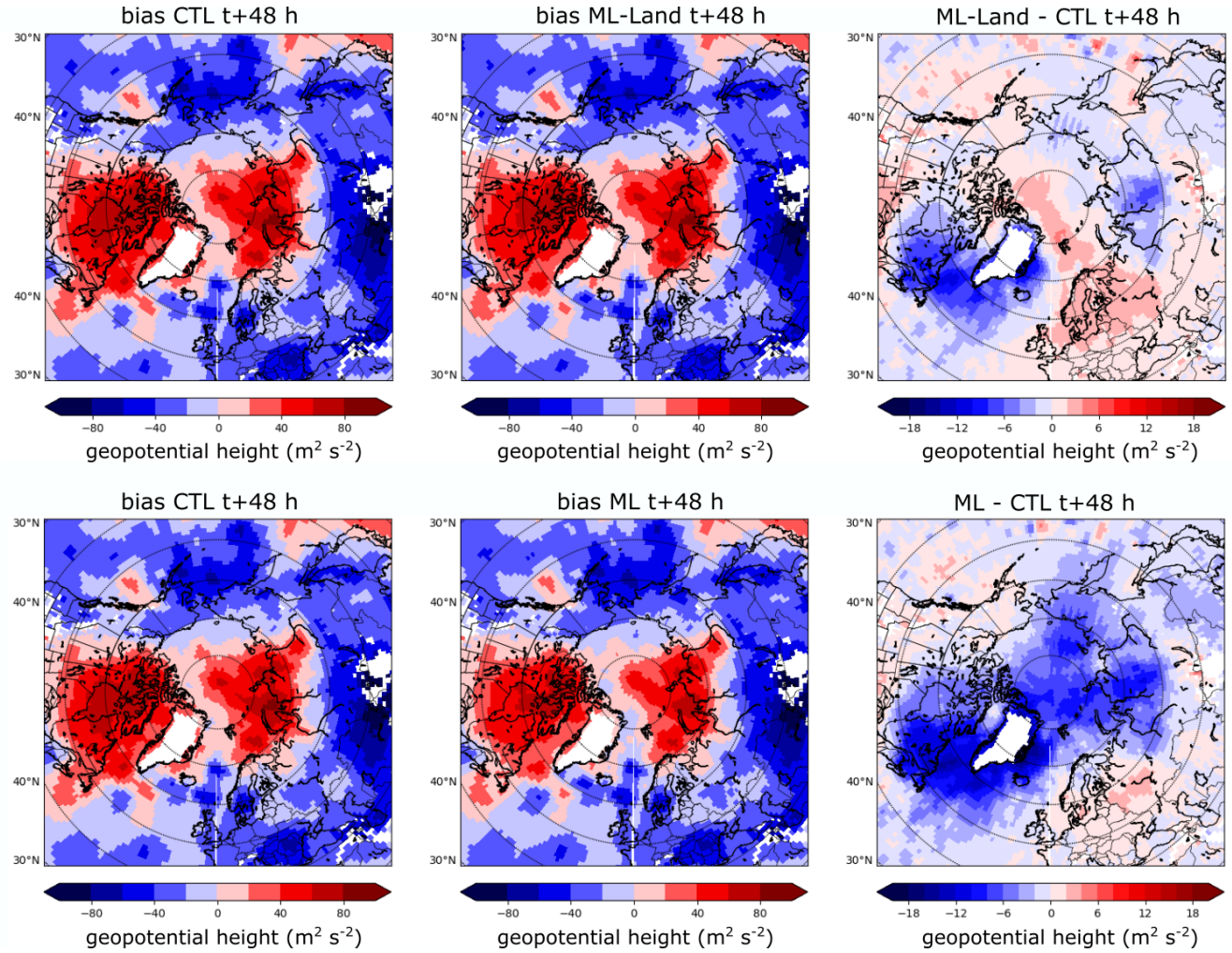

Figure 31: First row: (left and centre) Bias of the geopotential height at 850 hPa of the coupled forecasts with the single-layer snow scheme and no snow over sea ice (CTL) and with the multilayer snow scheme over land only (ML-Land), compared with the ECMWF operational analysis, and (right) mean difference between ML-Land and CTL. Bottom row: as the top row, but for CTL (left), forecasts with the multilayer snow scheme both over land and sea ice (ML, centre) and ML – CTL (right). Forecasts are evaluated for the time period DJF 2014/2015.

radiative properties, or poor representation of the turbulent mixing.

The impact of the new multilayer snow scheme on upper-air scores, e.g., geopotential height at 500 hPa in the North Hemisphere, was found nearly neutral on the time scales considered.

The comparison with satellite observations of surface temperature indicates that the current IFS model overestimates the sea ice surface temperature by several degrees during wintertime, in particular over the Central Arctic and north of Greenland during the winter 2014/2015. The

experiment with the multilayer snow scheme activated over sea ice surfaces discussed here reduces to a large extent such bias, demonstrating the importance of accounting for the presence of snow over sea ice surface. The impact is not only restricted to the near-surface atmosphere, but propagates in the boundary layer with an effect on the geopotential height at 850 hPa. However, the case-study analysed in D2.3 indicated that an underestimation of liquid water clouds in the Arctic can lead to the increase of errors when a multilayer snow scheme is used, because of the compensation between cloud radiative forcing errors and the response of the surface fluxes to an incorrect forcing. Therefore, an evaluation of cloud phase errors and their occurrence in operational forecasts is a necessary step before the activation of a multilayer snow scheme over sea ice surfaces. Another parameter that can influence the surface temperature variability, and not considered in this report, is the SIT, which is fixed to a value of 1.5 m in the current IFS. An improved coupling between the atmospheric and sea ice models is required to take into account such effects on the sea ice surface temperature, which was explored as part of WP2 Task 2.2.2 and reported in D2.2.

3.4 Landfast ice

3.4.1 Impact of landfast ice on the sea ice within EC-Earth3

This section describes the impact of landfast ice parameterization implemented in EC-Earth3 PRIMAVERA on the sea ice conditions. The simulations with fast ice developments lead to more realistic sea ice conditions under constant greenhouse forcing of 2000 (Fig. 32). This is discernible in the Canadian Arctic Archipelago (April maximum fast ice extent) where fast ice is a common occurrence towards the end of winter. The realistic sea ice conditions attribute to the reliable climatology for constant forcing of 2000.

The fast ice parameterization creates lower ice thickness in the Laptev Sea than that in CTRL for constant forcing of 2000, with a small variability likely caused by the short duration of the simulation (10 years, Fig. 33a). However, the model underestimates the SIC in the Barents Sea (Fig. 33b). The fast ice regions of the Canadian coast are also observable upon implementing the parameterization (Fig. 33a).

Despite some success of the fast ice parameterization as compared to Environment and Climate Change Canada (ECCC) observational data, there are shortcomings and limitations of the scheme (see Figs. 34, 35, and Sec. 2.4.1). The sea ice simulated as fast ice in the experiment (Fig. 33a) in parts of eastern Kara Sea seems to partly agree with the observations in Fig. 35a. The sea ice velocity is very low in magnitude in the regions of expected fast ice zones, e.g., East Siberian Sea coastal region, Mackenzie River delta, Canadian Arctic Archipelago, and the coastal regions of Laptev Sea. The fast ice simulations could further improve by representing the coastal salinity for the river delta regions (e.g., Mackenzie River, Ob River). There can also be an underestimation of fast ice because of the lower freezing point of the seawater.

The fast ice parameterization by Lemieux et al. (2015) and Lemieux et al. (2016) implemented in the global coupled model EC-Earth3 PRIMAVERA improves the fast ice simulations in the regions such as coastal regions of the East Siberian Sea, the Mackenzie Delta, and the Laptev Sea.

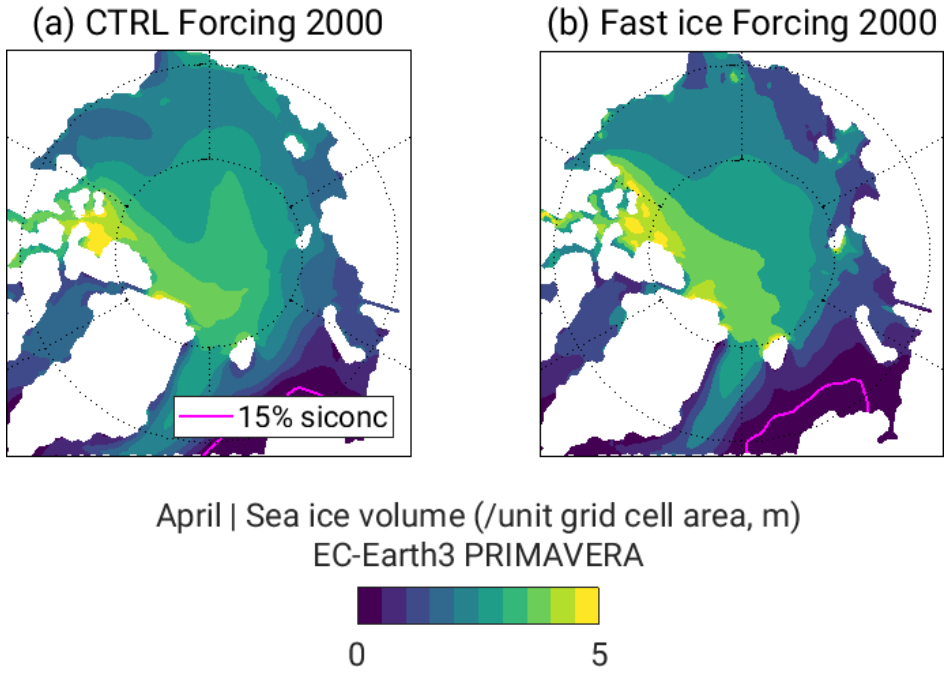

Figure 32: Sea ice volume (per unit grid cell area) for the last 5-year mean of 10-year simulation using EC-Earth3 PRIMAVERA in April, (a) CTRL, and (b) fast ice parameterization for constant greenhouse gas forcing of 2000.

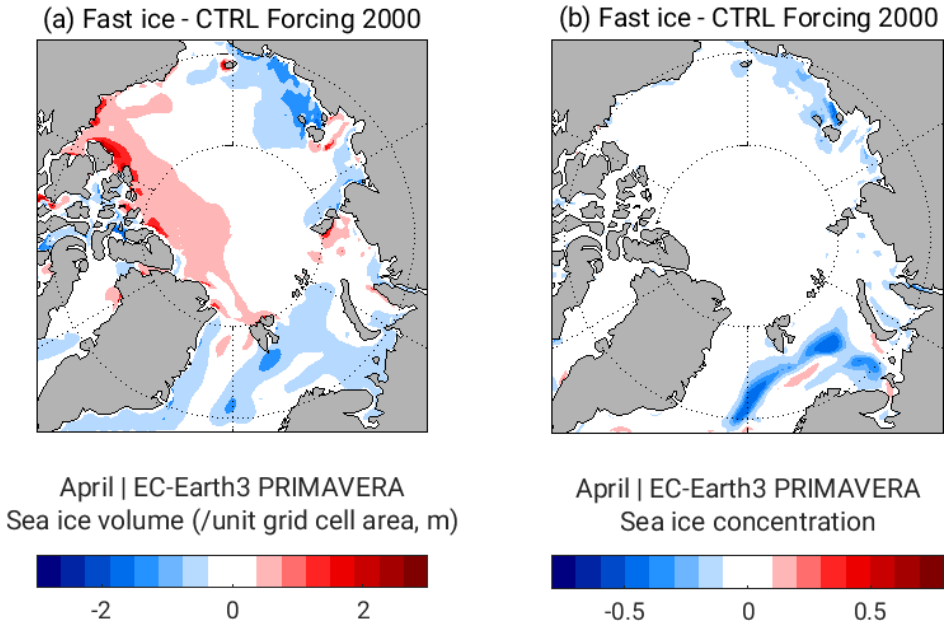

Figure 33: Difference maps of CTRL and sea ice volume (per unit grid cell area) (a), SIC (b) after implementing fast ice parameterization for the last 5-year mean of 10-year simulation using EC-Earth3 PRIMAVERA in April for constant greenhouse gas forcing of 2000.

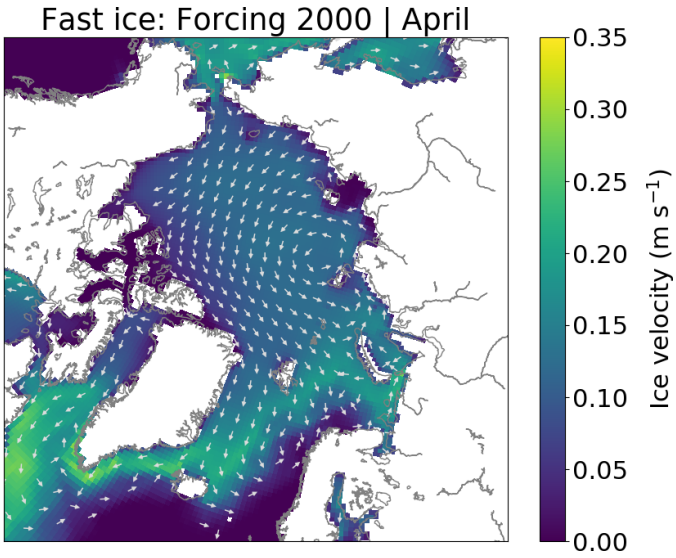

Figure 34: Sea ice velocity vectors (last 5-year mean of 10-year run) for fast ice parameterization sensitivity experiments in April for constant forcing 2000. The vectors are of equal length representing the direction of ice motion.

Parts of the Kara Sea region show underestimation of fast ice, likely because of deeper bathymetry and large freshwater (i.e., low salinity) influx from the Ob and Yenisey Rivers. The uniaxial and the isotropic tensile strength of sea ice representation in NEMO3.6-LIM3 improves fast ice formation (ice arching).

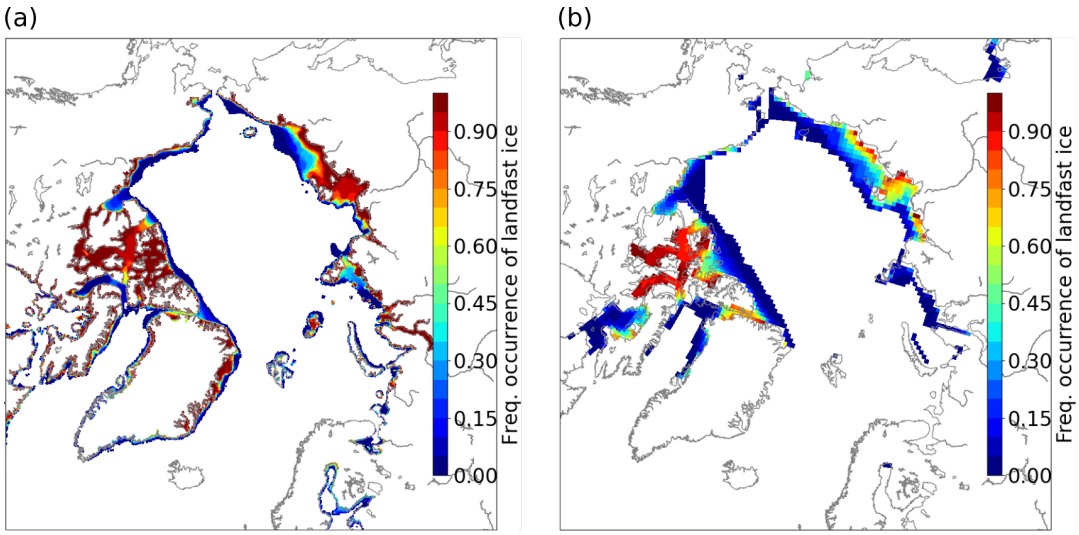

Figure 35: (a) Frequency of occurrence of landfast ice from January to May between 2006 and 2015 for the ECCC observational dataset and (b) last 5 years of 10-year run with constant greenhouse gas forcing 2000 (left).

We draw the following conclusions from these sensitivity experiments: (1) Simulations with fast ice developments lead to more realistic sea ice conditions under constant greenhouse forcing of 2000. These ongoing sensitivity experiments are being continued for 100 years (or more). (2) The sea ice velocity is very low in magnitude in the regions of expected fast ice zones, as supported by evidence from ECCC observational data (see Fig. 35 and Sec. 2.4.1). (3) The combined use of adjusted isotropic tensile strength and basal parameterization in the model improves the results.

3.5 Floe size distribution

3.5.1 Impact of floe size distribution on the sea ice within EC-Earth3

Figure 36 shows the difference maps of SIT and SIC between two simulations during August. The maps show the last 5-year mean of EC-Earth3 PRIMAVERA simulation of 10 years for constant greenhouse gas forcing of 2000. The impact of FSD parameterization is distinct in both the maps. A small value of β (0.6) corresponds to small floe lengths, and a large value of β (1.4) corresponds to large flow lengths. A large (small) floe length causes a larger (smaller) drag coefficient. The positive difference (in red) is discernible in the circumpolar regions of the Arctic (Fig. 36a). It implies that the larger floes dominate in the circumpolar Arctic, where MIZs are prevalent and significant changes in ice thickness occur in these regions. The negative difference (in blue) shows dominant small floes that correspond to the small drag coefficient (Fig. 36a). These minor changes occur in the Central Arctic, where ice thickness decreases.

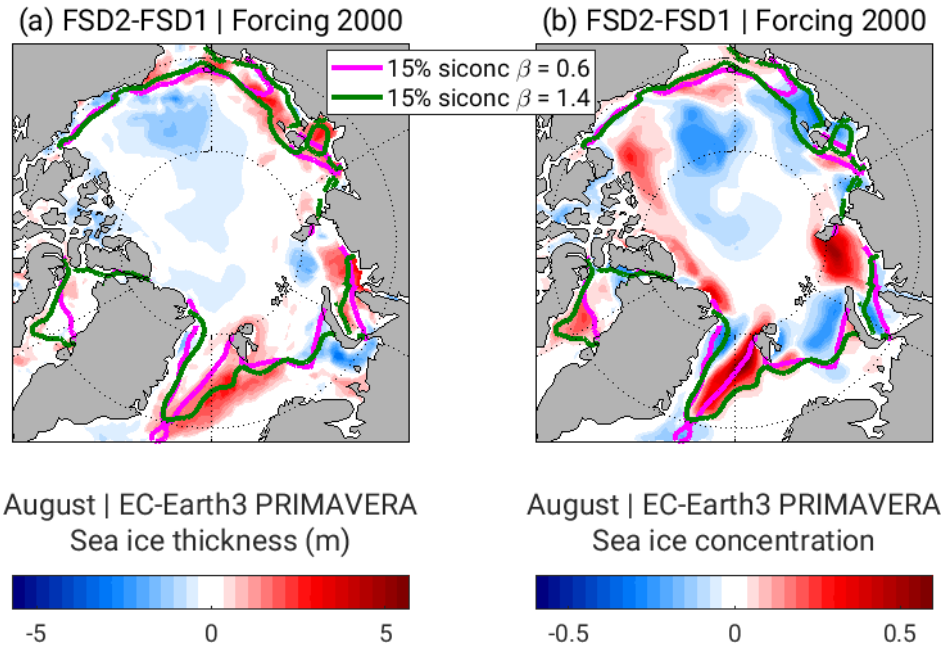

Figure 36: Difference maps of floe size distribution parameterization FSD1 ($\beta = 0.6$) and FSD2 ($\beta = 1.4$) simulated by EC-Earth3 PRIMAVERA for constant greenhouse gas forcing 2000. The maps show the last 5-year mean of 10-year run for SIT (a) and SIC (b) during August.

A change in the value of β explains a large part of the variability in the drag coefficients and SIC in different ice edge zones. In August, the circumpolar Arctic becomes agile. The SIC sees an increase in these regions. Parts of the Canada Basin and the East Siberian Sea undergo a reduction in SIC because of small ice floes and little drag coefficient. However, a large part of the Central Arctic sees no change in ice concentration as there are no MIZs in the region (Fig. 36b). The green line in Fig. 36b shows 15% SIC for FSD1 ($\beta = 0.6$), and magenta line shows 15% ice concentration for FSD2 ($\beta = 1.4$). The ice extent is similar in both cases except that when ice floes are small (i.e., $\beta = 0.6$) the extent is a bit larger compared to when floe size is large ($\beta = 1.4$).

The parameterization of floe size distribution in the EC-Earth3 PRIMAVERA shows that large ice floes cause growth in SIT and ice concentration in the MIZs of the circumpolar Arctic during August.

3.6 Impact of increased model resolution on the Arctic atmospheric response to CO_2 forcing

Four models (CNRM-CM6-1, HadGEM3-GC3.1, MPI-ESM1-2, and GISS-E2-G) are analysed following Lu and Cai (2009). The changes in surface temperature are estimated by the difference between the first and last 30 years of the 140-year simulations (the first 30 years roughly represent the 20th-century climate and the last 30 years represent a transient state with the quadrupling of the CO_2 concentration). The Arctic region is defined as all grid-points north of 60°N. We consider that grid-points are land if the land fraction is greater than 95%. The surface albedo feedback (SAF), changes in cloud radiative forcing (CRF), changes in surface sensible and latent heat fluxes (TURB), changes in heat storage (HEAT), and changes in the clear-sky downward infrared radiation (CS_LWD) are analysed for the various simulations. Note that HEAT does include the heat storage in both land and ocean and also the ocean heat transport. Contributions to changes in surface temperature are coming from the five processes described above plus the non-SAF-induced change in clear-sky shortwave radiation (NOSAF_SW), for instance, due to water vapor absorption changes associated with a warmer and moister atmosphere due to the CO_2 concentration increase (see Lu and Cai (2009), 2009 for the derivation and details).

Figure 37 shows that the Arctic surface warming due to CO_2-increase is strongly amplified in autumn and winter compared with late spring and summer (with a 10 °C difference north of 75°N between winter and summer warming, see the ALL panel) as expected from previous studies. Note also that the linearization slightly reduces the amplitude of the temperature changes at low latitudes but maintains the Arctic seasonal cycle changes (compare panels ALL with REC). Let us now focus on the main physical drivers for summer and winter (note that winter here is taken as extended winter, roughly from October to March).

The first thermodynamic factor for a small Arctic warming amplification in summer is that the main positive driver – the surface albedo feedback SAF (due to large sea ice loss) – is largely cancelled out by the negative cloud radiative feedback CRF at midlatitudes up to 75°N. At higher latitudes, the heat storage (HEAT), and to a lesser extent, the turbulent flux (TURB) and non-SAF-

induced change in clear-sky shortwave radiation (NOSAF_SW) negative terms are also opposing the positive SAF contribution.

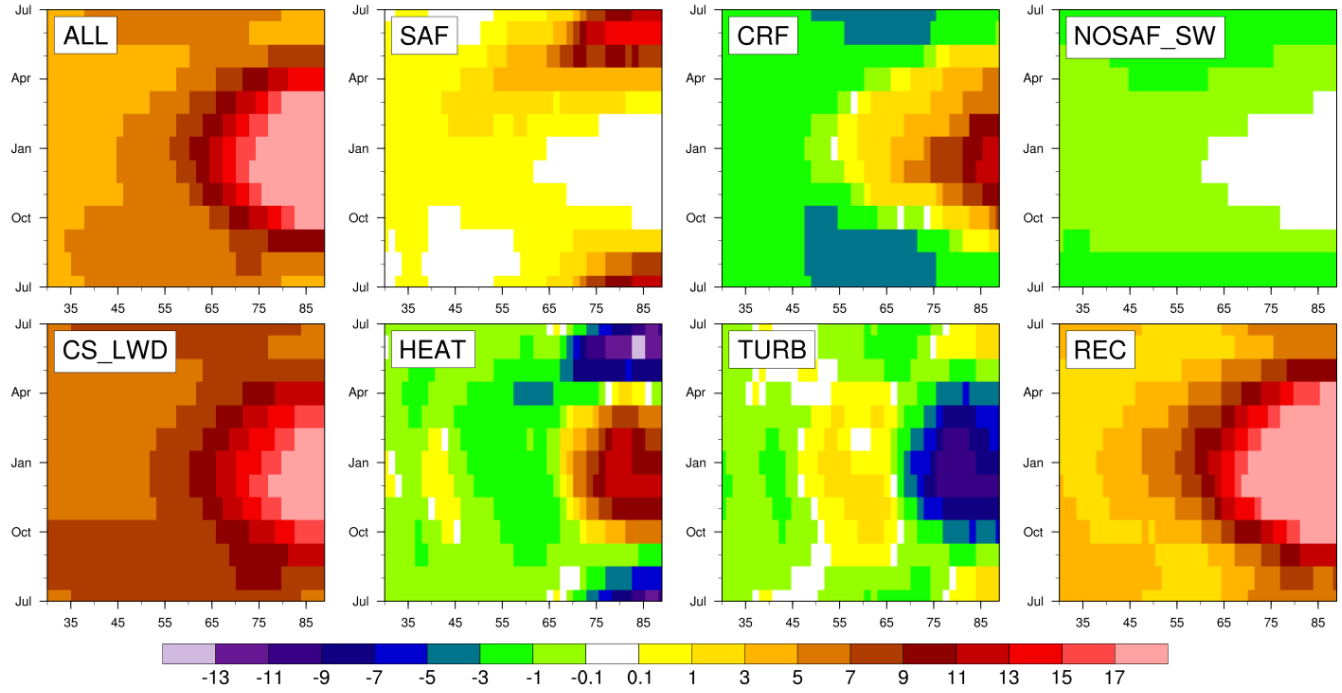

Figure 37: Seasonal cycle (Y-Axis) of the multi-model mean zonal-averaged surface temperature change (in K) at quadrupling CO_2 concentration over mid- to high latitudes (X-Axis) of the Northern Hemisphere: (ALL) the total Arctic warming; the partial temperature changes due to (SAF) surface albedo feedback, (CRF) the change in surface cloud radiative forcing, (NOSAF_SW) the non-SAF-induced change in clear-sky shortwave radiation, (CS_LWD) the change in net clear-sky longwave radiation fluxes, (HEAT) the change in heat storage, and (TURB) the changes in surface sensible/latent heat fluxes, respectively; (REC) the sum of the 6 previous contributions. Negative/positive values indicate heat storage/release for HEAT and negative TURB values indicate turbulent fluxes from the ocean to the atmosphere.

The SAF is naturally much weaker in winter compared to its importance in summer and thus, as expected, does not contribute to the pronounced Arctic amplification in winter. The main driver of the high-latitude winter surface warming amplification, in terms of both spatial patterns and temporal amplitude, is related to changes in clear-sky downward longwave radiation (CS_LWD). It is tempting to associate the CS_LWD contribution mostly with the enhanced CO_2 concentration and increased downwelling infrared radiation. However, Lu and Cai (2009) point out that this is only a small part of the CS_LWD term. This suggests the crucial importance of other atmospheric processes, such as changes in the vertical atmospheric temperature profile, water vapor feedback and other dynamical feedbacks associated with the enhancement of poleward moist static energy transport. The HEAT (positive and thus indicating winter heat release following summer heat

storage) and CRF are the other secondary contributors to increasing surface temperature while the remaining one – TURB – cancels out the heat release contribution. As expected, NOSAF_SW does not play any role in winter.

Let us now focus on the multi-model ensemble spread for these different processes (Fig. 38). The model spread displays large amplitude (>6 K) at high latitude (>75°N) in summer for SAF and HEAT and in winter for CS_LWD, HEAT, TURB and CRF to a lesser extent. In contrast, the spread magnitude is much smaller outside the Arctic (south of 60°N). The large amplitude of the spread (about 50% of the forced signal) clearly suggests that the selected models do have quite different representations of the main processes/drivers of surface Arctic amplification.

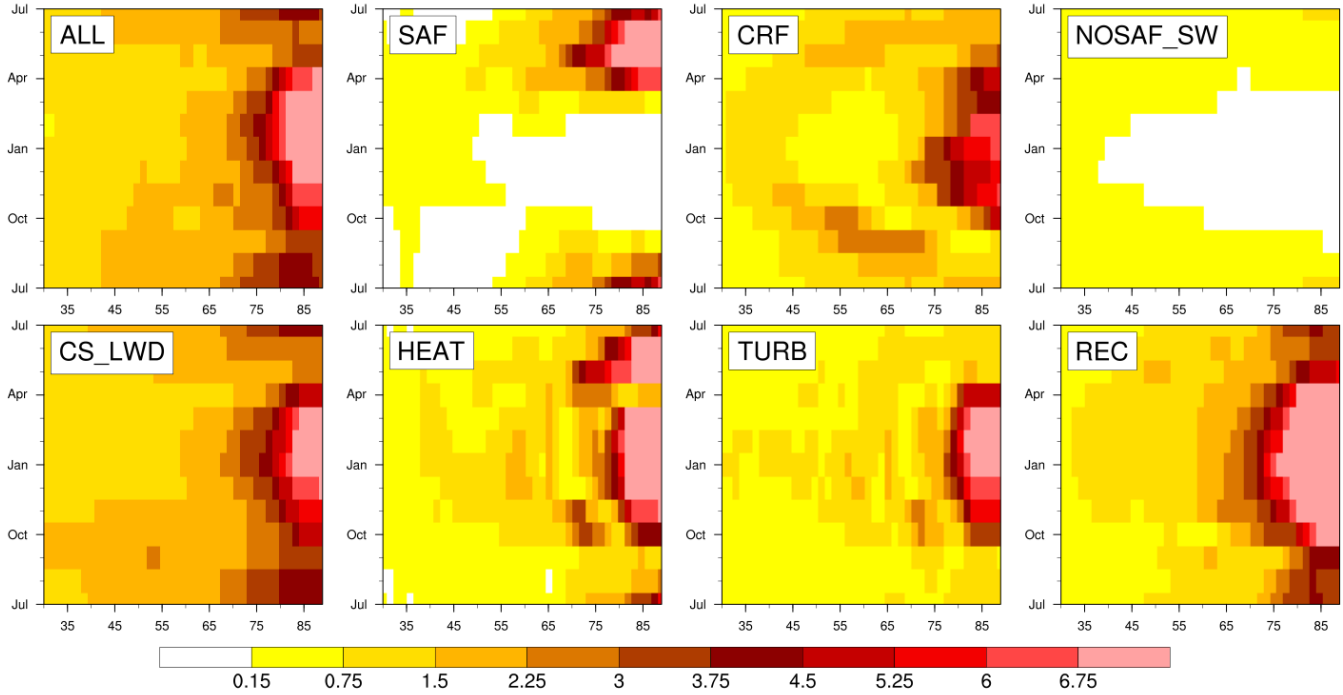

Figure 38: Seasonal cycle (Y-Axis) of the multi-model spread of zonal-averaged surface temperature change (in K) at quadrupling CO_2 concentration over mid- to high latitudes (X-Axis) of the Northern Hemisphere: (ALL) the total Arctic warming; the partial temperature changes due to (SAF) surface albedo feedback, (CRF) the change in surface cloud radiative forcing, (NOSAF_SW) the non-SAF-induced change in clear-sky shortwave radiation, (CS_LWD) the change in net clear-sky longwave radiation fluxes, (HEAT) the change in heat storage times -1, and (TURB) the changes in surface sensible/latent fluxes, respectively; (REC) the sum of the 6 previous contributions.

Next, we evaluate the impact of horizontal resolution and land-ocean contrast. For that purpose, we compare the low- and high-resolution versions (LR and HR) for three models (CNRM-CM6-1, HadGEM3-GC3.1, MPI-ESM1-2). Figures 39 and 40 show that there is no discernible and significant difference between the LR and HR results regarding both the total surface temperature

change and the partial temperature changes relative to the processes mentioned above. Differences, if any, between LR and HR results are of small amplitude and much smaller than the inter-model spread depicted in Fig. 38.

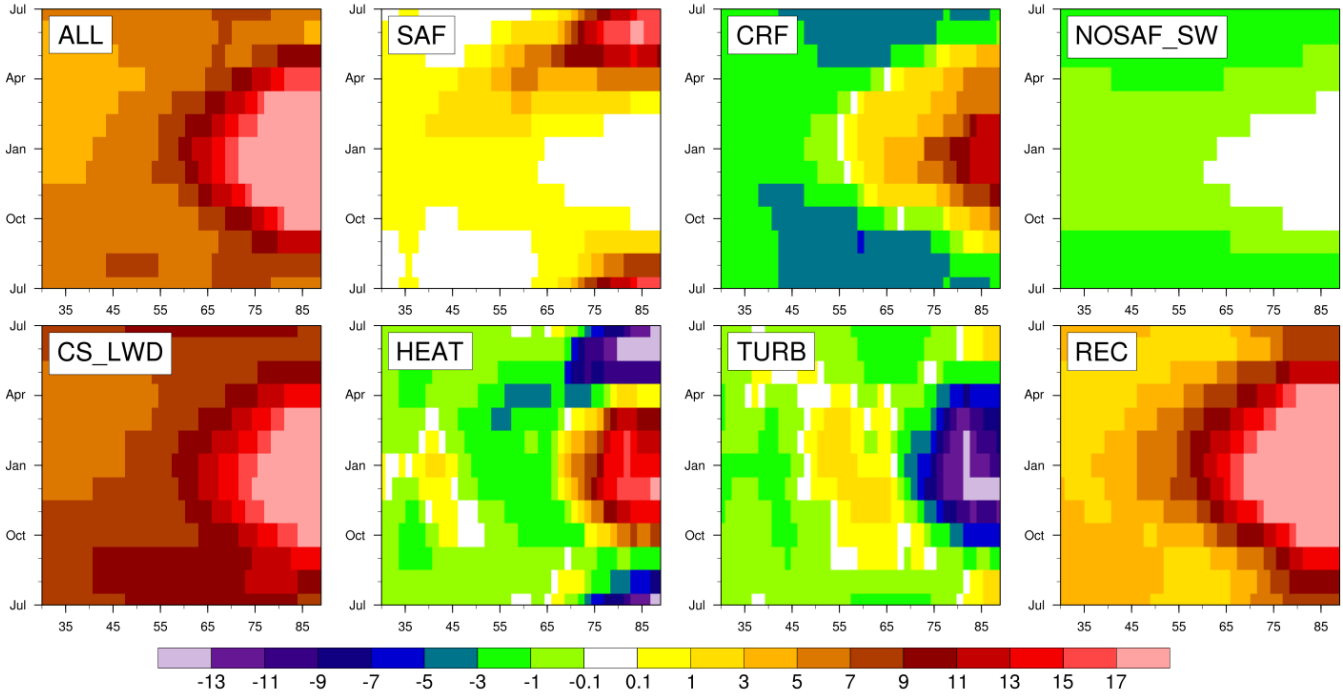

Figure 39: Same as Fig. 37 but only for the multi-model mean of the low-resolution version of CNRM-CM6-1, HadGEM3-GC3.1 and MPI-ESM1-2.

Finally, we depict land-ocean contrast in Arctic surface warming amplification. We use again all the models and compare the forced response to CO_2 increase between ocean and land grid-points. Figure 41 (Fig. 42) shows the seasonal cycle of Arctic surface warming amplification for land (ocean) grid-points. In winter at high latitudes, the ocean surface warming is larger than the land warming (it is the reverse in summer) due to large sea ice loss. At low latitudes, south of the Arctic region, the warming is greater over land during the whole year (with the snow melting and snow-albedo feedback being active over land throughout most of the seasonal cycle at different latitudes). As with the whole domain, the main process driving the seasonal cycle of the surface warming is related to changes in clear-sky downward longwave radiation (CS_LWD) for both land and ocean domains. In summer over land, SAF and CRF almost cancel each other and smaller amplitude negative contributions from TURB, HEAT and NOSAF_SW. In winter, the positive CRF contribution enhances the warming due to CS_LWD with the contributions from other mechanisms being much weaker. In summer over the ocean, there is an almost cancellation between the two dominant drivers, SAF and HEAT. In winter, there is also an almost cancellation, but between HEAT and TURB. The substantial positive cloud radiative forcing (CRF) adds up to the CS_LWD contribution, more significantly than over land.

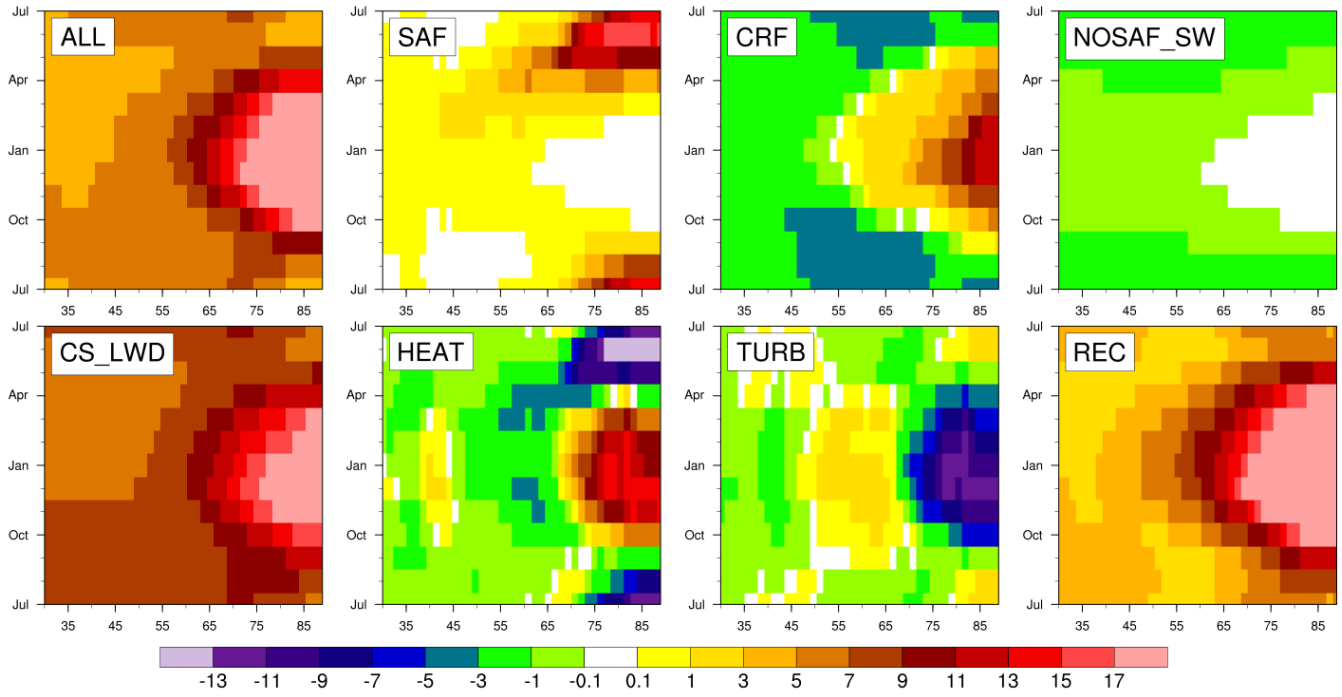

Figure 40: Same as Fig. 39 but for the high-resolution version.

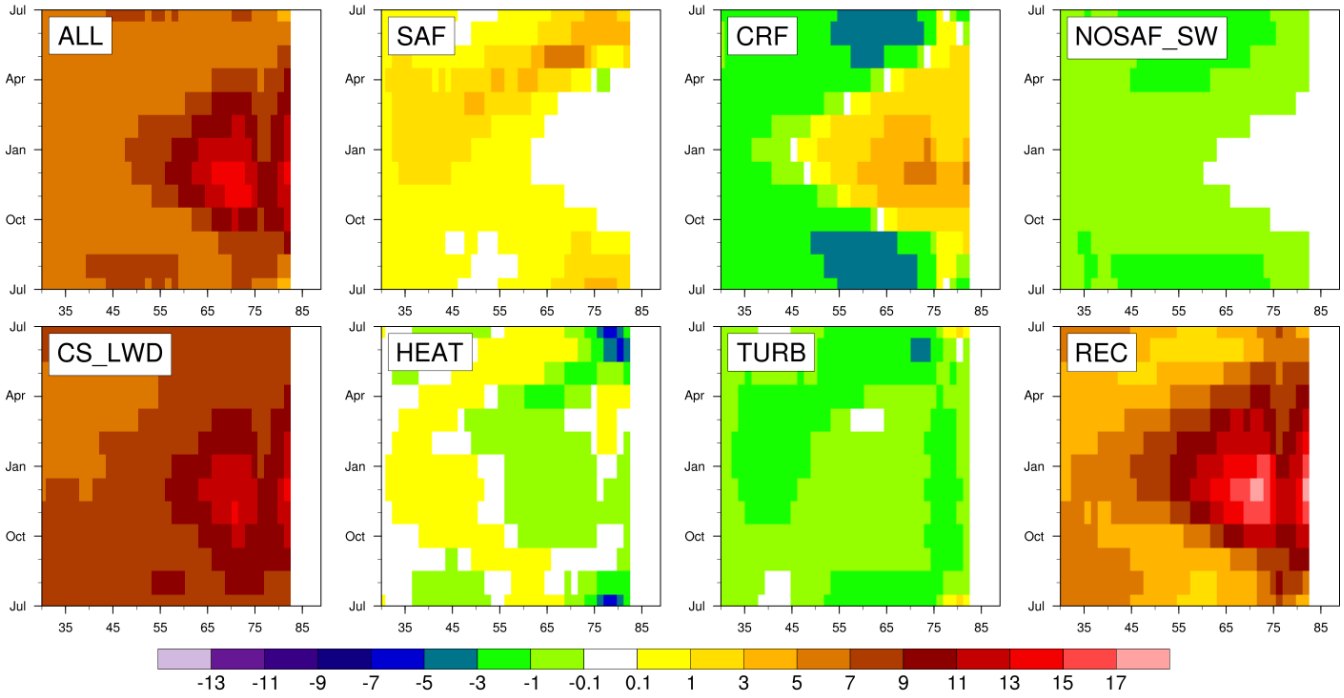

Figure 41: Same as Fig. 37 but only using land grid-points.

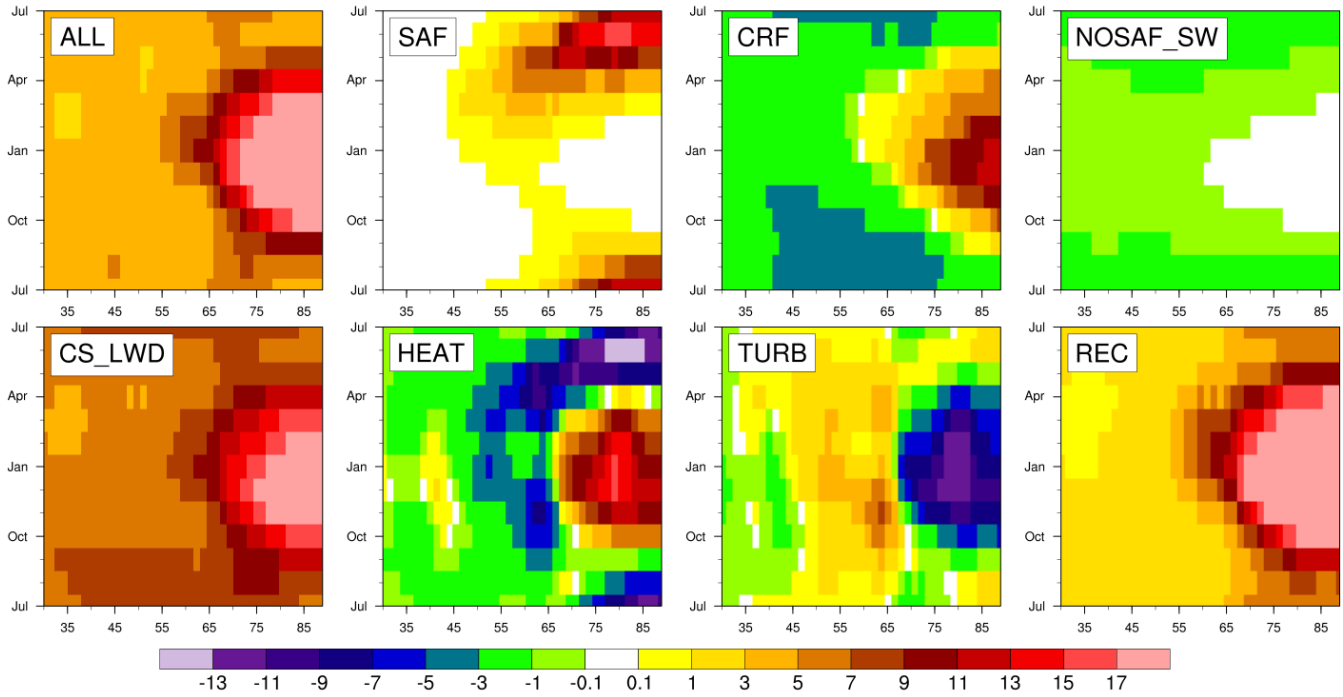

Figure 42: Same as Fig. 37 but only using ocean grid-points.

4 Forced mode: results and discussion

4.1 Form drag

4.1.1 Impact of form drag on the sea ice within NEMO3.6-LIM3

In complement to the results in the coupled mode shown in Sec. 3.1.3, this section assesses the sea ice representation in forced mode simulations performed with NEMO3.6-LIM3 using a prescribed atmospheric state. The first simulation, named REF, uses constant drag coefficients at the ocean-ice and atmosphere-ice interfaces. The second simulation makes use of the variable drag coefficients formulated by Tsamados et al. (2014), referred to as DRG. Both simulations use the topographic melt pond scheme given by Flocco and Feltham (2007).

To assess the results of the simulations, we compare the model outputs to the SIC from Nimbus-7 SMMR and DMSP SSM/I-SSMIS passive microwave data given by Cavalieri et al. (2012) (referred to as NSIDC 0051). Also, we examine the Integrated Ice Edge Error (IIEE) introduced by Goessling et al. (2016) to quantify the misplacement of the ice edge, using NSIDC 0051 as the reference product. By definition, IIEE is the total area where the simulated local sea ice extent differs from NSIDC 0051.

In the Arctic, the mean seasonal cycle of the total sea ice extent is smaller in DRG compared to REF (Fig. 43). The underestimation accentuates to 2.5×10^5 km^2 in August and September. Also, the IIEE in DRG reduces by 1×10^5 km^2 compared to REF. The improvements in DRG, in terms of mean sea ice extent and IIEE, seem to associate with reduced biases in SIC in the Greenland Sea, Fram Strait, and the Barents Sea.

The mean seasonal cycle of the total sea ice volume from DRG is smaller than that from REF all year round, as shown in Fig. 44. The total sea ice volume in the Arctic from PIOMAS reanalysis (Schweiger et al., 2011) is shown in black on the same figure. As for information, Schweiger et al. (2011) estimated the uncertainty of PIOMAS Arctic sea ice volume as 1.35×10^3 km^3 in October and 2.25×10^3 km^3 in March. The mean seasonal cycle of the total sea ice volume from DRG is close to PIOMAS, and the seasonal minimum of Arctic sea ice volume has the same magnitude as PIOMAS. The model overestimates the mean total sea ice volume in REF all-year-round compared to PIOMAS. DRG features a larger mean sea ice volume in winter than PIOMAS. However, the overestimation in March reduces by 3×10^3 km^3 between DRG and REF. Last, the variability of the total sea ice volume in NEMO is similar between DRG and REF. The phase and amplitude of the mean seasonal cycles remain preserved between the two simulations.

Figure 45 shows the difference maps of mean sea ice velocities between DRG and REF averaged from 1980 to 2015. The ice velocities simulated in DRG are 1 to 4 cm s^{-1} smaller in the Central Arctic than the ice velocities in REF. However, DRG has greater ice velocities in the Canadian Arctic Archipelago and the coastal regions in the North American sector. The greater estimation of ice velocities in DRG extends through Fram Strait and in the Greenland Sea whenever sea ice is present. In winter, the ice velocities in the Barents, Kara, and Laptev Seas are smaller in

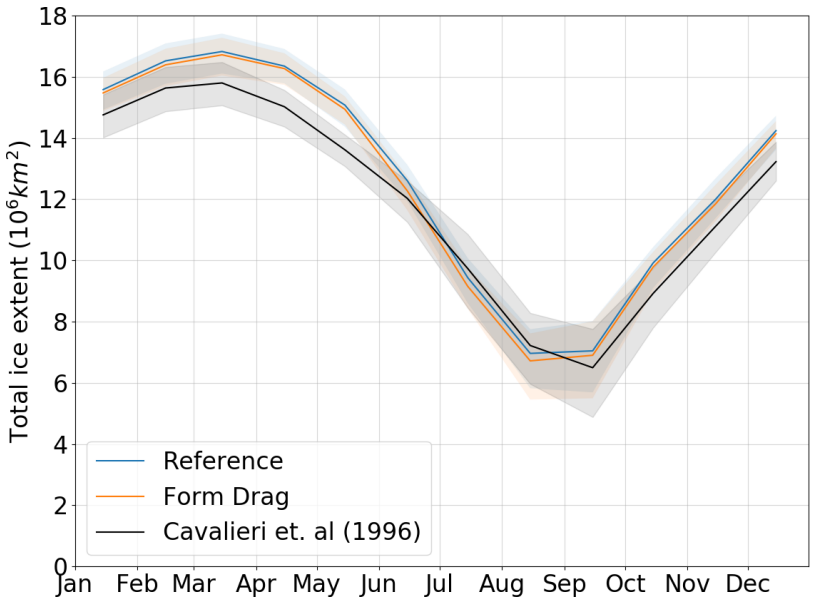

Figure 43: Mean seasonal cycles of total sea ice extent in the Arctic between 1980 and 2015 for the reference simulation with constant drag coefficients (blue), the simulation with variable drag coefficients (orange), and the observational product NSIDC 0051 (black). Shaded areas indicate the 10th and 90th percentiles of the ice extent per month between 1980 and 2015.

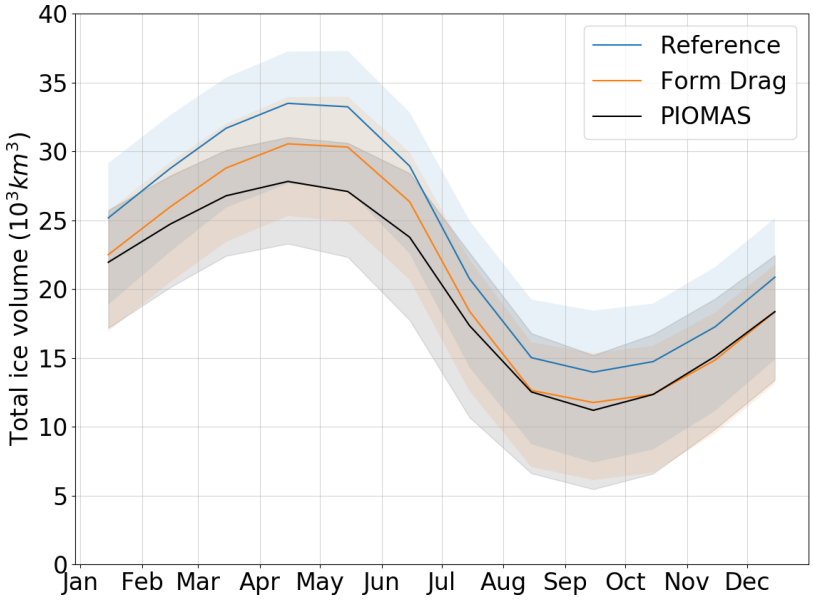

Figure 44: Mean seasonal cycles of total sea ice volume in the Arctic between 1980 and 2015 for the reference simulation with constant drag coefficients (blue), the simulation with variable drag coefficients (orange), and the reanalysis product PIOMAS (black). Shaded areas indicate the 10th and 90th percentiles of the ice volume per month between 1980 and 2015.

DRG than in REF, except on the shores of Severnaya Zemlya and Novaya Zemlya islands. The differences in sea ice velocities between the two simulations accentuate during the summer months. Further investigations may establish potential links between the variable drag coefficients and the reductions in sea ice volume or ice velocities. As a next step, we continue to implement the form drag parameterization in the EC-Earth3 setup with a coupled earth system.

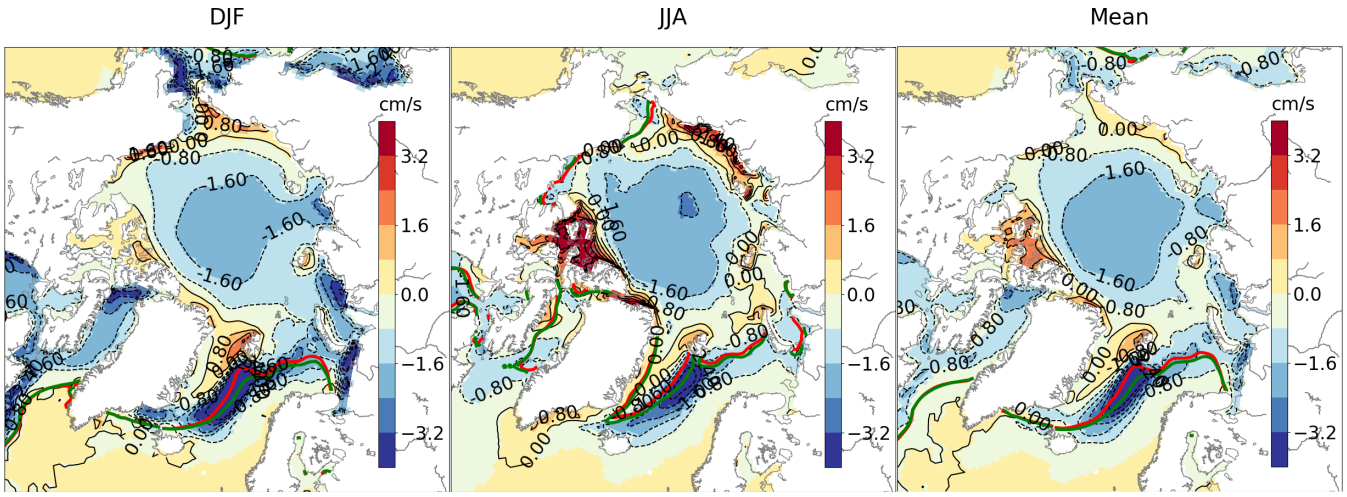

Figure 45: Difference of mean sea ice velocities in cm s^{-1} between DRG and REF from 1980 to 2015 in the Arctic, during winter (left), summer (center) and annual mean (right). The red (green) contour line indicates the position of the 15% ice concentration line in REF (DRG).

4.2 Melt ponds

4.2.1 Impact of melt ponds on the sea ice within GELATO

The prognostic melt pond scheme described in Sec. 2.2.2 is activated within GELATO. In this study, GELATO includes the updated snowpack scheme described in Sec. 2.3.3, in its 3-layer configuration. Atmosphere-forced simulations are performed following the CMIP6/OMIP2 protocol (JRA-55-based forcing, see Tsujino et al. (2018)). The results shown here are based on years 1981-2010 of a 1958-2018 simulation. By contrast with the OMIP2 specifications, only one forcing cycle was run, but it could be checked that differences between simulated sea ice in the last (sixth) and the first cycle of another OMIP2 simulation are very small.

Figure 46 shows the impact of the prognostic melt pond scheme on sea ice albedo. The summer albedo simulated by GELATO using the Køltzow (2007) melt pond simple parameterization and the snowpack model in its 3-layer configuration (SN3L, bottom row) is probably slightly overestimated compared to in situ observations such as those from the SHEBA campaign, during which surface albedo as low as 0.4 was observed (Perovich et al., 2002), due to the presence of melt ponds. In the configuration with prognostic melt ponds (SN3L MP, top row), the albedo decreases more during the summer, down to less than 0.5 north of Greenland.

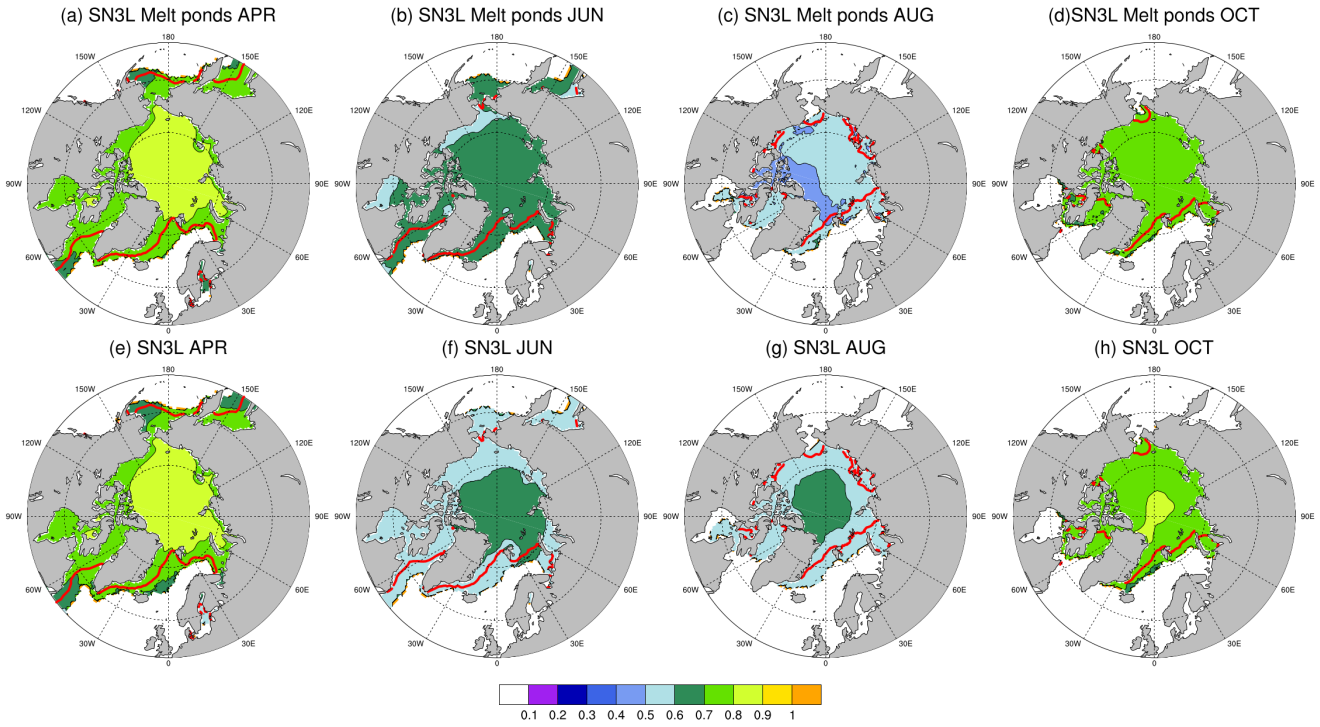

Figure 46: Monthly mean sea ice albedo [0 1], simulated by NEMO-GELATO including the updated snowpack scheme in its 3-layer configuration and the prognostic melt pond scheme (top row) for (from left to right) April, June, August and October (average for 1981-2010). Bottom row: same as top row, but with the simple parameterization of the albedo and fraction of melt ponds (Køltzow, 2007). The climatological sea ice edge for 1981-2010, defined here as the 15% SIC contour line, is inferred from the HadISST data set (Rayner et al., 2007).

As shown in Fig. 47, sea ice simulated by GELATO with 3 snow layers (SN3L, b, d) is thinner by about 0.5 m than in the GIOMAS reconstructions (a, d) year round, but the simulated ice edge is close to observations. Since the surface albedo during the summer in SN3L-MP (including prognostic melt ponds) is lower than in SN3L, the summer melt is more pronounced and sea ice is thinner year-round in SN3L-MP (c, e). In winter, the simulated ice edge in SN3L-MP is realistic (c), but in summer (f), the panarctic sea ice extent is less than in observations.

4.3 Multilayer snow scheme

4.3.1 Impact of the snow scheme on the sea ice within NEMO3.6-LIM3

Figure 48 shows the difference maps of the Arctic Ocean sea ice volume (per unit grid cell area) and surface snow depth during March and September analyzed from the two runs. Because of the lack of radiative transfer in CTRL and higher snow thermal conductivity in a single layer (0.31 W m^{-1} K^{-1}) than multilayer snow thermal conductivity (up to about 0.25 W m^{-1} K^{-1}), the

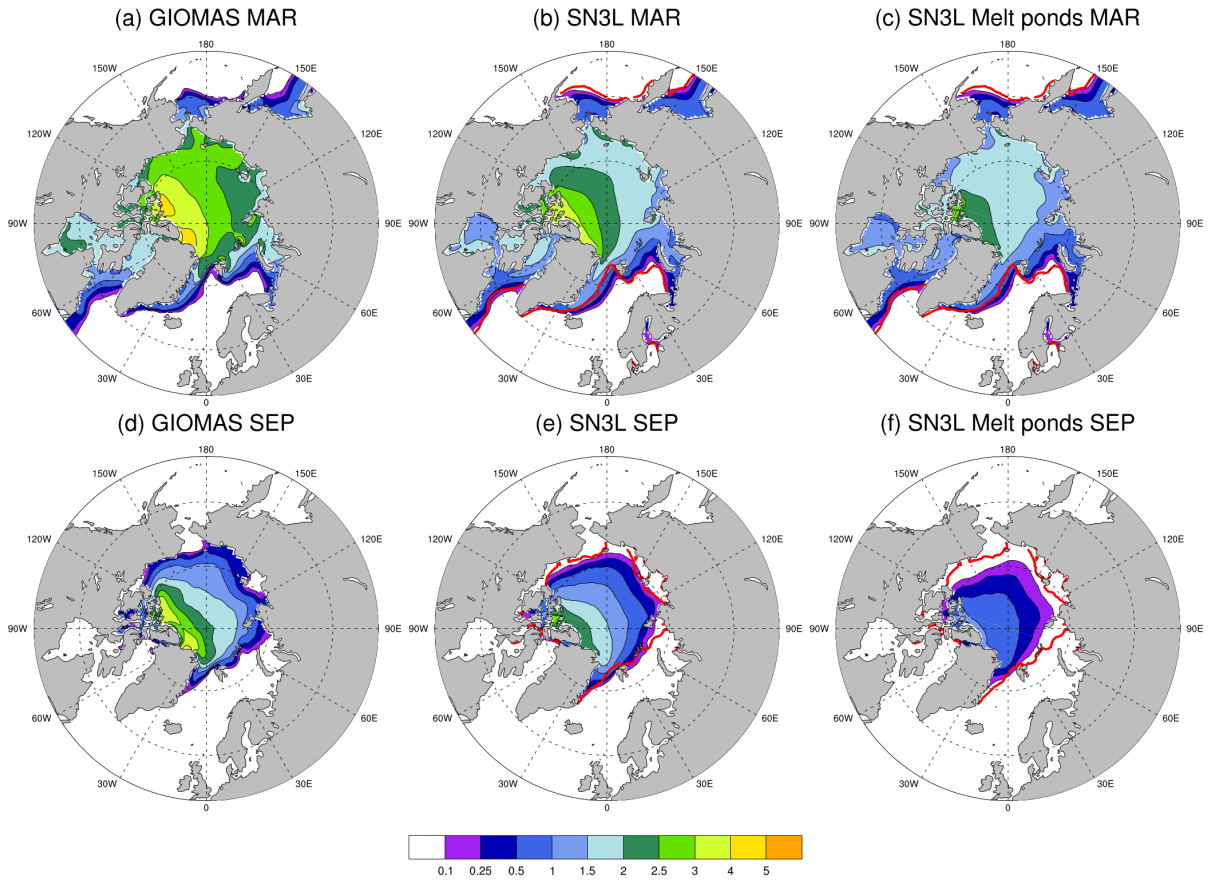

Figure 47: Monthly mean sea ice volume per area (m) for March (top row) and September (bottom row) for 1981-2010 in the PIOMAS reconstructions (Zhang and Rothrock, 2003) (left column), simulated by GELATO with its 3-layer snow scheme (middle), and simulated by GELATO with 3-layer snow scheme and prognostic melt ponds (right). The climatological sea ice edge for 1981-2010, defined here as the 15% SIC contour line, is inferred from the HadISST data set (Rayner et al., 2007).

overestimation of surface snow depth occurs during winter in the Norwegian Sea (Fig. 48a).

The CTRL uses a single snow layer with a constant thermal conductivity of 0.31 W m^{-1} K^{-1}, which is not used in the multilayer snow scheme run (SNOW). To compare with SNOW, the last 20-year mean snow depth climatology simulated from the CTRL as shown in Fig. 49. This constant value overestimates surface snow depth in winter compared to SNOW and underestimates it in the summer (Fig. 48a,c). It leads to an overestimation of the SIT in the Fram Strait during both summer and winter (Fig. 48b), whereas the underestimation of sea ice volume (per unit grid cell area) in summer occurs in most of the western Arctic Ocean (including Beaufort and Chukchi

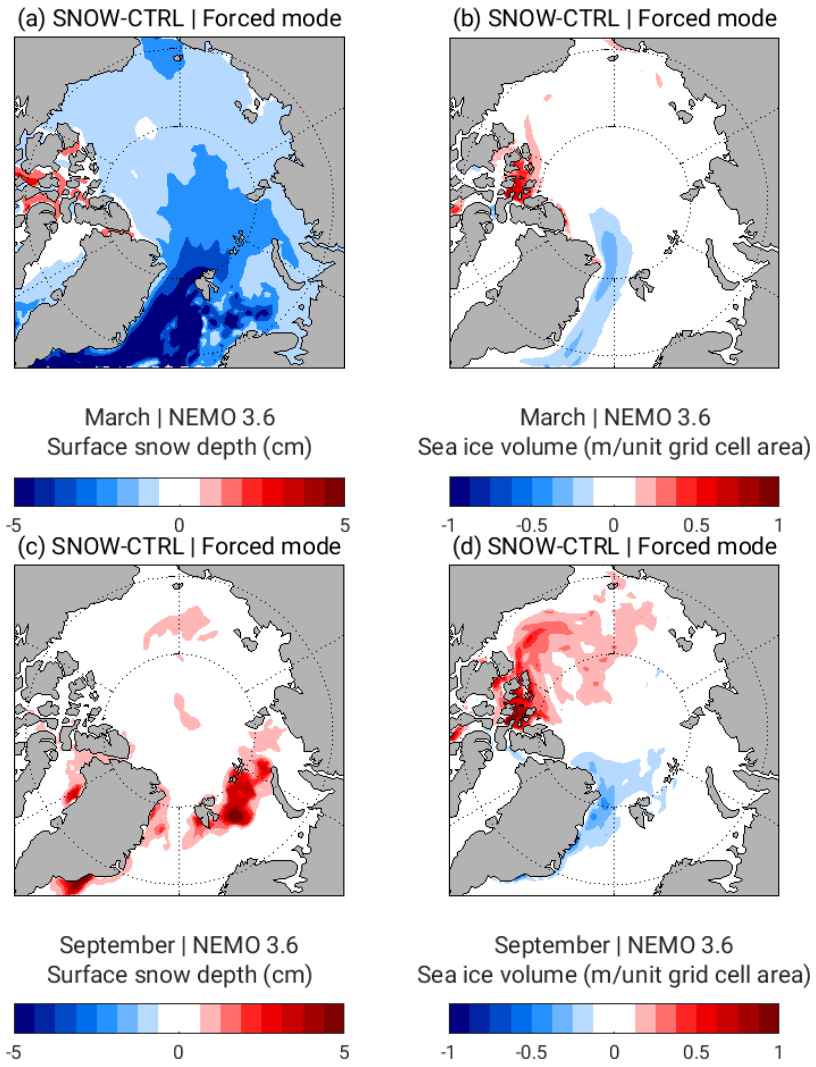

Figure 48: Difference maps of Arctic Ocean sea ice volume (per unit grid cell area) (b, d) and surface snow depth (a, c) obtained from the multilayer snow scheme run and CTRL for 58-year run in forced mode using NEMO3.6 during March (a, b) and September (c, d).

Seas, East Siberian Sea, Canada Basin, and Central Arctic, Fig. 48d). The multilayer snow scheme uses wind-dependent snow thermal conductivity and snow density for different layers, which is more sensitive to the thermodynamic surface forcing than a single layer scheme with constant thermodynamic properties.

Because of varying snow physics in the Arctic during the summer season, there is a large over- and under-estimation of ice volume and surface snow depth as also seen in the HCI diagnostics (Figs. 49 and 50). HCI is useful here because of its sensitivity to the thickness of snow layers and conductivity. The snow depth is highest during the October-November months and the positive HCI difference (SNOW minus CTRL) is observable in all winter months. Forced simulations, therefore,

are season- and hemisphere-dependent, where the underlying snow physics and the surface energy budget can be substantially different. The CTRL has no radiative transfer, whereas the multilayer snow scheme implements radiative transfer parameterization in sea ice with specific extinction coefficients.

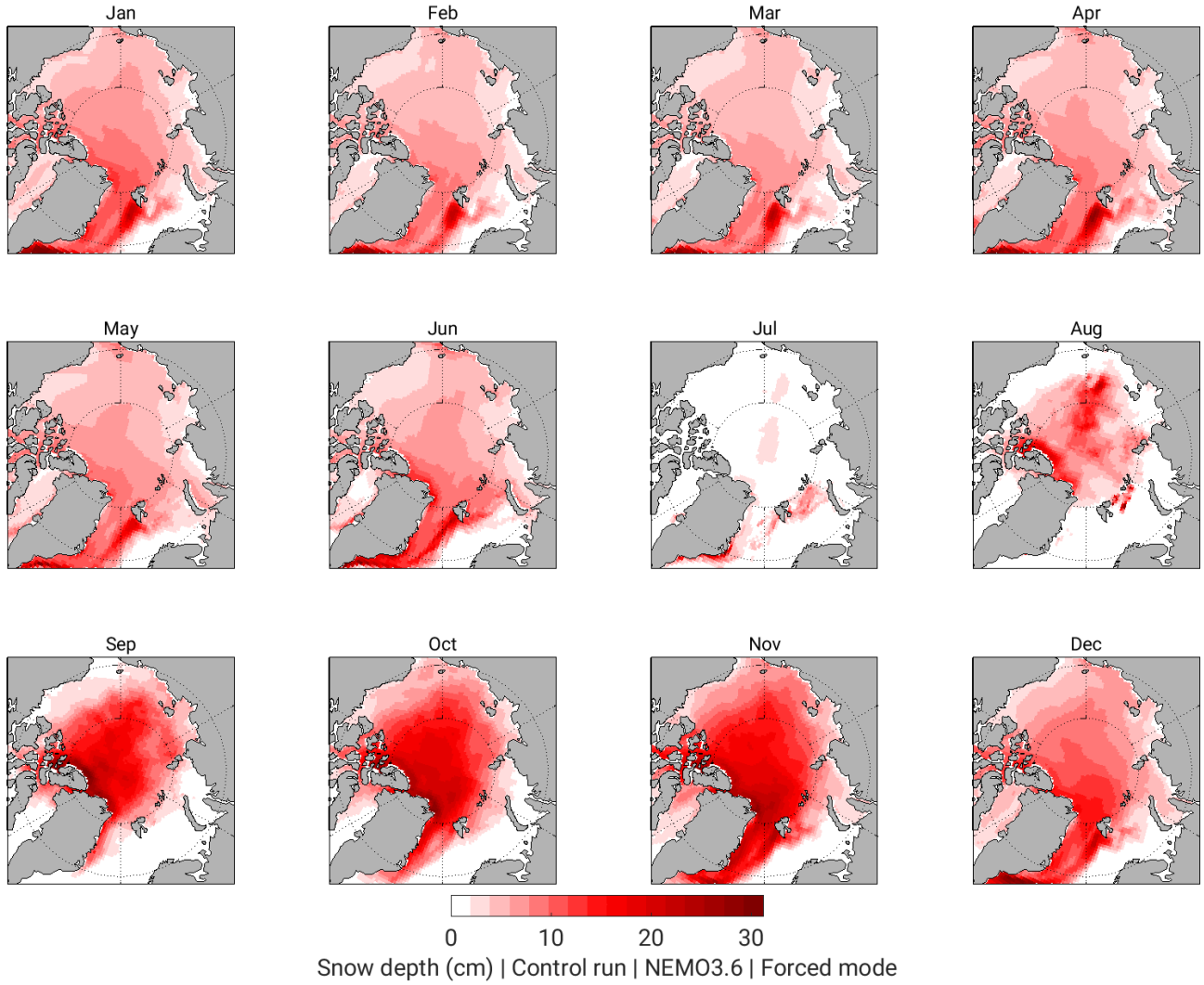

Figure 49: Snow depth climatology maps of Arctic Ocean surface obtained from the last 20-year mean of 58-year CTRL in forced mode using NEMO3.6.

Introducing radiative transfer in the multilayer snow parameterization makes the model more sensitive to the surface thermodynamic forcing compared to the CTRL that uses a single layer of snow. The low snow thermal conductivity (versus 0.31 W m^{-1} K^{-1} in the CTRL) limits the basal thermodynamic growth of sea ice because of little loss of heat through the ice column. The lateral ice production compensates it to maintain the hydrostatic equilibrium of the snow-ice column. A high snow thermal conductivity in the CTRL leads to less sea ice volume (per unit grid cell area)

in the Fram Strait and the Greenland Sea, whereas a higher sea ice volume results in the Canadian Arctic Archipelago and Canada Basin after introducing the multilayer snow scheme (Fig. 48b, d). The increased surface snow depth in September implies more insulating snow on top of sea ice that limits the heat loss from the ice to the atmosphere and thus limits the basal ice growth in the Kara and Barents Seas (Fig. 48c, d).

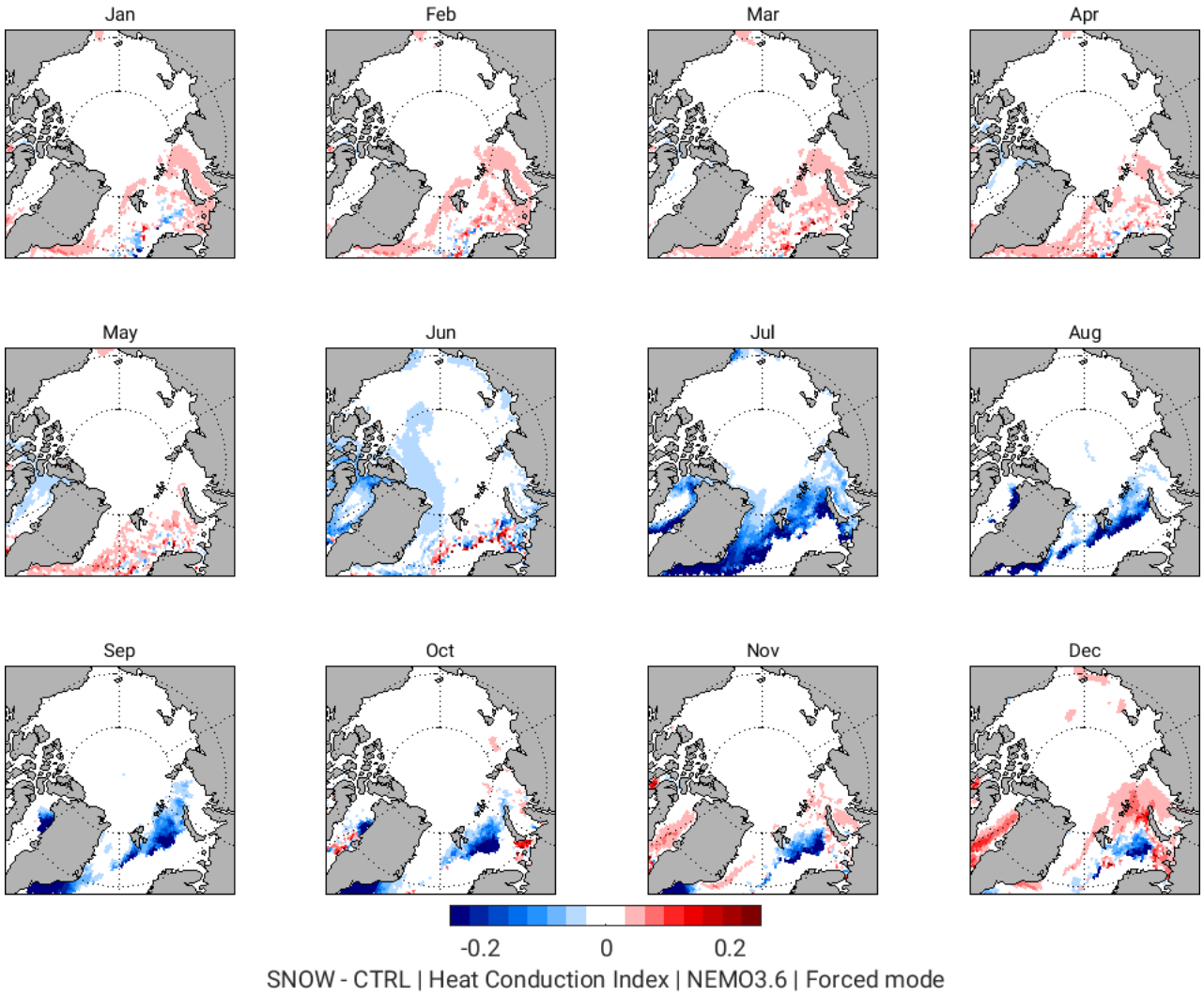

Figure 50: Difference (SNOW minus CTRL) maps of Heat Conduction Index in the Arctic Ocean obtained from the last 20-year mean of multilayer snow scheme run and CTRL of 58 years in forced mode using NEMO3.6.

4.3.2 Impact of the snow scheme on the sea ice within GELATO

As for the melt ponds experiments from Sec. 4.2.1, the results presented here are based on years 1981-2010 of a forced ocean-sea ice simulation run following the CMIP6/OMIP2 protocol.

The winter ice edge is close to observations in the 3- and 1-layer snow model configurations (SN3L and SN1L, respectively). As already noticed in Sec. 4.2.1, the sea ice edge is also close to observations in summer for SN3L. Sea ice is thinner year round in SN1L than in SN3L, and during the summer, the thinner ice in SN3L tends to melt away in vast portions of the Arctic where it is actually observed (North of Siberia and Alaska). These differences are currently not fully understood, and understanding them will require further investigation.

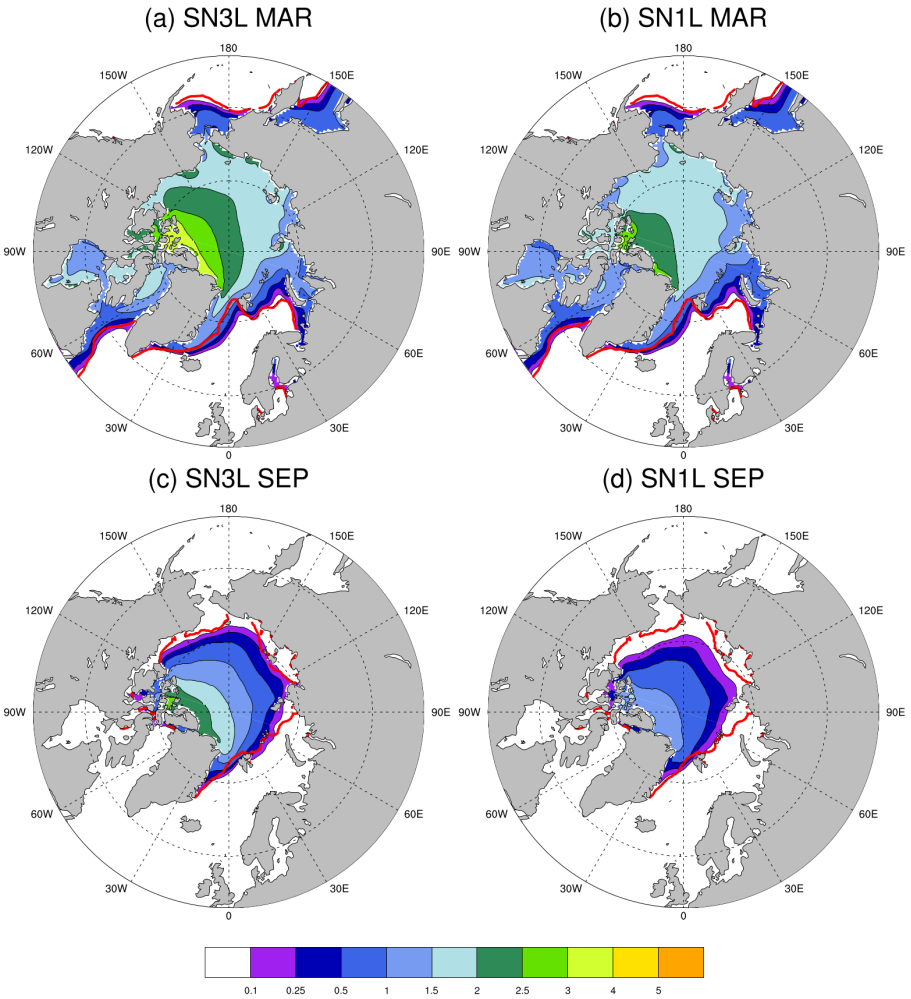

Figure 51: Monthly mean sea ice volume per area (m) for March (top row) and September (bottom row) for 1981-2010 simulated by GELATO with its 3-layer snow scheme (left column), and simulated by GELATO with 1-layer snow scheme (right). The climatological sea ice edge for 1981-2010, defined here as the 15% SIC contour line, is inferred from the HadISST data set (Rayner et al., 2007).

5 Conclusions and outlook

This report introduces a set of ten physical-process parameterizations implemented in various numerical models, both in forced (GELATO and NEMO3.6-LIM3) and coupled mode (AWI-CM1, EC-Earth3 PRIMAVERA, HadGEM3-GC3.1, and IFS CY45R1).

The new and improved parameterizations developed in APPLICATE intend to provide a better representation of physical-processes as observed in the Arctic and, therefore, improve long-term climate predictions (or short-term weather forecasts, in the ECMWF Integrated Forecasting System case). For different reasons (e.g., internal variability, compensating biases, or coupled feedbacks), the impact of the parameterizations is not always straightforward. Sometimes, it is small and/or statistically non-significant or even shows a negative effect. In this case, we should still consider to use the parameterizations since they intend to represent observed physical-processes, provided that they are not computationally too expensive. Some arguments in favour of this approach are discussed by Hyder et al. (2018).

Apart from reporting the model developments, D2.5 also provides a first assessment of these by making use of different metrics and diagnostics, including one diagnostic developed in WP1 (the Heat Conduction Index reported in D1.3). In addition, D2.5 assesses the Arctic atmospheric response to CO_2 anthropogenic forcing for the increased model resolution.

We summarize the key conclusions from the new model parameterizatons introduced in this report based on the five aspects (i–v) defined earlier for assessing the model developments, as follows:

(i) changes in various components of the Arctic surface energy budget (radiative, turbulent)

- Analyses based on the Heat Conduction Index show that the form drag parameterization implemented in HadGEM3 affects the heat exchange through the sea ice in different months of the year and regions (Fig. 5, see Sec. 3.1.1 – Form drag in HadGEM3).
- The melt pond parameterization shows a clear impact on the albedo and sea ice variability (Figs. 19–23, see Sec. 3.2.1 – Melt pond in EC-Earth3). An improved representation of the floe size distribution within EC-Earth3 PRIMAVERA reveals that large ice floes cause growth in SIC and SIT in the marginal ice zone during summer (Fig. 36, see Sec. 3.5.1 – Floe size distribution in EC-Earth3).
- The use of a multilayer snow scheme, which considers radiative transfer through multiple layers, makes the model more sensitive to the surface thermodynamic forcing than the control run that uses a single layer of snow (Figs. 48–50, see Sec. 4.3.1 – Multilayer snow scheme in NEMO3.6-LIM3).
- Numerical weather prediction also benefits from an improved multilayer snow scheme. The

new parameterization implemented in IFS CY45R1 improves the heat conduction within the snowpack and, therefore, the coupling with the underlying atmosphere. This leads to an improved prediction of the 2-m temperature diurnal cycle over land in short- to medium-range forecasts. Over sea ice, the snow thermal insulation effect accounted by the new scheme reduces large positive biases of outgoing longwave radiation. As consequence, the simulation of the sea-ice surface temperature is enhanced (see Sec. 3.3.1 – Multilayer snow scheme in IFS CY45R1).

(ii) changes in the transfer of momentum from the atmosphere to the ocean

- Common results emerged from the form drag experiments: increased sea ice drift speed in the marginal ice zone (Figs. 13 and 45), general decrease in SIT and therefore volume (Figs. 16, 4b,d and 44), and a marginal decrease of SIC at the ice edge in summer (Figs. 14 and 4a,c) [see Sec. 3.1.1 – Form Drag in HadGEM3; Sec. 3.1.2 – Form Drag in AWI-CM1; and Secs. 3.1.3 and 4.1.1 – Form Drag in EC-Earth3].
- For the HadGEM3, a decline in SIT is observed because of the form drag parameterization in winter in most of the Arctic Ocean whereas the impact on winter SIC is little in the entire Arctic Ocean (Fig. 4). The mean seasonal cycle of the total sea ice extent/volume in the Arctic is smaller in form-drag-activated simulation in NEMO3.6-LIM3 compared to the reference simulation (Figs. 43 and 44).
- The sensitivity experiments of AWI-CM1 reveal long-term impact more pronounced in the region near the marginal ice zone, both in the atmosphere (air temperature; Fig. 15) and sea ice (drift, concentration, and thickness; Figs. 13, 14, and 16).

(iii) the overall realism of the simulated climate system

- The form drag parameterization within HadGEM3 improves the large scale atmospheric circulation. Long-standing biases like the too zonal Atlantic storm track have improved based on its signature on the wind stress curl (Figs. 10 and 11, see Sec. 3.1.1 – Form Drag in HadGEM3).
- The implementation of the form drag parameterization within NEMO3.6-LIM3 improves the representation of the SIC compared to observational satellite data (Fig. 43). The sea ice volume reconstructed with form drag is closer to a reference reanalysis (PIOMAS; Fig. 44). Form drag implementation in EC-Earth3 PRIMAVERA reduces SIC in the MIZ of the Greenland Sea in all seasons (see Sec. 4.1.1 – Form Drag in NEMO3.6-LIM3).
- Preliminary results from the melt pond and multilayer snow parameterizations implemented within GELATO indicate a more realistic representation of the albedo (Fig. 46). As a consequence, sea ice is thinner year-round in the model configuration with prognostic melt ponds

than in the model with diagnostic melt ponds (Figs. 47 and 51). Although, in both cases, there is a bias in SIT compared to observations and, therefore, further improvement is needed to improve the sea ice representation (see Sec. 4.2.1 – Melt pond in GELATO; and Sec. 4.3.2 – Multilayer snow scheme in GELATO).

- The EC-Earth3 PRIMAVERA sensitivity experiments with landfast ice developments lead to more realistic sea ice conditions (Figs. 32 and 33). The sea ice velocity is very low in magnitude in the regions of expected fast ice zones, as supported by evidence from observational data (Fig. 34, see Sec. 3.4.1 – Landfast ice in EC-Earth3).
- A comparison against satellite observations indicates that there is an improvement in the representation of surface temperatures when the ECMWF multilayer snow scheme is active over the sea ice. The new scheme enhances the forecast of the Arctic 2-m temperature diurnal cycle at lead times of 1–6 days (Figs. 26–28, see Sec. 3.3.1 – Multilayer snow scheme in IFS CY45R1).

(iv) effects on the Arctic Ocean circulation

- The form drag parameterization within HadGEM3 shows an impact on the large scale atmospheric circulation. As consequence, different aspects of the wind-driven ocean circulation are also impacted such as the subpolar gyre ((Figs. 10 and 11), the heat transport into the Nordic Seas (Fig. 7) and towards the Arctic through the Fram Strait and Barents Sea Opening (Figs. 6–8). Also, a reduction in the annual mean turbulent heat flux close to the ice edge is identified (Fig. 12) due to an attenuation in the wind speed (see Sec. 3.1.1 – Form drag in HadGEM3).
- The EC-Earth3 PRIMAVERA melt pond experiments reinforces that a reduced sea ice regime in the Arctic impacts the large-scale, density-driven ocean circulation. From these experiments, SIT and ice extent time evolution correlates with the maximum AMOC (at 26°N latitude). This correlation implies that AMOC and SIT/extent have an inverse relationship (Fig. 25, see Sec. 3.2.1 – Melt ponds in EC-Earth3).

(v) changes in the Arctic climate sensitivity

- The HadGEM3-modified form drag reduced ocean temperature and salinity biases in the Arctic Ocean in the low CO_2 case, but with an adverse effect of increasing the warm bias in the subpolar gyre (Figs. 7, 8, and 9). However, the adverse effects could be minimized by additional tuning (see Sec. 3.1.1 – Form drag in HadGEM3).
- A simple linearization of the surface heat budget equation applied to a set of 1pctCO2-increase multi-model simulations has shown that the primary driver of the Arctic amplification seasonal cycle is related to changes in clear-sky downwelling longwave radiation, although

other mechanisms (surface albedo feedback, cloud radiative forcing, surface sensible and latent heat fluxes, and changes in heat storage) also contribute to surface warming in specific months with smaller magnitude. Changes in horizontal resolution do not seem to have impact on the results. However, note that the highest resolution (50 km) is far from being eddy-resolving over the mid-to-high latitude oceans (see Sec. 3.6 – Impact of model resolution).

Besides the impact that all physical parameterizations have on the simulated essential climate variables and climate feadbacks, further work requires a more comprehensive model validation through a comparison against observational data. This comprehensive evaluation will certainly benefit from recent efforts of the scientific community to enhance the Arctic observational system through recent observational expeditions such as the Multidisciplinary drifting Observatory for the Study of Arctic Climate (MOSAiC; https://www.mosaic-expedition.org/).

References

Amante, C. and B. Eakins (2009), ETOPO1 1 Arc-Minute Global Relief Model: procedures, data sources and analysis, *NOAA Technical Memorandum NESDIS NGDC-24. National Geophysical Data Center, NOAA*. DOI: 10.7289/V5C8276M.

Andreas, E. L. et al. (2010), Parametrizing turbulent exchange over summer sea ice and the marginal ice zone, *Q. J. R. Meteorol. Soc.*, *136* (649), 927–943. DOI: 10.1002/qj.618.

Arduini, G. et al. (2019), Impact of a multi-layer snow scheme on near-surface weather forecasts, *J. Adv. Model. Earth Syst*, *11*, 4687–4710. DOI: 10.1029/2019MS001725.

Batrak, Y. and M. Müller (2019), On the warm bias in atmospheric reanalyses induced by the missing snow over Arctic sea-ice, *Nat. Commun.*, *10*, 4170. DOI: 10.1038/s41467-019-11975-3.

Boone, A. (2002). *Description du schema de neige ISBA-ES (Explicit Snow). (Description of the ISBA-ES Explicit snow scheme)*. 70. Note de Centre, Meteo-France/CNRM, p. 53.

Cavalieri, D. J. et al. (2012), Sea Ice Concentrations from Nimbus-7 SMMR and DMSP SSM/I-SSMIS Passive Microwave Data, Version 1, *NASA National Snow and Ice Data Center Distributed Active Archive Center*. DOI: 10.5067/8gq8lzqvl0vl.

Day, J. J. et al. (2020), Measuring the impact of a new snow model using surface energy budget process relationships, *J. Adv. Model. Earth Syst*. DOI: 10.1029/2020MS002144.

Dussin, R. et al. (2016). *The making of the DRAKKAR Forcing Set DFS5. Drakkar/myocean report.* Laboratoire de Glaciologie et de Géophysique de l'Environnement, Université de Grenoble, Grenoble, France.

Elvidge, A. D. et al. (2016), Observations of surface momentum exchange over the marginal ice zone and recommendations for its parametrisation, *Atmos. Chem. Phys.*, *16*, 1545–1563. DOI: 10.5194/acp-16-1545-2016.

Flocco, D. and D. Feltham (2007), A continuum model of melt pond evolution on Arctic sea ice, *J. Geophys. Res. Oceans*, *112* (C08016). DOI: 10.1029/2006JC003836.

Flocco, D. et al. (2010), Incorporation of a physically based melt pond scheme into the sea ice component of a climate model, *J. Geophys. Res. Oceans*, *115* (C08012). DOI: 10.1029/2009JC005568.

Flocco, D. et al. (2012), Impact of melt ponds on Arctic sea ice simulations from 1990 to 2007, *J. Geophys. Res. Oceans*, *117* (C09032). DOI: 10.1029/2012jc008195.

Goessling, H. F. et al. (2016), Predictability of the Arctic sea ice edge, *Geophys. Res. Lett.*, *43* (4), 1642–1650. DOI: 10.1002/2015GL067232.

Grenfell, T.C. and D. K. Perovich (2004), Seasonal and spatial evolution of albedo in a snow-ice-land-ocean environment, *J. Geophys. Res. Oceans*, *109* (C1). DOI: 10.1029/2003JC001866.

Griffies, S. et al. (2009), Coordinated Ocean-ice Reference Experiments (COREs), *Ocean Model.*, *26* (1-2), 1–46. DOI: 10.1016/j.ocemod.2008.08.007.

Haarsma, R. et al. (2020), HighResMIP versions of EC-Earth: EC-Earth3P and EC-Earth3P-HR – description, model computational performance and basic validation, *Geosci. Model Dev.*, *13*, 3507–3527. DOI: 10.5194/gmd-13-3507-2020.

Hibler, W. and E. Schulson (2000), On modeling the anisotropic failure and flow of flawed sea ice, *J. Geophys. Res. Oceans*, *105* (C7), 17105–17120. DOI: 10.1029/2000JC900045.

Holland, M. M. et al. (2012), Improved sea ice shortwave radiation physics in CCSM4: The impact of melt ponds and aerosols on Arctic sea ice, *J. Clim.*, *25* (5), 1413–1430. DOI: 10.1175/JCLI-D-11-00078.1.

Horvat, C. et al. (2016), Interaction of sea ice floe size, ocean eddies, and sea ice melting, *Geophys. Res. Lett.*, *43* (15), 8083–8090. DOI: 10.1002/2016GL069742.

Hunke, E. C. and W. H. Lipscomb (2010). *CICE: the Los Alamos sea ice model, documentation and software user's manual, Version 4.1 (Tech. Rep. LA-CC-06-012)*. Los Alamos, NM: Los Alamos National Laboratory.

Hunke, E. C. et al. (2013), Level-ice melt ponds in the Los Alamos sea ice model, CICE, *Ocean Model.*, *71*, 26–42. DOI: 10.1016/j.ocemod.2012.11.008.

Hutchings, J. K. and I. G. Rigor (2012), Role of ice dynamics in anomalous ice conditions in the Beaufort Sea during 2006 and 2007, *J. Geophys. Res.*, *117*, C00E04. DOI: 10.1029/2011JC007182.

Hyder, P. et al. (2018), Critical Southern Ocean climate model biases traced to atmospheric model cloud errors, *Nat. Commun.*, *9* (3625). DOI: 10.1038/s41467-018-05634-2.

Itkin, P. et al. (2015), Landfast ice affects the stability of the Arctic halocline: Evidence from a numerical model, *J. Geophys. Res. Oceans*, *120* (4), 2622–2635. DOI: 10.1002/2014JC010353.

Køltzow, M. (2007), The effect of a new snow and sea ice albedo scheme on regional climate model simulations, *J. Geophys. Res. Atmos.*, *112* (D7). DOI: 10.1029/2006JD007693.

Laine, V. (2004), Arctic sea ice regional albedo variability and trends, 1982–1998, *J. Geophys. Res. Oceans*, *109* (C06027). DOI: 10.1029/2003JC001818.

Large, W. and S. Yeager (2004), Diurnal to decadal global forcing for ocean and sea-ice models: The data sets and flux climatologies, *University Corporation for Atmospheric Research, (No. NCAR/TN-460+STR)*. DOI: 10.5065/D6KK98Q6.

Large, W. and S. Yeager (2008), The global climatology of an interannually varying air–sea flux data set, *Clim. Dyn.*, *33* (2-3), 341–364. DOI: 10.1007/s00382-008-0441-3.

Lawrence, H. et al. (2019), Use and impact of Arctic observations in the ECMWF Numerical Weather Prediction system, *Q. J. R. Meteorol. Soc.*, *145* (725), 3432–3454. DOI: 10.1002/qj.3628.

Lebrun, M. (2019). *De l'interaction entre banquise, lumière et phytoplancton arctique*. Océanographie. Sorbonne Université.

Lecomte, O. et al. (2013), On the formulation of snow thermal conductivity in large-scale sea ice models, *J. Adv. Model. Earth Syst*, *5* (3), 542–557. DOI: 10.1002/jame.20039.

Lecomte, O. et al. (2015), Benefits from representing snow properties and related processes in coupled ocean–sea ice models, *Ocean Model.*, *87*, 81–85. DOI: 10.1016/j.ocemod.2014.11.005.

Lemieux, J. et al. (2015), A basal stress parameterization for modeling landfast ice, *J. Geophys. Res. Oceans*, *120* (4), 3157–3173. DOI: 10.1002/2014JC010678.

Lemieux, J. F. et al. (2016), Improving the simulation of landfast ice by combining tensile strength and a parameterization for grounded ridges, *J. Geophys. Res. Oceans*, *121* (10), 7354–7368. DOI: 10.1002/2016JC012006.

Lu, J. and M. Cai (2009), Seasonality of polar surface warming amplification in climate simulations, *Geophys. Res. Lett.*, *36*, L16704. DOI: 10.1029/2009GL040133.

Lüpkes, C. and G. Birnbaum (2005), Surface drag in the Arctic marginal sea-ice zone: A comparison of different parameterisation concepts, *Boundary-Layer Meteorology*, *117*, 179–211. DOI: 10.1007/s10546-005-1445-8.

Lüpkes, C. and V. M. Gryanik (2015a), A stability-dependent parameterization of transfer coefficients for momentum and heat over polar sea ice to be used in climate models, *J. Geophys. Res. Atmos.*, *120* (2), 552–581. DOI: 10.1002/2014JD022418.

Lüpkes, C. and V. M. Gryanik (2015b). *New parametrization of transfer coefficients over polar sea ice: instructions for the application in ECHAM6, Technical report*. Tech. rep. Alfred Wegener Institute for Polar and Marine Research.

Lüpkes, C. et al. (2012), A parameterization, based on sea ice morphology, of the neutral atmospheric drag coefficients for weather prediction and climate models, *J. Geophys. Res. Atmos.*, *117* (D13), 1–18. DOI: 10.1029/2012JD017630.

Lüpkes, C. et al. (2013), Effect of sea ice morphology during Arctic summer on atmospheric drag coefficients used in climate models, *Geophys. Res. Lett.*, *40* (2), 446–451. DOI: 10.1002/grl.50081.

Mahajan, S. et al. (2011), Impact of the Atlantic Meridional Overturning Circulation (AMOC) on Arctic surface air temperature and sea ice variability, *J. Clim.*, *24*, 6573–6581. DOI: 10.1175/2011JCLI4002.1.

Maykut, G. A. and N. Untersteiner (1971), Some results from a time-dependent thermodynamic model of sea ice, *J. Geophys. Res.*, *76* (6), 1550–1575. DOI: 10.1029/JC076i006p01550.

Morison, J. et al. (2012), Changing Arctic Ocean freshwater pathways, *Nature*, *481*, 66–70. DOI: 10.1038/nature10705.

Perovich, D. K. et al. (2002), Seasonal evolution of the albedo of multiyear Arctic sea ice, *J. Geophys. Res. Oceans*, *107* (C10). DOI: 10.1029/2000JC000438.

Pogson, L. et al. (2011), Development and validation of a one-dimensional snow-ice algae model against observations in Resolute Passage, Canadian Arctic Archipelago, *J. Geophys. Res. Oceans*, *116* (C4). DOI: 10.1029/2010jc006119.

Rayner, N. A. et al. (2007), Global analyses of sea surface temperature, sea ice, and night marine air temperature since the late nineteenth century, *J. Geophys. Res. Atmos.*, *108* (D14). DOI: 10.1029/2002JD002670.

Renfrew, I. A. et al. (2019), Atmospheric sensitivity to marginal-ice-zone drag: Local and global responses, *Q. J. R. Meteorol. Soc.*, *145* (720), 1165–1179. DOI: 10.1002/qj.3486.

Ricker, R. et al. (2014), Sensitivity of CryoSat-2 Arctic sea-ice freeboard and thickness on radar-waveform interpretation, *The Cryosphere*, *8* (4), 1607–1622. DOI: 10.5194/tc-8-1607-2014.

Ridley, J. K. et al. (2018), The sea ice model component of HadGEM3-GC3.1, *Geosci. Model Dev.*, *11*, 713–723. DOI: 10.5194/gmd-11-713-2018.

Roberts, M. J. et al. (2019), Description of the resolution hierarchy of the global coupled HadGEM3-GC3.1 model as used in CMIP6 HighResMIP experiments, *Geosci. Model Dev.*, *12*, 4999–5028. DOI: 10.5194/gmd-12-4999-2019.

Roberts, M. J. et al. (2020), Impact of Model Resolution on Tropical Cyclone Simulation Using the HighResMIP–PRIMAVERA Multimodel Ensemble, *J. Clim.*, *33* (7), 2557–2583. DOI: 10.1175/JCLI-D-19-0639.1.

Rothrock, D. A. and A. S. Thorndike (1984), Measuring the sea ice floe size distribution, *J. Geophys. Res. Oceans*, *89* (C4), 6477–6486. DOI: 10.1029/JC089iC04p06477.

Schweiger, A. et al. (2011), Uncertainty in modeled Arctic sea ice volume, *J. Geophys. Res. Oceans*, *116* (C8). DOI: 10.1029/2011JC007084.

Semmler, T. et al. (2020), Simulations for CMIP6 with the AWI climate model AWI-CM-1-1, *J. Adv. Model. Earth Syst.*, *12* (e2019MS002009). DOI: 10.1029/2019MS002009.

Shine, K.P. and A. Henderson-Sellers (1985), The sensitivity of a thermodynamic sea ice model to changes in surface albedo parameterization, *J. Geophys. Res. Atmos.*, *90* (D1), 2243–2250. DOI: 10.1029/JD090iD01p02243.

Steiner, N. et al. (1999), Sea-ice roughness and drag coefficients in a dynamic–thermodynamic sea-ice model for the Arctic, *Tellus A*, *51* (5), 964–978. DOI: 10.3402/tellusa.v51i5.14505.

Thonner, A. (2016). "Implémentation d'une paramétrisation de la glace de mer côtière dans le modèle NEMO-LIM3". MA thesis. Université Catholique de Louvain.

Tsamados, M. et al. (2014), Impact of variable atmospheric and oceanic form drag on simulations of Arctic sea ice, *J. Phys. Oceanogr.*, *44* (5), 1329–1353. DOI: 10.1175/JPO-D-13-0215.1.

Tsamados, M. et al. (2015), Processes controlling surface, bottom and lateral melt of Arctic sea ice in a state of the art sea ice model, *Phil. Trans. R. Soc. A*, *373* (2052), 1–30. DOI: 10.1098/rsta.2014.0167.

Tsujino, H. et al. (2018), JRA-55 based surface dataset for driving ocean-sea-ice models (JRA55-do), *Ocean Model.*, *130*, 79–139. DOI: 10.1016/j.ocemod.2018.07.002.

Voldoire, A. et al. (2019), Evaluation of CMIP6 DECK experiments with CNRM-CM6-1, *J. Adv. Model. Earth Syst.*, *11* (7), 2177–2213. DOI: 10.1029/2019MS001683.

West, A. E. et al. (2016), The location of the thermodynamic atmosphere–ice interface in fully coupled models – a case study using JULES and CICE, *Geosci. Model Dev.*, *9* (3), 1125–1141. DOI: 10.5194/gmd-9-1125-2016.

Williams, K. D. et al. (2017), The Met Office Global Coupled model 3.0 and 3.1 (GC3.0 & GC3.1) configurations, *J. Adv. Model. Earth Syst*, *10* (2), 357–380. DOI: 10.1002/2017MS001115.

Zhang, J. and D. A. Rothrock (2003), Modeling global sea ice with a thickness and enthalpy distribution model in generalized curvilinear coordinates, *Monthly Weather Review*, *131* (5), 845–861. DOI: 10.1175/1520-0493(2003)131<0845:MGSIWA>2.0.CO;2.

List of acronyms

AMOC	Atlantic Meridional Ocean Circulation
APPLICATE	Advanced Prediction in Polar regions and beyond: modelling, observing system design and LInkages associated with a Changing Arctic climaTE
AWI-CM1	Alfred Wegener Institute-Climate Model 1
CERFACS	Centre Européen de Recherche et de Formation Avancée en Calcul Scientifique
CESM	Community Earth System Model
CICE	Community Ice CodE
CMEMS	Copernicus Marine Environmental Monitoring Service
CMIP6	Coupled Model Intercomparison Project 6
CNRM	Centre National de Recherches Météorologiques
CORE	Coordinated Ocean-ice Reference Experiments
COVID-19	COronaVIrus Disease 2019
CPU	Central Processing Unit
CRF	Cloud Radiative Forcing
CTRL/CTL	Control run
DECK	Diagnostic, Evaluation and Characterization of Klima
DFS	Drakkar Forcing Set
DMSP	Defense Meteorological Satellite Program
ECCC	Environment and Climate Change Canada
EC-Earth	European Community-Earth System Model
ECHAM	ECMWF HAMburg model
ECMWF	European Centre for Medium-Range Weather Forecasts
ERA5	ECMWF reanalysis 5
EVP	Elastic-Viscous-Plastic
FD	Form Drag
FSD	Floe Size Distribution
GELATO	Global Experimental Leads and ice for ATmosphere and Ocean
GHG	Green House Gas
GISS	Goddard Institute for Space Studies
GS	Greenland-Scotland Ridge
HadGEM3-GC3.1	Hadley Centre Global Environment Model version 3; using the Global Coupled configuration 3.1

HCI	Heat Conduction Index
HTESSEL	Hydrology Tiled ECMWF Scheme for Surface Exchanges over Land
IIEE	Integrated Ice Edge Error
IFS CY45R1	Integrated Forecasting System Cycle 45R1
ISBA-ES	Interactions between Soil, Biosphere and Atmosphere-Explicit Snow
JULES	Joint UK Land Environment Simulator
LIM3	Louvain-la-Neuve Ice Model 3
MetUM	Met Office Unified Model
MIZ	Marginal Ice Zone
MOSAiC	Multidisciplinary drifting Observatory for the Study of Arctic Climate
MPI-ESM	Max-Planck-Institut-Earth-System Model
NEMO	Nucleus for European Modelling of the Ocean
NH	Northern Hemisphere
NIC	National Ice Center
NORCE	Norwegian Research Centre
NSIDC	National Snow and Ice Data Center
piControl	pre-industrial Control simulation
PIOMAS	Pan-Arctic Ice Ocean Modeling and Assimilation System
PRIMAVERA	PRocess-based climate sIMulation: AdVances in high-resolution modelling and European climate Risk Assessments
SAF	Surface Albedo Feedback
SIC	Sea Ice Concentration
SIT	Sea Ice Thickness
SMMR	Scanning Multichannel Microwave Radiometer
SSMIS	Special Sensor Microwave Imager / Sounder
SU	Stockholm University
UCLouvain/UCL	Université catholique de Louvain
UTC	Coordinated Universal Time
WOA	World Ocean Atlas
WP	Work Package